METAMATERIAL RADIATION FROM ATTENUATED TOTAL REFLECTION AT TERAHERTZ FREQUENCIES

By

SUCHITRA RAMANI

Bachelor of Engineering
University of Mumbai
Mumbai, India
2001

Master of Science in Photonics
Oklahoma State University
Stillwater, Oklahoma
2006

Submitted to the Faculty of the
Graduate College of the
Oklahoma State University
in partial fulfillment of
the requirements for
the Degree of
DOCTOR OF PHILOSOPHY
December, 2013

METAMATERIAL RADIATION FROM ATTENUATED TOTAL REFLECTION AT TERAHERTZ FREQUENCIES

Dissertation Approved:

Dr. Weili Zhang

Dissertation Adviser

Dr. Daniel Grischkowsky

Dr. John O'Hara

Dr. Albert Rosenberger

This thesis is dedicated to my late father, Dr.K.Ramani.

ACKNOWLEDGEMENTS

Three people who sacrificed their time and energy in this long and arduous journey, to whom I will be eternally grateful — my father, my mother and my husband— without them I would not have been able to scale such heights.

I would not have come this far without the dedication, support and guidance of my friend, my colleague and my husband, Matt Reiten. Matt, the unsung hero in all this who stepped up to fulfil the role of an advisor and a mentor, in addition to fulfilling the role of a new father and a caring husband. He believed in me when I had stopped believing in myself. Matt, I cannot thank you enough and will never forget what you have done for me. I hope I can be a pillar of support for you.

To my father who laid the foundation for me to pursue science. Daddy, you are dearly missed and you will always be my inspiration.

Thank you mom for being patient and understanding all these years and taking care of me and Kavya during the rough times.

I express my sincere gratitude to my collaborators Dr. John O'Hara and Dr.Pat Colestock who undertook the task of coming up with a suitable theoretical model to match my experimental results. Thank you for all the time invested in this unfunded project despite your other academic and professional commitments. It was a pleasure working with both of you and I have learnt a lot in the process. I look forward to future collaborations. Pat, I admire your enthusiasm and how you worked on this problem for the sheer fun of it.

Thank you John for being supportive and encouraging and seeing through to the end. You proofread the thesis draft multiple times, a task that is expected of an advisor. Your valuable suggestions have resulted in a document that I'm proud of.

I am extremely grateful to Dr. Weili Zhang who stepped in as my committee chair

and advisor when my former advisor had abandoned me.

I would like to thank Dr Grischowsky for his unwavering support and encouragement over the years.

Thank you Dr. Rosenberger for being a part of my doctoral research committee and helping me refine my dissertation document.

Thanks to my sister Sandhya who did not give up hope and thought so highly of me.

I would like to thank Abul Azad and Toni Taylor for supporting this research and allowing me to access the THz ranging experiment.

Folks at the TA-35 machine shop, thank you for being such a lively audience and coming up with innovative designs for the prism holder and cage system. You also helped broaden my baking skills.

Lastly, thank you mom and dad, for giving me this opportunity to pursue higher education.

Name: SUCHITRA RAMANI

Date of Degree: DECEMBER, 2013

Title of Study: METAMATERIAL RADAIATION FROM ATTENUATED TOTAL REFLECTION AT TERAHERTZ FREQUENCIES

Major Field: PHOTONICS (ELECTRICAL ENGINEERING)

Abstract: The focus of this research was to explore the behavior of two-dimensional planar metamaterials or metafilms and understand the various excitation schemes for application of metafilms to Terahertz-Attenuated Total Reflection spectroscopy (THz-ATR). A standard THz time domain spectroscopy system based on photoconductive switches was modified to implement the ATR technique. Finite metamaterial arrays with varying singly- split ring resonator sizes were excited in the Kretschmann ATR configuration using finite sized terahertz beams. Numerical approaches using commercial software were looked into to explain the experimental observations. Various theoretical models were used to explain the observed phenomena. The ATR measurements showed an unexpected strengthening of the resonance when the metafilm sample was illuminated near the edge. This phenomenon referred to in this study as "the anomalous edge enhancement" was observed strongly in metafilms with closely spaced rings. A re-radiation signal was observed across the total internal reflection barrier where no signal is expected. It consisted of two peaks one at the fundamental metamaterial resonance and the second peak was due to the periodicity of the metafilm array. The anomalous behavior seen in the ATR measurements is attributed to the edge currents at the boundary of the metafilm array giving rise to this re-radiation signal. Results from analytic treatments based on Floquet method and method of moments were able to qualitatively model the measurements. The observed re-radiation signal is a potential loss mechanism that could impact observations from commonly used transmission measurements on metamaterials.

.TABLE OF CONTENTS

Chapter Page

LIST OF TABLES

LIST OF FIGURES

LIST OF SYMBOLS AND ACRONYMS

Symbol/Acronym	Meaning
α	Power absorption coefficient
a	periodicity
A	Absorption /Absorbance
A_{rr}	Losses due to re-radiation
ATR	Attenuated total reflection
c	Speed of light in vacuum
C	Capacitance
CW	Continuous wave
d	distance or thickness as indicated
d_e	Effective thickness
d_{edge}	Relative displacement of the array with respect to the incident THz beam
d_p	Penetration depth
D	Goos-Hanchen shift
DC	Direct Current
eSRR	Electric split ring resonator
EM	Electromagnetic
ε	Electric permittivity
f	Frequency
f	focal length
FDTD	Finite Difference Time Domain
FRU	Field Replaceable Unit
FWHM	Full Width Half Maximum
GH	Goos-Hanchen
H	Transfer function
i	Imaginary number $(-1)^{½}$
IRE	Internal Reflection Element

IRS	Internal Reflection Spectroscopy
k_0	Free-space wavenumber
$k_{i,}$ k_r, k_t	Incident, Reflected, Transmitted wave vectors
L	Inductance
λ	Wavelength
λ_0	resonant wavelength of the SRR in free space
MF	Metafilm
MI	Magneto-inductive wave
MM	Metamaterial
μ	Magnetic permeability
n	Index of refraction
p	Polarization in the plane of incidence TM
φ	Phase change
Q	Quality factor
r	Fresnel field reflection coefficient
$\mathrm{r}_{\mathrm{ATR}}$	ATR coefficient
R	Resistance
R	Reflectance or Reflectivity
s	Polarization out of the plane of incidence (TE)
SRR	Split ring resonator
SOS	Silicon on sapphire
t	Fresnel field transmission coefficient
T	Transmissivity or Transmittance
TIR	Total Internal Reflection
TL	Transmission line
θ_{c}	Critical angle
θ_{i}	Angle of incidence
$\mathrm{\omega}$	Angular frequency, (rad/s)
ω_0	Fundamental (LC) frequency, (rad/s)
w_{o}	Beam waist (radius)
Z	Impedance
z	Propagation distance

1 Introduction

"…Why consider finite arrays?

The short answer to this question is,

Because they are the only ones that really exist."— Ben Munk[*]

1.1 Motivation

The focus of this research has been to explore the behavior of metamaterials (MM)—specifically metafilms (MF) — and understand the various excitation schemes for application to Terahertz-Attenuated Total Reflection (THz-ATR) spectroscopy. This investigation deals with both theoretical and experimental aspects of terahertz excitation of metamaterials. The selective excitation of metamaterials via THz electric field, magnetic field, and their combination; and the corresponding effect on THz radiation emitted from MM elements has been investigated. A re-radiation signal is observed across the forbidden TIR boundary where no signal is expected and is due to the fundamental resonance of a split ring resonator array. The influences of edge effects and coupling on radiation by finite arrays are studied in this work. This is a unique phenomenon that has not been observed at THz frequencies previously to the author's knowledge.

---

[*] Ben A. Munk, *Finite Antenna Arrays and FSS*, Wiley Interscience, 2003.

The results of this study extend the current understanding of total internal reflection at surfaces of dielectrics with resonant patterned structures and the resultant re-radiation from the MM arrays observed using ATR. This research will further the understanding of how single and multi-layer thin resonant films on the surface of a dielectric affect the evanescent field to enable improvements in spectroscopy and sensing and the impact of sample edge effects.

1.2 Background of Terahertz technology

The Terahertz region of the electromagnetic spectrum, the so-called "terahertz gap" has received considerable attention and has become a rapidly evolving field since its discovery two decades ago. This gap encompasses the sub-millimeter region between 0.1 THz (3mm) to 10 THz (30 μm) and traditionally has been explored by using both microwave and optical techniques. Sub-picosecond near single cycle pulses of terahertz radiation with broad bandwidths from tens of GHz up to a few THz are commonly generated by optically exciting a biased photoconductive switch. The other most commonly used methods of terahertz wave generation is optical rectification. A large number of materials are transparent to terahertz radiation, but are opaque at optical frequencies. Terahertz spectroscopy techniques have become increasingly important in material characterization. The rotational and vibrational modes of many molecules lie in the terahertz region that can be probed directly by THz radiation thus making it attractive for sensing applications. Terahertz radiation offers many applications in chemical sensing, imaging, biological sciences [1] and medicine. THz or T-ray imaging is particularly of interest to medical imaging and security screening due to its non-ionizing and non-invasive properties. Much of the recent interest in terahertz radiation lies in its ability to penetrate through a number of materials such as paper, polymers, and textiles to name a few. THz waves are strongly absorbed by water. This property makes it appealing for security diagnostics—detection of explosives and non-destructive evaluation and testing [2]. The development of terahertz technology is lagging due to the lack of high power THz sources and functional devices. This makes it a fertile area for commercialization due to the merging of optical technologies and high frequency electronics. More recently, there has been a great deal of interest in creating high power THz sources through non-linear techniques [3]. Advances in device fabrication techniques have furthered terahertz research and tremendous progress has been in this field such as the development of the quantum cascade laser [4]. A review of scientific developments in the THz region can be found in review articles and texts such as [5-9] and references therein.

Terahertz Time-Domain Spectroscopy (THz-TDS) has become a reliable and non-invasive coherent spectroscopic technique, where information about the amplitude and the phase information of the test sample can be directly obtained. THz-TDS has proven to be a sensitive tool in the detection and analysis of a variety of materials including gases and liquids. It is used to study carrier transport and relaxation dynamics in semiconductors.

Terahertz-time domain spectroscopy based on photoconductive antenna will be covered in great detail in the next chapter.

1.3 Attenuated total reflection

Attenuated total reflection (ATR) is an established sampling technique to study material properties by taking advantage of the evanescent field at a surface due to the phenomenon of total internal reflection. When an absorbing sample is brought in contact with an optically denser medium, the intensity of the evanescent field is modified or attenuated by the sample on the interface. This interaction of the evanescent field with the sample manifests as a change in the frequency dependent reflectivity which is then used to characterize the sample's optical constants [10].

Several centuries after the discovery of the evanescent wave by Newton, Harrick and Farenfort [11], proposed and independently developed theories for internal reflection spectroscopy (IRS). In the year 1960, Harrick described multi-path theory for IRS whereas Fahrenfort demonstrated the usefulness of a single reflection IRS technique. Historically, the term "attenuated total reflection" spectroscopy first coined by Farenfort has been used interchangeably with internal reflection spectroscopy [10].

ATR is routinely used with other spectroscopic techniques for the characterization of a wide range of samples such as thin films, liquids, powders, polymers to name a few. ATR requires minimal to no sample preparation and is amenable to various sample types. Commercial ATR spectrometers are sold with various options and accessories to support different types of samples or analytes. ATR is often used in the pharmaceutical industry for analyzing powdered targets [12]. It serves as a diagnostic tool for applications in Forensic science [13] specifically for detecting and analysis of illicit drugs (e.g. cocaine.)

1.3.1 ATR at THz frequencies

ATR in conjunction with THz-TDS was first implemented by Hirori *et.al* at THz frequencies. THz-ATR is advantageous over conventional THz-TDS in that THz-ATR can characterize samples that are ordinarily difficult to characterize using transmission spectroscopy such as optically thick materials, powdered samples, polar liquids or dielectrics that are highly absorbent. ATR in the THz region has been used to characterize polar liquids [14] and powdered solids that have applications in the biotechnology, pharmaceutical, and food industries [15].The evanescent field in ATR can couple to waveguide modes thus making ATR attractive for sensing applications, as shown in [16] where sensitive detection of adsorbates on waveguide surfaces were demonstrated. This gives an extended interaction length analogous to Harrick's multi-reflection technique. A miniature handheld ATR module was developed and tested for functionality using various powders and liquids [17]. ATR system using an integrated prism at terahertz frequencies has been reported with the claim of enhanced propagation efficiency via decreased Fresnel losses [18]. The integrated prism is self-contained in that it houses a terahertz emitter, a terahertz receiver, and an ATR prism. The terahertz waves propagate in a closed environment in the absence of air and therefore the measurements are not affected by ambient water vapor. More recently, an imaging technique using ATR was demonstrated [19] by raster scanning a silicon sample mount on the ATR prism which can be mechanically moved to generate an image.

1.4 Metamaterials

The development of a new class of artificial structured materials called metamaterials (MM) has been the topic of recent interest in the electromagnetic community since its first experimental demonstration in microwave frequencies. Metamaterials are artificial structured composites typically comprised of patterned sub-wavelength ($\sim\lambda/10$) metallic inclusions arranged periodically on dielectric/semiconducting substrates. The 2D analogues of metamaterials are commonly known as metafilms (MF) or meta-surfaces. The electromagnetic behavior of these composites differs from the constituent materials which can provide an effective medium response if the wavelength is large with respect to the unit cell. The response is dictated by the geometry, orientation, shape and arrangement of the unit cells. Material properties such as ε and μ can be considered as effective only when the dimensions of the structure are much smaller than the incident wavelength. Much of this interest has been sparked by exploring metamaterials for novel phenomena such as negative index, perfect lenses, invisibility cloaking and artificial magnetism [20, 21].

In 1968, Veselago considered the possibility of a hypothetical material with negative constitutive parameters i.e. simultaneous negative permittivity ε and negative permeability μ [22]. Such materials are termed as left-handed materials (LHMs) or negative index materials (NIMs). In a left-handed material, E, H, k form a left-handed triplet. Such material properties are not readily available in nature. In naturally occurring materials, the EM response is governed by two constitutive parameters namely frequency dependent electric permittivity $\varepsilon(\omega)$ and the frequency dependent magnetic permeability μ(ω). They are both positive leading to a positive refractive index defined by $n = \sqrt{\varepsilon\mu}$. Metals exhibit a negative electrical permittivity. Likewise naturally occurring materials such as ferromagnets display a negative magnetic response. No naturally occurring material has demonstrated this behavior yet therefore a composite material that exhibit simultaneous negative electromagnetic behavior is of considerable interest.

A common feature of the metamaterial approach is in the engineered resonant element. In 1999, Pendry proposed an artificial medium comprising of an array of split ring resonators that exhibits a negative magnetic response over a range of frequencies in line with Veselago's predictions [21]. The first experimental realization of the simultaneous existence of –ε and -μ was in 2000 when Smith *et al.* experimentally demonstrated a composite medium consisting of metallic wires and split ring resonators did exhibit negative refraction ($\varepsilon < 0$ and $\mu < 0$) region at microwave frequencies [23]. Implications of having left-handed materials could lead to dramatically different behavior on well-known phenomena such as anomalous reflection, reversal of negative refraction, Doppler shift and Cherenkov radiation [22].

Since then, over a decade of research in metamaterials with incremental refinements to early experiments and exploring these unique properties has given rise to a multitude of potential applications over a wide region of the EM spectrum from RF through near- visible regimes [24]. The dimensions of the conducting elements in these artificial structures are easily scalable with frequency although there are limitations to the scaling giving rise to saturation of the resonant magnetic response at higher frequencies

[25] and unavoidable increase in losses in metallic structures as optical frequencies are approached.

The following paragraphs briefly describe major developments over the recent years in electromagnetic metamaterials.

1.4.1 Electromagnetic MM

With preliminary research focused on the microwave regime, metamaterial research has rapidly advanced into the terahertz and optical regimes. The EM response of metamaterials can be designed over a large region of the EM spectrum and depends on the collective response to either or both the electric and magnetic components of the incident electromagnetic radiation. Due to the scale invariance of Maxwell's equations, SRRs are scalable across frequencies and can be easily fabricated by conventional lithography suitable to the spectral range. Optical metamaterials suffer from losses associated with metals and limitations due to the current fabrication technology that may impact device performance. Metals no longer behave as perfect conductors at optical wavelengths. The continual push towards higher operating frequencies also places demands on improved characterization techniques. Emerging areas of research include non-linear metamaterials, plasmonic metamaterials, superconducting metamaterials, and dispersive metamaterials for slow light applications to name a few [26]. Low-loss alternatives to metals such as graphene and other superconducting oxides are also being sought [26]. Non-linearity can be introduced either by replacing the dielectric with a Kerr-type non-linear medium or by utilizing non-linear components such as diodes [27]. While the implementation of 2D planar structures is established from the GHz to optical frequencies, assembly of complex 3D metamaterials is challenging especially at higher frequencies since bulk 3D metamaterials demand advanced fabrication techniques. Recent efforts have focused on assembling bulk metamaterials. Advances in that direction have been made such as a layer by layer fabrication method for manufacturing 3D metamaterials has been demonstrated at optical frequencies [28]. 3D THz metamaterials referred to as standup metamaterials fabricated on flexible substrates was demonstrated using multilayer electroplating technique [29].

The following paragraph highlights some of the progress in electromagnetic metamaterials that are designed to operate at terahertz frequencies. As with all new directions in science, the initial enthusiasm for this topic has been enormous resulting in a vast array of publications with a staggering array of conclusions. The sheer volume of literature prevents a full exhaustive review beyond the pertinent topics and seminal papers.

1.4.1.1 Terahertz metamaterials

The capability to engineer material properties is even more important at THz frequencies where a wide range of material behavior is not as readily available as the neighboring microwave and optical spectral regions. Planar Terahertz metamaterials are realizable using current photolithographic techniques. The first demonstration of magnetic response at terahertz frequencies was by Yen *et al* [30] in 2004 using ellipsometric techniques. Inspired by the promise of negative index materials, metamaterial research has resulted in the development of MM-based THz devices such as THz modulators, filters, perfect absorbers, compact antennas, polarization rotators and many more [31-36]. The resonant response is fixed by the SRR geometry and the substrate.

The quest for achieving tunable and switchable functionalities makes active THz metamaterials an extremely fertile research area. Tunable MMs offer promising alternatives to terahertz switches and ultrafast modulators. The resonant electromagnetic response of MMs can be tuned by application of external control parameters such as electric field, magnetic field, optical illumination, temperature or even mechanical control. A dynamically controlled resonant electrical response was achieved by modifying the dielectric constant of the high resistivity GaAs substrate thus tuning the capacitive response via photoexcitation of charge carriers in the substrate [37]. Thermal tuning of the resonant frequency has been demonstrated on planar THz metamaterial consisting of split ring resonator array made from high transition superconducting films such as YBCO [38] instead of conventional metal films. The temperature-dependent modulation of the resonant response of the superconductor YBCO metamaterial array fabricated on sapphire substrate near the critical temperature could possibly lead to a low loss THz switch. Another method of tuning using thermal control has been accomplished by blending the concept of MEMS with MMs. Planar metamaterials were fabricated on "bimaterial cantilevers that are designed to bend out of plane in response to a thermal stimulus [39]". A tunable electric or magnetic response was observed that depends on the reorientation of the SRR elements within the unit cells.

The ability to slow and trap light by exploiting the nonlinear phenomenon of electromagnetically induced transparency (EIT) using planar metamaterials has gained immense popularity in recent years across several frequency bands. It promises unique and fascinating solutions to information storage, quantum computing and sensing [40]. EIT-like behavior was demonstrated at THz frequencies by integrating photoconductive silicon into the metamaterial unit cell [41].

A review of recent developments in the field of THz metamaterials can be found in review articles such as [42, 43] and references therein.

The advances in the development of THz metamaterials can play an important role leading to novel and functional THz devices and thus filling the ever shrinking “THz gap”.

1.5 THz Attenuated Total Reflection and Metamaterials

Coupling terahertz radiation to waveguide modes in metamaterials was shown by using the ATR technique in the Otto configuration [44]. This was inferred from the ATR measurements. More recently, leaky modes were observed on composite right/left handed (CRLH) metamaterial waveguides using Otto ATR configuration.

This is a merging area of study by bringing together these three separate fields, namely terahertz technology, ATR and metamaterials. Subsequently there is not a large body of literature dealing with specific techniques, pitfalls and interpretations of results.

1.6 Outline of Dissertation

Chapter 2 provides a brief summary of the experimental technique used in THz-Time domain spectroscopy. A THz time domain spectrometer based on photoconductive antennas is discussed. Typical results from a standard THz-TDS system are presented along with a procedure for extracting optical constants from standard measurements.

Chapter 3 describes the ATR technique. Fundamentals of attenuated total reflection technique are summarized in this chapter.

Chapter 4 discusses metamaterials, briefly touching on fundamental concepts.

Chapter 5 goes into details about the THz-time domain spectrometer modified to suit the measurement undertaken. Aligning a THz ATR ranging system is an important task especially when using a high index prism that modifies the system geometry. Issues and challenges in implementing THz-ATR in a fiber coupled THz-TDS setting are presented. Elaborate procedures developed to overcome these challenges are laid out.

Chapter 6 describes the experimental results obtained by using THz-ATR on metafilms, specifically the re-radiation across the total internal reflection boundary.

Chapter 7 presents potential theories to help explain the observations showcased in Chapter 6. Detailed results using full wave numerical simulations and Floquet and Moment Method approaches are presented. These treatments qualitatively explain the origin of the observed re-radiation in metafilm arrays.

Chapter 8 summarizes and concludes the work done in this research. It provides an outlook on future directions for this research.

2 Terahertz Technology

This chapter presents a discussion of the main experimental technique used in this work, specifically Terahertz Time Domain Spectroscopy (THz-TDS) that uses a pump-probe system with photoconductive antenna structures for THz generation and detection. Additionally, an overview of the developments in terahertz components is provided.

The development of ultrafast lasers and the introduction of the Auston switch [45] over two decades ago has led to a surge in research at terahertz frequencies giving rise to a vast number of potential applications. With rapid development of tunable sources and detection techniques and advances in novel ultrafast sources, there has been continuing interest to explore multi-disciplinary scientific and engineering phenomena thus stimulating a lot of activity in this part of the electromagnetic (EM) spectrum.

There are a variety of coherent terahertz sources. They can be classified into two broad categories 1) Continuous wave (CW) sources and 2) Pulsed sources. CW sources are inherently narrowband and are typically high-power sources. Some of the CW sources are free-electron sources such as backward-wave oscillators (BWO), gyrotrons, synchotrons, and of course, free electron lasers (FEL). There are also quantum cascade lasers, photomixers, intrinsic Josephson junction using high temperature superconductors [46], and other solid state devices such as resonant tunneling diodes, GUNN diode etc. [7, 47] . Pulsed sources which are broadband in nature and typically have low average power yields include gated photoconductive switches, and crystals employed in optical rectification techniques. This work will focus on the pertinent techniques for pulsed THz measurements.

2.1 THz Generation

Terahertz pulsed generation techniques can be classified into two categories; 1) photoconductive switching to generate electromagnetic transients on a sub-picosecond time scale and 2) second order non-linear processes such as optical rectification (OR). While the electro-optic (EO) rectification technique and photoconductive switching are the two most commonly used opto-electronic methods to generate pulsed THz radiation, another method used to generate THz radiation is the Photodember effect. The Photodember effect takes advantage of the difference in mobilities between the electrons and the holes [48].The diffusion of the electron hole pairs when excited by an ultrashort pulse creates dipoles leading to single cycle transients at THz frequencies. This effect is seen in high mobility semiconductors such as InAs and InSb [8].

Terahertz generation via optical rectification [49] is a second order non-linear effect where the terahertz radiation is generated due to difference frequency generation between the components of the ultrafast laser pulse. This method does not require application of a bias voltage and requires strict phase matching requirements for high conversion efficiencies. Zinc Telluride (ZnTe) is a widely employed EO material. More recently, high power terahertz radiation using non-linear techniques such as tilted phase front with lithium niobate ($LiNbO_3$) crystal [50] to generate powers as high as 10 μJ. The typical THz pulse energies generated from photoconductive antennas are on the order of

1–10 fJ [3].The success of photoconductive THz-TDS rests mainly upon the availability of signal averaging and time windowing of signals to become a viable scientific tool.

2.2 THz Detection

Free-space electrooptic sampling (FSEOS) based on Pockels effect [51] and photoconductive sampling are two popular detection schemes. In FSEOS, the probe pulse co-propagating with the THz pulse induces polarization rotation in the non-linear crystal, the magnitude and direction of which is recorded as the sign and amplitude of the THz field. This method can yield very high bandwidth [52]. Once again, factors such as the thickness of the crystal, phase matching and duration of the probe pulse impose limitations on the detected THz radiation.

Other measurement schemes include THz Differential Time Domain Spectroscopy (DTDS), THz interferometry mainly for thin film characterization and THz time resolved spectroscopy for studying carrier dynamics and transport [53]. This is primarily a variation in the sample and THz modulation compared to traditional TDS techniques. The following section discusses THz-TDS based on a photoconductive antenna source and detector in great detail.

2.3 Standard THz-TDS system

A typical THz-TDS system used to generate and detect short pulses of terahertz radiation using photoconductive antenna utilizes the experimental setup shown in **Error! Reference source not found.**. It is comprised of an ultrafast excitation source, a THz source (transmitter), THz detector/receiver and collimation and energy collecting optics.

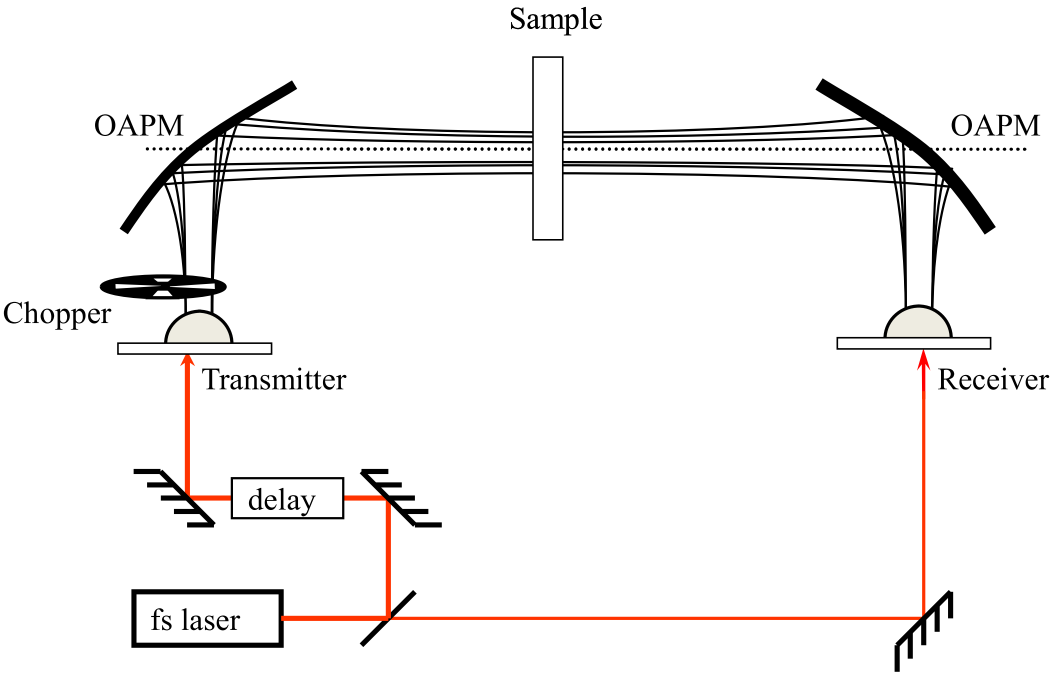

Figure 2-1 Experimental setup of a THz-TDS system. Off-axis paraboloidal mirrors (OAPM), Beam Splitter (BS) [54].

The conventional THz-TDS system uses a pump-probe approach where a passively mode-locked laser generates femtosecond pulses at a high repetition rate. A frequency doubled solid state pump laser drives the ultrashort laser. The femtosecond laser is split into two beams, one pulse train with a variable delay directed to the THz transmitter and the other with a fixed delay going to the THz detector. However unlike a pump-probe system where typically the high powered beam (pump beam) is directed onto a sample and the low powered beam probes the sample response, the transmitter in a TDS system receives a lower optical power than the receiver. A mechanical delay line is used to change the time delay between the THz transmitter and the receiver. The delay line is typically located in the transmitter path rather than the detector line since the receiver is more sensitive to optical beam alignment.

The transmitter antenna structure shown in Figure 2-2(a) is a pair of DC biased coplanar transmission lines 10 µm wide, fabricated on semi-insulating GaAs substrate using conventional photolithography. The transmission lines are separated by a gap of 80 µm. Typical bias voltages are 40 to 100 V.

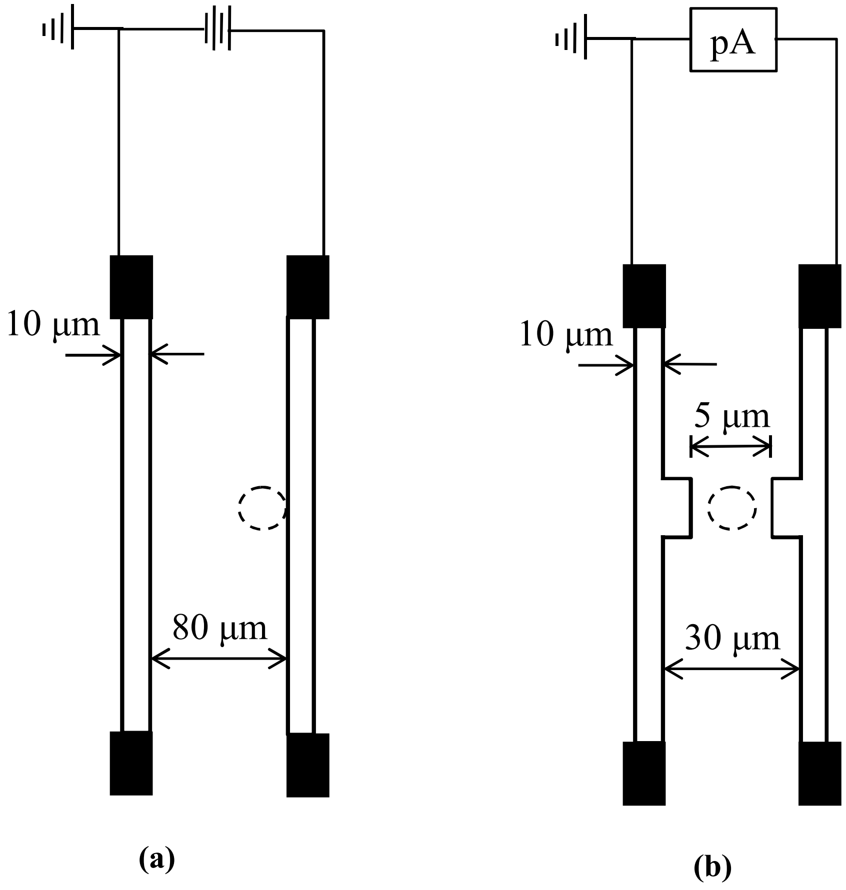

Figure 2-2 a) Transmitter chip b) Receiver chip. Laser excitation spot shown as a dashed circle.

Photo-excitation of the gap with the beam from ultrafast laser delivering <100 fs pulses centered around 800 nm results in the generation of photocarriers. Consequently acceleration of the carriers in the local MV/m fields [55] generates a near single cycle electrical current pulse. The photoconductive antenna behaves like a Hertzian dipole

[56].The current pulse radiates an electromagnetic pulse at THz frequencies which is then collimated by a spherical high-resistivity silicon lens contact mounted on the back side of the transmitter chip. The terahertz radiation propagates through free space. This radiation is steered and collimated by off-axis paraboloidal mirrors (OAPM) arranged in near-confocal symmetry and is then focused onto the THz receiver.

The receiver antenna structure also fabricated using conventional photolithographic techniques is similar to that of the source antenna. A typical THz detector photoconductive antenna in stripline geometry seen in Figure 2-2(b) consists of two coplanar strip lines on a short lifetime semiconductor substrate. The detector strip lines have a dipole antenna structure with a photoconductive gap of 5 μm. These lines nominally have linewidths 5 to 10 μm and a 10 to 50 μm wide separation between them. The separation determines the bandwidth of the detector with large antennas having more sensitivity at the expense of bandwidth, and the smaller antennas having greater bandwidth, but reduced signal strength.

Choice of substrates for the photoconductive source is dictated by properties such as high mobility and high breakdown field leading to rapid charge acceleration and fast rise times. A widely used material for the THz emitter is a GaAs substrate. The photon energy of the commonly available Ti:sapphire laser source at 1.55eV is greater than the bandgap energy of 1.43 eV of the GaAs emitter . Electron hole pairs in the substrate are created when pumped with femtosecond laser pulses. Substrates with short carrier lifetimes are desired for THz receivers for e.g. radiation damaged silicon on sapphire (SOS) with lifetime of 600fs [57]. The carrier lifetime for Lt-GaAs can range between

0.3-1.1ps and is dependent on fabrication parameters [58, 59]. A modification to the standard receiver antenna used for the work reported in this document is a superlattice formed by self-assembled erbium arsenide (ErAs) nano islands embedded in GaAs substrate [60] which will be covered in a later chapter.

When the receiver is synchronously gated by an optical pulse, the electric field of the incident THz radiation creates a transient bias across the gap in the receiver antenna structure, thus inducing a current that is amplified by a low noise current amplifier. The output from the current amplifier goes to the lock-in amplifier which isolates the signal at the reference frequency of the modulated THz beam. An optical chopper modulates the generated Terahertz beam at the transmitter which is phase locked to the lock-in amplifier. This current is proportional to the received THz field. The terahertz waveform is mapped out by varying the relative delay between the optical pulse and the THz pulse on the receiver.

A typical terahertz pulse obtained from a THz-TDS system is shown in Figure 2-3. It is a near single cycle pulse lasting a few picoseconds with the FWHM of the main peak of the single cycle pulse equal to 0.4 ps. The system is purged to a relative humidity 1.9 % to suppress the effect of water vapor absorption lines.

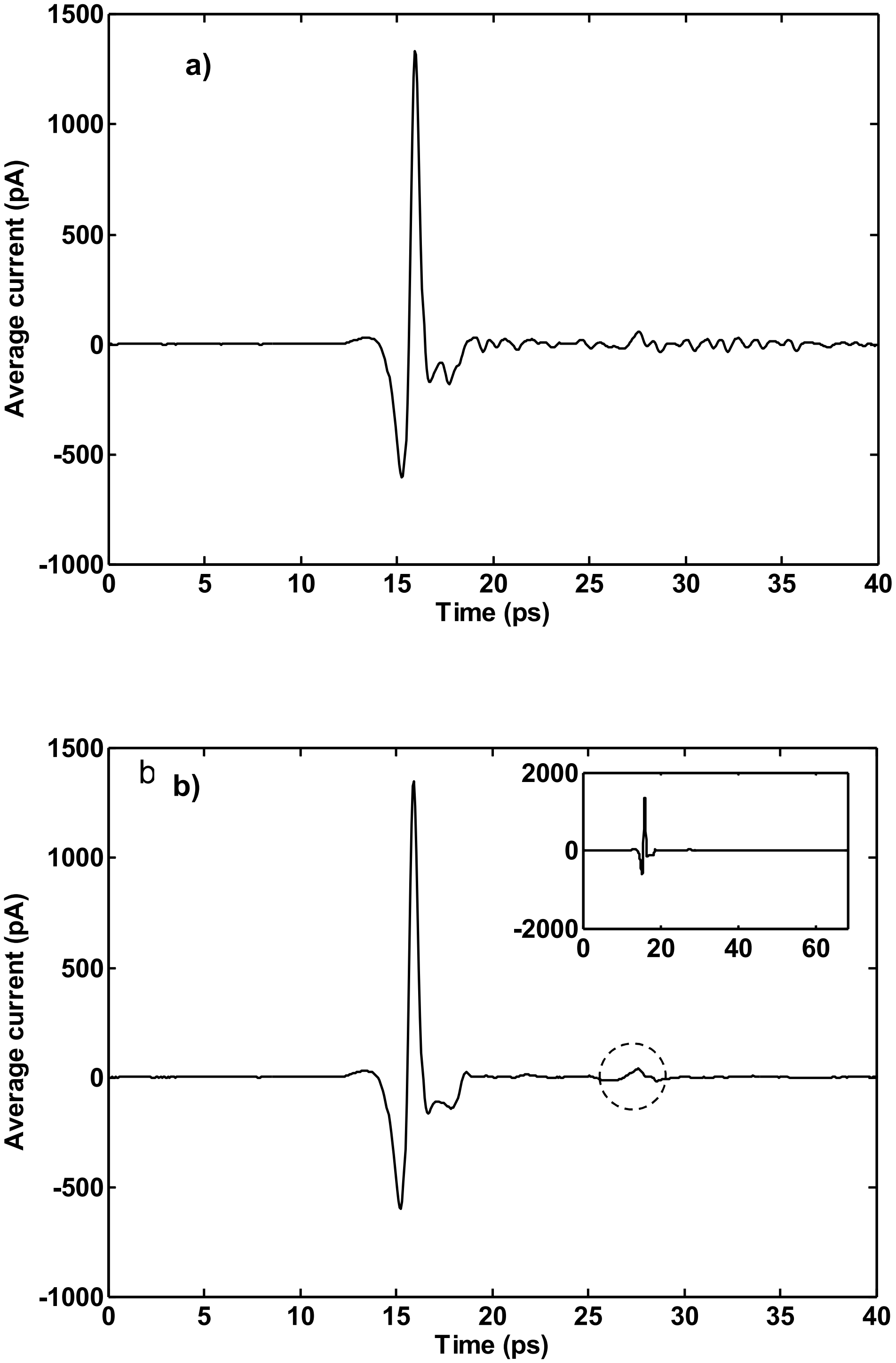

Figure 2-3 THz pulse measured in a THz-TDS system a) in humid air b) under nearly dry conditions with relative humidity of 1.9%. Inset in part b) shows full length of the measurement scan.

A small blip near 28 ps (dashed circle in Figure 2-3b) is due to internal reflections from the source chip. By comparing the arrival times of the reflection and the main pulse, the thickness of the source chip can be calculated to be 487 μm assuming a frequency independent refractive index of 3.6 for the GaAs substrate (500 μm thick). Additional reflections appear in the time domain measurements. Optical reflections within the substrate of the receiver modify the gating response and cause a pre-pulse earlier in time. The pre-pulse is not a problem when one is able to time window the measurement. Optical reflections in the transmitter substrate create a secondary THz pulse that appears later in time and can cause structure on the resultant spectrum. A substrate and lens system made from the same material would be ideal, but is typically unfeasible. Hence a thick substrate on the transmitter is preferred to reduce the "small blip" and clean up the spectrum.

The numerical Fourier transform of the temporal pulses in Figure 2-3 yields the corresponding spectra plotted in Figure 2-4. The spectrum peaks near 0.5 THz. The spectral amplitude extends from 0.1 to 2.5 THz, with a usable bandwidth of approximately 2 THz.

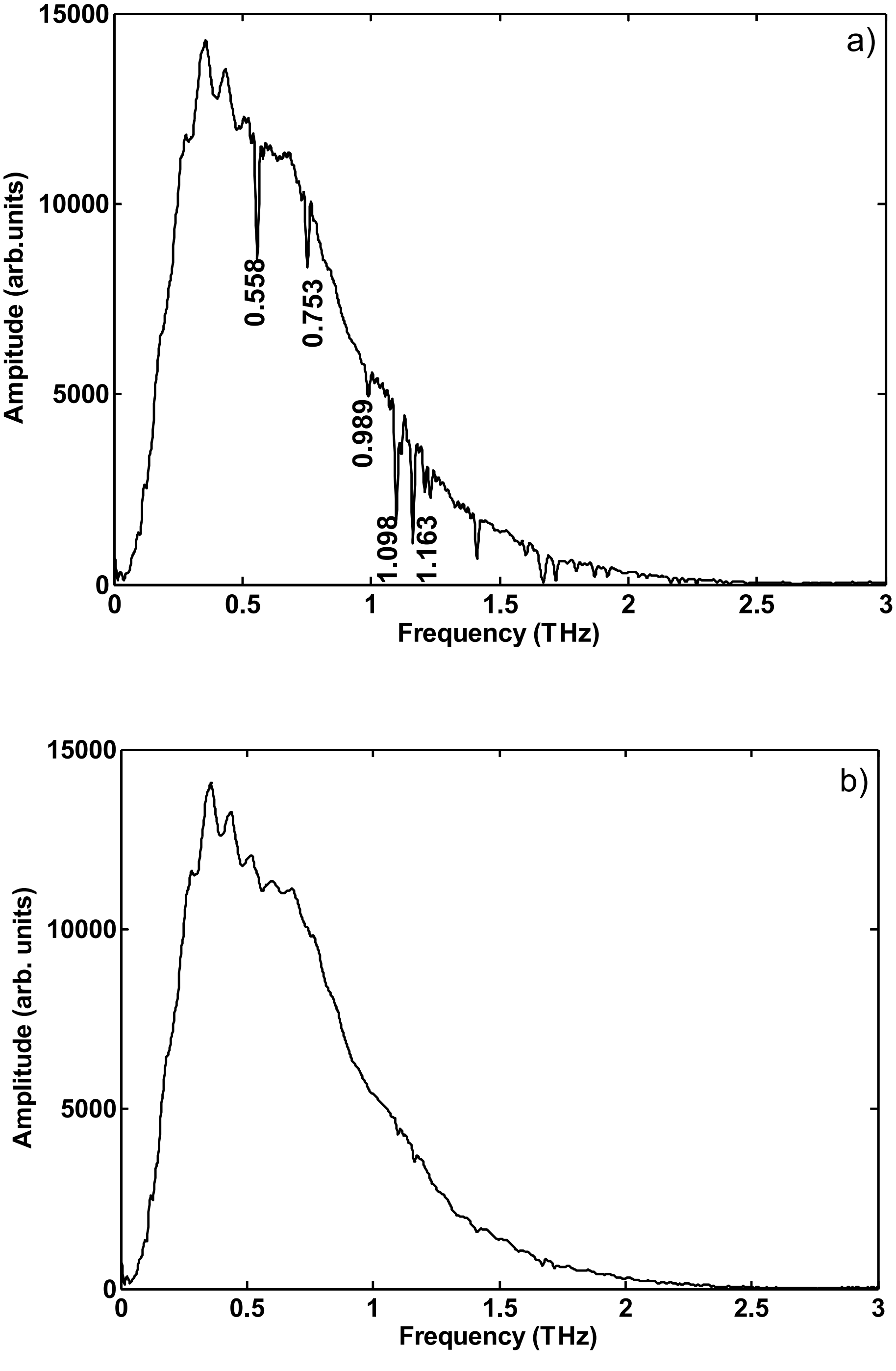

Figure 2-4 Numerical Fourier transform of Terahertz pulses from Figure 2-3.
a) In ambient humid air and b) under nearly dry conditions with relative humidity of 1.9%

Figure 2-4(a) show the effect of residual ambient water vapor in the THz pulse beam path. The measured spectrum shows the presence of some absorption lines due to water vapor, with the strongest features located at 0.558 THz, 0.753THz, 1.098 THz and 1.163 THz. Figure 2-4b corresponds to a measurement in nearly dry air containing 1.9 % water vapor.

2.4 Analysis of THz-TDS data

A typical TDS measurement in transmission involves placing the sample to be characterized at the focal plane between the transmitter and the receiver. This requires the sample to be relatively transparent to THz radiation and the terahertz beam to be entirely in the sample. It also requires knowledge of the sample thickness. The changes in the temporal field with and without the sample can be used to determine the material properties. The reference is either taken without a sample or using a suitable substrate. The Fourier transforms of the sample and reference time scans namely $E_{sam}(\omega)$ and $E_{ref}(\omega)$ gives $t(\omega)$ which is complex transmission due to the sample. The phase difference between the sample and the reference waveforms is a measure of the index of refraction of the material.

$$t(\omega) = \frac{E_{sam}(\omega)}{E_{ref}(\omega)} \tag{2.1}$$

The index of refraction and the absorption of the sample are extracted from the magnitude and the phase of the above ratio. The complex index of the material is given by

$$n(\omega) = n_r(\omega) - in_i(\omega) = \frac{\ln t(\omega)\lambda}{i2\pi\Delta z} + 1 \qquad (2.2)$$

where Δz is the sample thickness. The above analysis ignores the effect due the Fresnel reflections from the front and back surfaces of the sample [54].

The change in amplitude between the measured sample and reference waveforms gives rise to the absorption per unit length due to the sample using the following equation. The field absorption coefficient is given as $\alpha = \frac{n_i\omega}{c}$ and expressed in terms of the complex transmission as

$$\alpha(\omega) = \frac{-1}{\Delta z}\ln\left(t(\omega)\right) \qquad (2.3)$$

Thus the optical constants of the material are obtained without the need for Kramers-Kronig analysis [55].

The direction that led this research was toward explaining the physical basis of the observed phenomena rather than extraction of optical constants of the metamaterial.

3 Attenuated Total Reflection

This chapter presents an overview of the attenuated total reflection (ATR) technique with a brief description of the key components of an ATR spectrometer. The main focus for this overview is on employing ATR in conjunction with THz spectroscopy. ATR is a well-established technique and a comprehensive overview lies outside of the scope of this endeavor.

ATR, also referred to as Internal Reflection Spectroscopy (IRS), is a sampling technique used together with spectroscopic methods in many spectral regions. Light undergoes total internal reflection at the interface of an optically dense medium when it is incident beyond the critical angle and creates an evanescent wave. An absorbing sample in intimate contact with the total internally reflecting surface interacts with the evanescent field. The internal reflection is attenuated since energy is absorbed by the sample in contact with the high index medium. The measured changes in reflectivity with and without the sample can provide information about the sample's material constants. The strength of ATR lies in the ability to characterize materials that are ordinarily difficult to characterize using transmission spectroscopy such as optically opaque powders and liquids thus offering qualitative and/or quantitative information about the material. Due to the superposition of the incident and the reflected fields at the ATR surface, the field is largest at the boundary. This property can be exploited for sensing applications. ATR spectra resemble transmission spectra [10] although there are quite a few subtle differences. These will be addressed in a later section.

Some of the advantages of the ATR technique [15] are

1. Ease of use
2. Speed
3. Minimum sample preparation compared to other techniques; ability to characterize liquids and powdered samples without dilution, mixing or compression into pellets.
4. Non-destructive
5. Potentially *in-situ* technique.
6. Thick and strongly absorbing samples can be analyzed since the sampling length is determined by the evanescent wave which penetrates only a few microns into the sample.

And some of the limitations of ATR are listed below.

1. Quality of contact of the sample with the ATR crystal. There must be good contact between the sample and the ATR prism since the evanescent wave decays rapidly with distance from the surface of the prism. Deposition of sample as films on the crystal surface or physical contact either by pressure or using a clamping mechanism. There could be artifacts resulting from pressure contact. These issues are discussed in more detail in a later chapter.
2. Modification of transmission experimental configurations to support ATR is not trivial. Typically dedicated systems must be constructed.

3. Correction algorithms to extract equivalent transmission spectra from ATR spectra are not well-known and easily accessible for all spectral ranges.

The ATR measurement depends on the type and the refractive index of the internal reflecting element (IRE), refractive index of the sample, critical angle, sample contact with the IRE, number of reflections and penetration depth [10]. Careful consideration of these parameters is important in successfully implementing the ATR technique and in achieving accurate and reproducible spectral information.

3.1 ATR configurations

Two commonly implemented ATR geometries are 1) Otto configuration and 2) Kretschmann geometry. Figure 3-1 shows a schematic representation of these configurations.

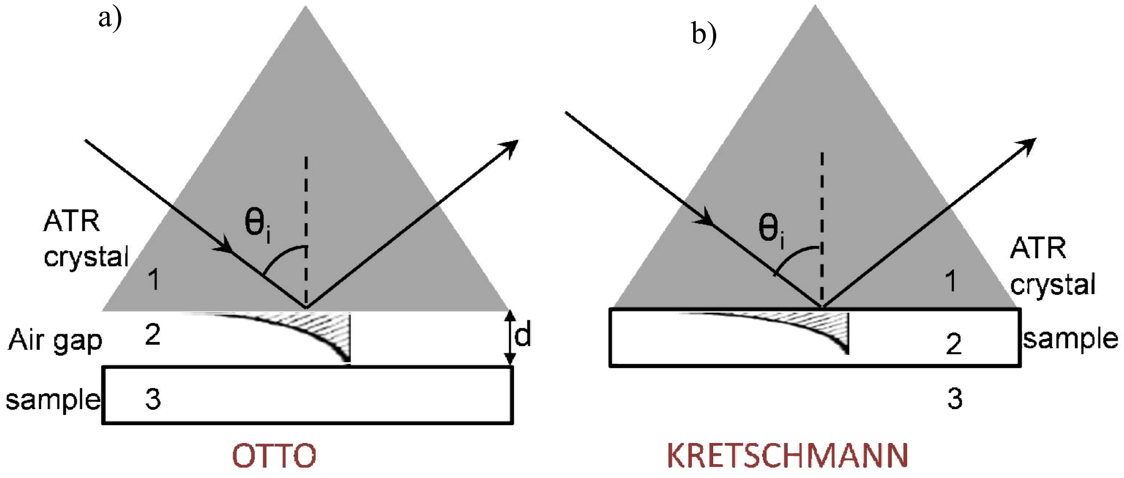

Figure 3-1 ATR geometries a) Otto b) Kretschmann, adapted from [61].

In Kretschmann [62] configuration, the sample is in optical contact with the high index prism as shown in Figure 3-1(b) whereas in the Otto[63] configuration, the sample is separated from the prism by a dielectric or an air gap as seen in Figure 3-1(a). The Kretschmann geometry is the configuration that will be applied in the experiments described in this work.

3.2 Internal reflecting element

Internal reflecting elements (IRE) are optically transparent materials with high index of refraction used in ATR. Some of the popular IREs used in implementing ATR are shown in Table 1. For reference, 1 THz corresponds to 300 μm or 0.3 mm.

Material	Spectral range (μm)	Refractive index	Critical Angle θ_c	Penetration depth [64] for λ=10 μm (μm)
Silicon	1.1-150	3.42	17.01° (n_2 = 1)	0.85 25 (at λ=300 μm and n_2 = 1)
Germanium	2-12	4	22.02°	0.66
ZnSe	0.5-15	2.41	38.5°	2.01
Quartz	0.3-2.3	1.43 [10]	--	--
Sapphire (Al_20_3)	0.4-5.5	1.7 [10]	62°	--
KRS-5 (thalium bromoiodide)	0.5-40	2.4	38.5°	2.13
Diamond	0.2-4	2.4	38.5°	2.01
Teflon[14]	300-150	1.4	46° (n_2 = 1)	61.2 (at λ=300 μm ,for θ_i = 65° and n_2 = 1)

Table 1 ATR crystals. Adapted from references [10, 64-66]. Critical angle is calculated w.r.t sample index n_2 = 1.5 unless indicated. Penetration depth is calculated for θ_i = 45°**,** sample index n_2 = 1.5 and λ=10 μm unless indicated.

Selection of the crystals depends on optical and mechanical properties such as chemical inertness, hardness, desired spectral range and penetration depth. High resistivity Diamond is scratch resistant and tolerates a wide range of pH values. Silicon is an excellent material for infrared spectroscopy specifically for terahertz applications. It is robust and inert. High resistivity silicon shows low dispersion and low loss at terahertz frequencies [66]. MgO and plastic prisms were used in the work presented in [67] at THz frequencies.

The nature of the sample dictates the geometry of the crystal. Accordingly, they can be classified as single path and multi-path IREs. An illustration of a single reflection IRE using a right angled prism used in this work is shown in Figure 3-2(a). This is preferred for strongly absorbing samples and where sensitivity is not a problem. Another example of a single bounce crystal with a dove prism used in THz-ATR is shown in Figure 3-2(b). Here the incoming and outgoing radiation paths are collinear thus maintaining the optical axis of a linear system [14].

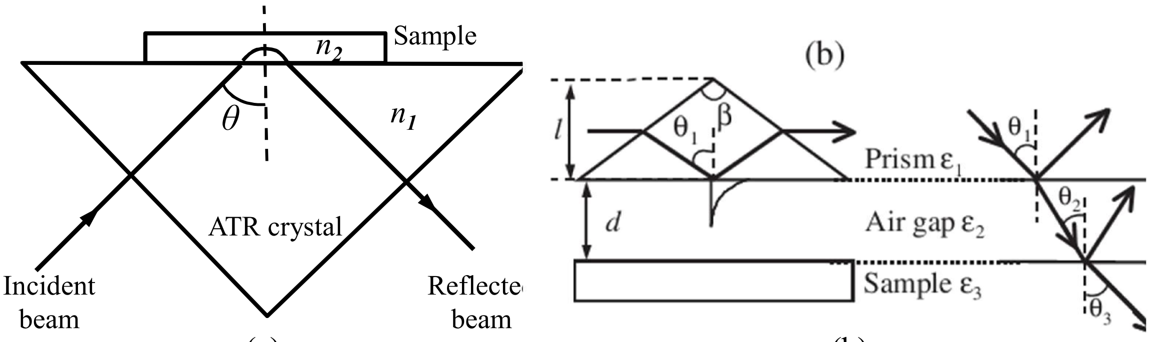

(a) (b)

Figure 3-2 Single reflection IRE a) Right angled prism b) Dove prism from [14]

A schematic of multiple reflections or multiple bounces in a trapezoidal ATR crystal is shown in Figure 3-3. These are more common in the case of weakly absorbing materials.

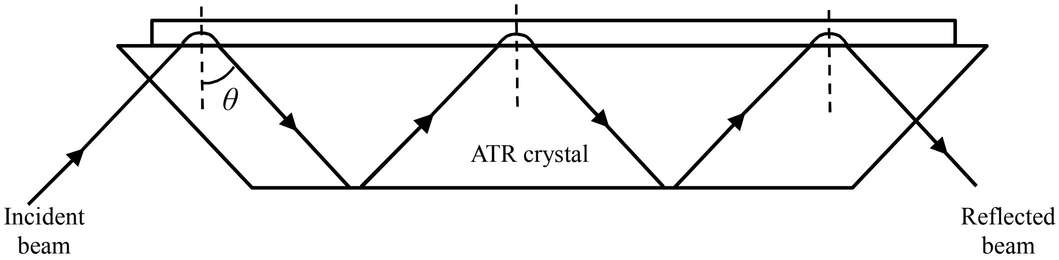

Figure 3-3 Schematic of a multiple bounce IRE [65]

The number of reflections depends on the length of the crystal and the angle of incidence. The spectral contrast proportionately increases with the number of reflections. Specially designed cells are used for analyzing liquid samples.

3.3 ATR Theory

3.3.1 Evanescent field

When light is incident from an optically denser medium n_1 into an optically rarer medium n_2, ($n_1 > n_2$) it undergoes total internal reflection when the angle of incidence is equal to or greater than a certain angle known as the critical angle [68]. Reflection from a boundary below critical angle (normal refraction), at critical angle, and beyond critical angle (TIR) is illustrated in Figure 3-4.

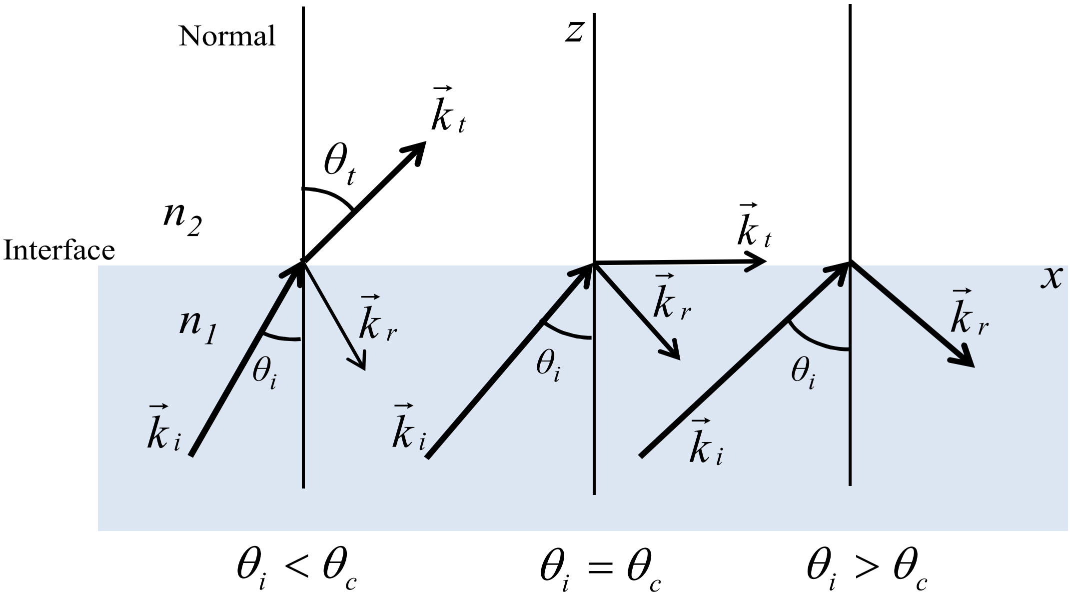

Figure 3-4 Three general cases for interaction with a planar interface

When $\theta = \theta_c$, $\theta_t = 90°$ and from Snell's law,

$$n_1 \sin\theta_c = n_2 \sin\theta_t \tag{3.1}$$

The critical angle is a function of the refractive indices of the sample and ATR prism and is defined as

$$\theta_c = \sin^{-1} n_{21} = \sin^{-1}\left(\frac{n_2}{n_1}\right) \tag{3.2}$$

For incident angles beyond critical angle i.e. $\theta_i > \theta_c$, $\sin\theta_t = \frac{n_1}{n_2}\sin\theta_i$ exceeds unity and therefore the transmitted angle θ_t is complex with the real part equal to π/2 radians [69].

In order to satisfy the boundary conditions, fields must be present on both sides of the interface, which leads to a complex transmitted wave vector. Assuming an *xz* plane of incidence as shown in Figure 3-4, the wavevector of the transmitted wave in medium 2 is given as

$$k_t = k_2(\sin\theta_t\hat{x} + \cos\theta_t\hat{z}) \tag{3.3}$$

The transmitted wave vector k_t has a component $k_{tx} = k_2 \sin\theta_t$ along the interface in the *x*-direction and a component $k_{tz} = k_2 \cos\theta_t$ perpendicular to the interface (*z*-direction) where $k_2 = \frac{2\pi n_2}{\lambda}$ is the wavenumber of medium 2.

Using a trigonometric identity,

$$k_{tz} = k_2 \cos\theta_t = k_2\sqrt{1-\sin^2\theta_t} \tag{3.4}$$

Using Snell's law,

$$k_{tz} = k_2\sqrt{1-\left(\frac{n_1}{n_2}\right)^2 \sin^2\theta_i} \tag{3.5}$$

For $\theta_i > \theta_c$,

$$k_{tz} = ik_2\sqrt{\left(\frac{n_1}{n_2}\right)^2 \sin^2\theta_i - 1} \equiv i\beta \tag{3.6}$$

Since the component perpendicular to the surface is imaginary, the transmitted field present in the semi-infinite rarer medium is evanescent. The evanescent field [68] can then be expressed as

$$\overline{E}_t = \overline{E}_{0t}e^{-\beta z}e^{i(k_{tx}x-\omega t)} \tag{3.7}$$

where E_{0t} is the initial transmitted field amplitude and $1/\beta$ is the decay length. Thus the evanescent field is a non-uniform plane wave that propagates parallel to the interface as a slow surface wave and decays exponentially normal to the surface (*z*-direction) into the rarer medium by a factor $e^{-\beta z}$. The polarization of the evanescent wave follows the polarization of the incident THz pulse (p- or s-polarized). There is no real energy transfer normal to the surface. Therefore, in that direction the time-averaged Poynting vector is zero [69]. Along the *x*-direction, it propagates with a phase velocity $c/n\sin\theta_i$. Under these conditions, the Fresnel reflection coefficient r becomes complex and there is 100% reflection for both s and p polarizations, i.e. the magnitude $|r|$ is unity. The Fresnel reflection coefficients for s (perpendicular) and p (parallel) polarized waves are given by the following equations [70].

$$r_\perp = \frac{\cos\theta_i - i\sqrt{\sin^2\theta_i - n^2}}{\cos\theta_i + i\sqrt{\sin^2\theta_i - n^2}} \tag{3.8}$$

$$r_\parallel = \frac{-n^2\cos\theta_i + i\sqrt{\sin^2\theta_i - n^2}}{n^2\cos\theta_i + i\sqrt{\sin^2\theta_i - n^2}} \tag{3.9}$$

where $n = \frac{n_2}{n_1}$.

3.3.2 Penetration depth

The penetration depth into the sample is the distance over which the evanescent field amplitude decays by a factor of 1/e from its amplitude at the reflection interface. [10]. The penetration depth is given by the equation

$$d_p = \frac{\lambda}{2\pi\sqrt{n_1^2\sin^2\theta_i - n_2^2}} \tag{3.10}$$

It is independent of polarization but depends on the wavelength of the propagating radiation, refractive indices of the denser and the rarer medium and the angle of incidence at the sample–prism interface. This work utilizes silicon prism as the ATR reflecting element with air as the rarer medium. Figure 3-5 shows the frequency dependence of the evanescent field penetration depth plotted for a silicon-air interface with 45° angle of incidence for THz frequencies.

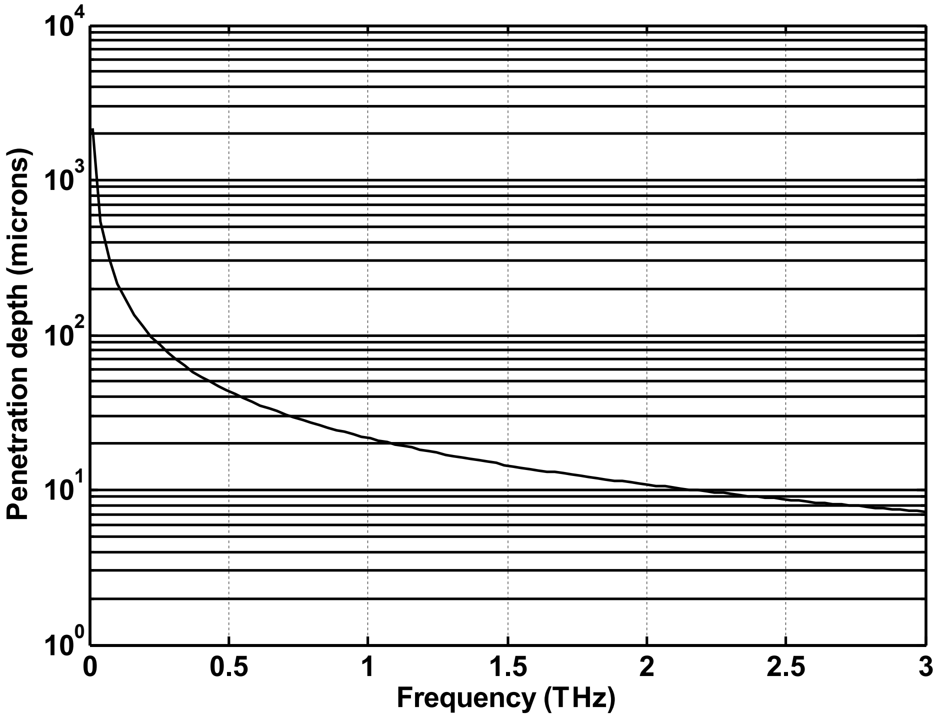

Figure 3-5 Penetration depth of evanescent field at 45° angle of incidence for silicon-air interface.

From Figure 3-5, the penetration depth of the evanescent field is 21.7 μm at 1 THz. The penetration depth decreases with increasing frequencies or shorter wavelengths. Larger penetration depths can be achieved by reducing the index change between the sample and the ATR prism for a fixed angle of incidence [see equation (3.10)]. The dependence of the penetration depth on the angle of incidence can be seen in Figure 3-6. This plot applies to the silicon-air interface with 1 THz incident radiation.

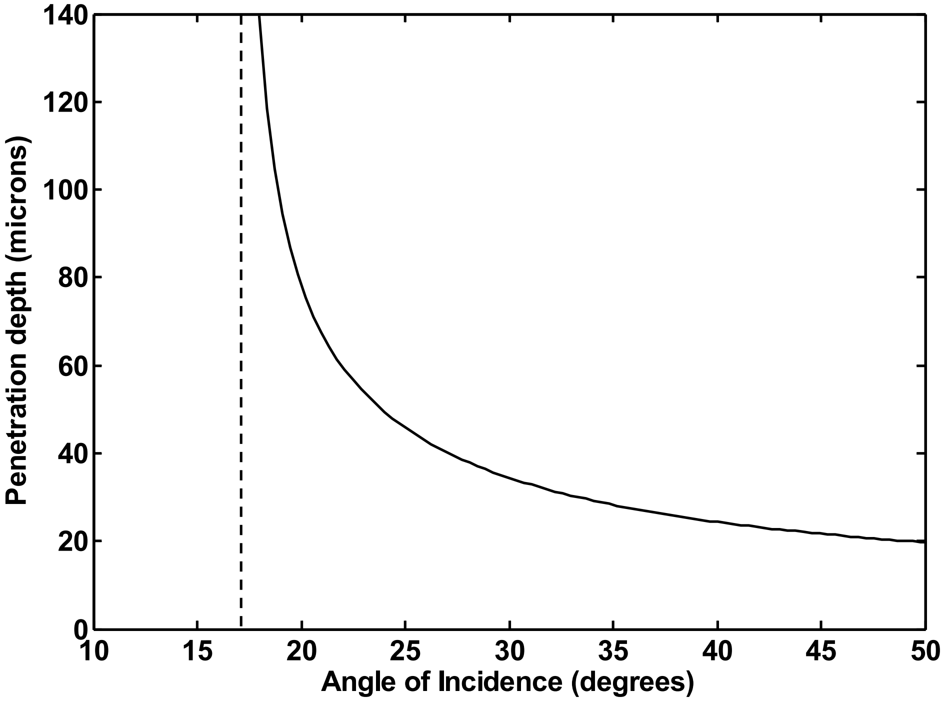

Figure 3-6 Penetration depth of evanescent as a function of incidence angle for silicon-air interface for 1 THz incident radiation.

The penetration depth increases as the angle of incidence decreases toward critical angle. The singularity shown with a dashed line corresponds to the critical angle of 17.01° for the silicon-air boundary. In theory, the penetration depth becomes infinitely large as θ_i approaches the critical angle θ_c. The SRR arrays used in this work have a typical height of 0.2 μm and the incident angle is fixed at 45°. Even with a high frequency of 1 THz, the penetration depth is > 20 μm. Thus for a 0.2 μm thick sample, the penetration depth will play a minimal role in the excitation of the fundamental *LC* resonance. This treatment assumes the Kretschmann configuration. In the Otto configuration, penetration depth would become an important parameter dependent upon the air gap spacing between IRE and sample.

3.3.3 Goos Hanchen *shift*

The phase shift associated with the complex reflectivity in a specular reflection scenario specifically when total reflection occurs, gives rise to a lateral shift known as the Goos-Hanchen shift [71]. Several theories were formulated to explain this phenomenon some of which include Artmann's stationary phase method [72] and theories by Lotsch [73] and Renard [74] based on energy conservation. Goos and Hanchen demonstrated experimentally this lateral displacement of the reflected beam with respect to the incident beam using a partially silvered glass prism thus agreeing with early predictions by Newton and Schaefer and Pich [75]. The beam displacement is proportional to the wavelength. A schematic representation of a bounded beam undergoing total internal reflection from denser medium 1 to rarer medium 2 is shown in Figure 3-7.

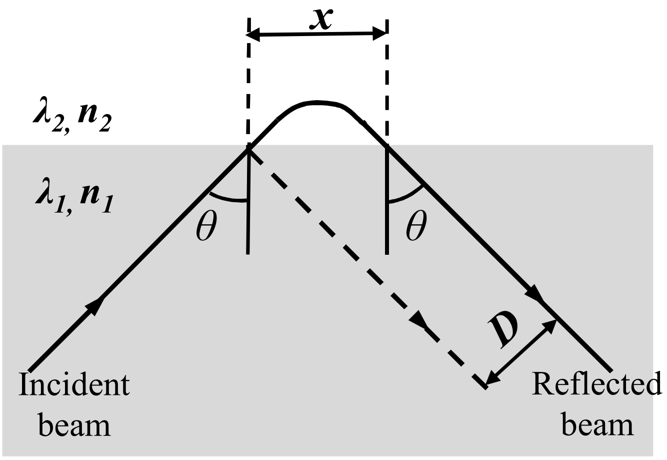

Figure 3-7 Schematic of the Goos-Hanchen shift *D* on total internal reflection. The dashed line on the reflected side of the normal represents the path taken by the reflected beam as predicted by geometric optics.

This phenomenon occurs for beams with finite widths of Δ*x*. A finite beam can be represented as a linear summation of plane wave components. As a consequence, the plane waves will obey the uncertainty relationship $\Delta x \Delta k_x \geq \frac{1}{2}$ leading to a non-zero spread in the k vector directions. Thus each plane wave component can experience a different angle of incidence on total internal reflection, therefore accumulate a different phase while satisfying the dispersion relation $k_x^2 + k_y^2 + k_z^2 = k^2$. The result of the relative phase shifts between the wave components comprising the incident and reflected beams gives rise to a net lateral shift (indicated by *D* in Figure 3-7) that is given by[72, 76]

$$D = -\cos\theta_0 \frac{d\varphi}{dk_x} = -\frac{\lambda}{2\pi}\frac{d\varphi}{d\theta} \tag{3.11}$$

The magnitude of the shift depends on the angle of incidence, polarization and wavelength of the incident light.

From the Fresnel equations, the phase change on total internal reflection for a s-polarized wave is given by

$$\phi_\perp = -2\tan^{-1}\left(\frac{\sqrt{\sin^2\theta_i - n^2}}{\cos\theta_i}\right) \tag{3.12}$$

and for a p-polarized wave;

$$\phi_\parallel = \pi - 2\tan^{-1}\left(\frac{\sqrt{\sin^2\theta_i - n^2}}{n^2\cos\theta_i}\right) \tag{3.13}$$

Equations (3.12) and (3.13) are only valid for $\theta_i > \theta_c$. Accordingly, the Goos-Hanchen shifts for the s and p-polarizations [76] can be expressed as

$$D_{\perp} = \frac{1}{\pi n_1} \frac{\lambda_1 n_2}{\sqrt{\sin^2 \theta_i - \sin^2 \theta_c}} \tag{3.14}$$

and

$$D_{\parallel} = \left(\frac{n_1}{n_2} \right)^2 \frac{1}{\pi n_1} \frac{\lambda_1 n_2}{\sqrt{\sin^2 \theta_i - \sin^2 \theta_c}} \tag{3.15}$$

Using equations (3.14) and (3.15) , the magnitude of the Goos-Hanchen shift for s-polarized and p-polarized is calculated for a silicon-air interface at 45° angle of incidence. The beam shift as a function frequency plotted for clarity on a logarithmic scale is shown in Figure 3-8.

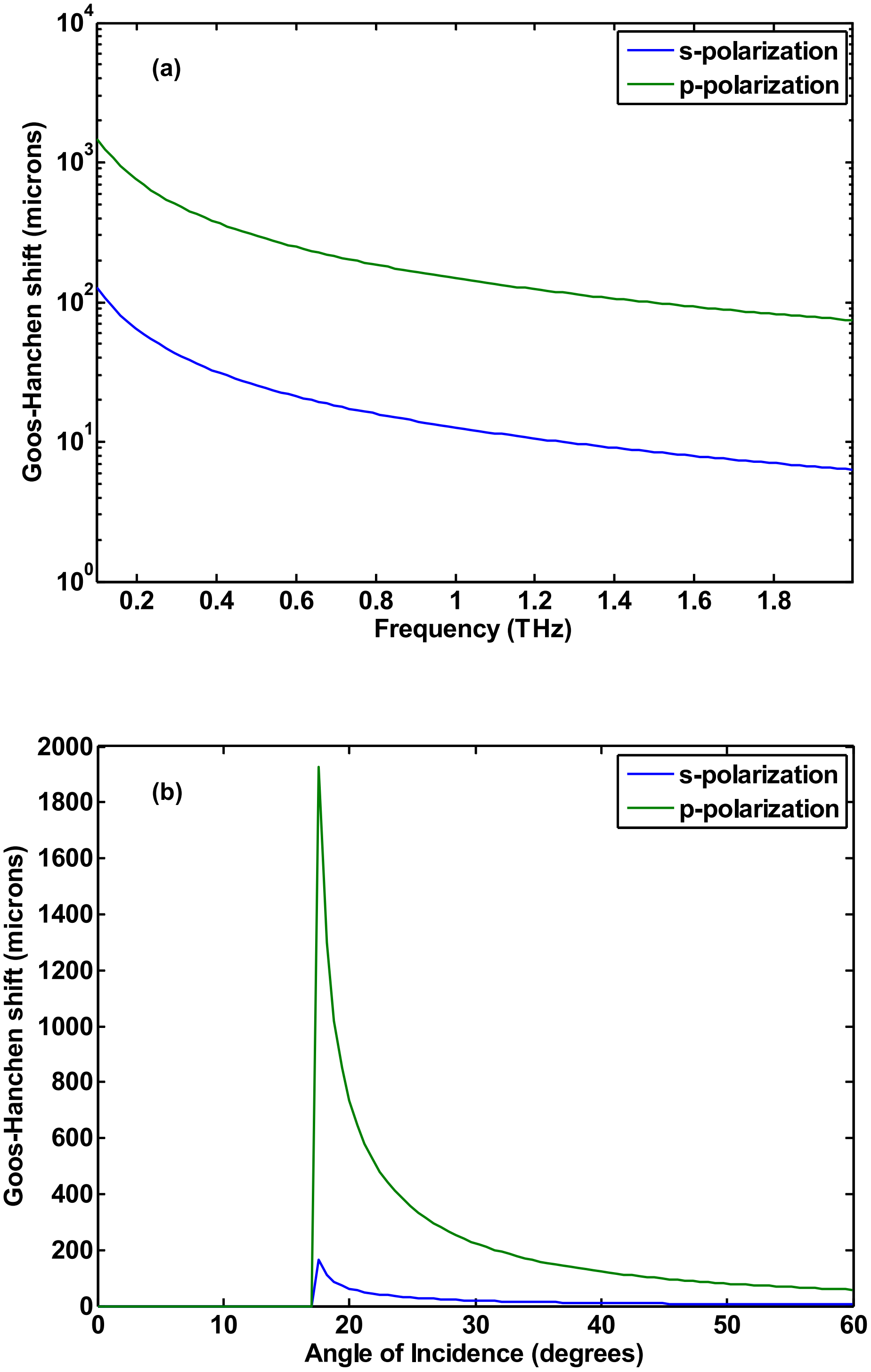

Figure 3-8 Goos-Hanchen shifts for s-polarization (blue) and p-polarized waves (green) plotted as a function of a) frequency for $\theta_i = 45°$ and b) incidence angle for a frequency of 1 THz.

The calculated Goos-Hanchen shifts as function of angle are plotted in Figure 3-8 b). From Figure 3-8 b), it can be inferred that for 1 THz, the shifts for s and p- polarized incident radiation are 98 µm and 8 µm respectively for a 45° incidence angle. Predicted by FDTD numerical modeling, a Goos-Hanchen shift has been indirectly observed in a FTIR geometry at terahertz frequencies [77] Predictions of "giant" Goos-Hanchen shifts have been made at the interface of right-handed and left-handed media [78, 79]. The effect of this lateral shift is not taken into account for the experimental results described in this work since the positioning uncertainty of the receiver arm is greater than the calculated GH shift. Measuring the Goos-Hanchen shift is not a trivial task and requires considerable precision and modification of the experimental setup. The shift can be amplified by using multiple reflections.

3.4 Comparison with transmission measurements

Often times, the ATR spectra qualitatively resembles a transmission spectra but in reality, there exist several differences. These differences manifest as spectral shifts and distortions in the intensities of the peaks at longer wavelengths (lower frequencies). Differences arise due to the wavelength dependence of the penetration depth. At longer wavelengths, the evanescent wave penetrates deeper into the sample. Therefore, the absorption bands at longer wavelengths (smaller frequencies) are stronger than those at shorter wavelengths (larger frequencies). An example of such a comparison from [13] is shown in Figure 3-9.

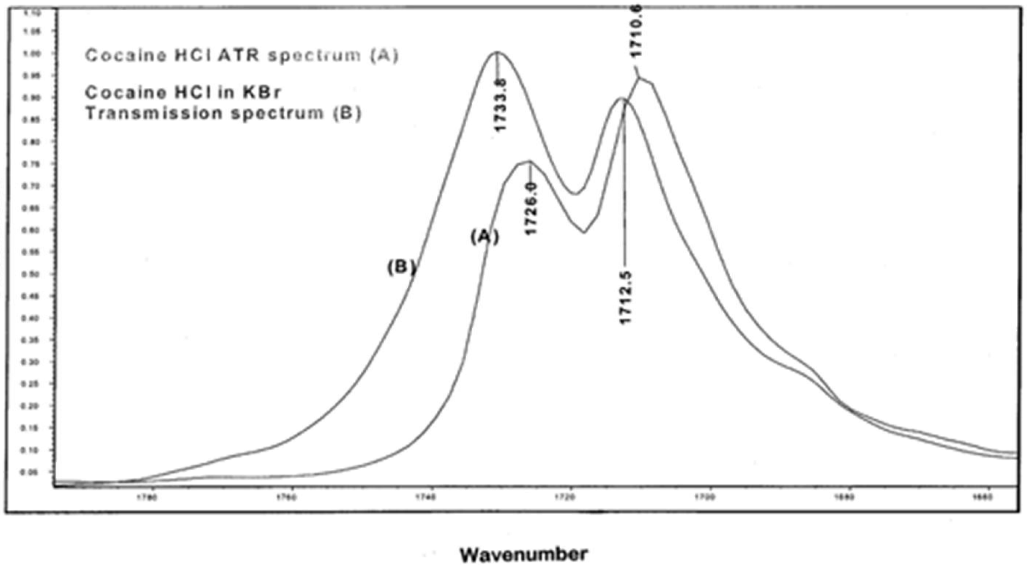

Figure 3-9 “The carbonyl band absorption of cocaine HCl showing the difference between ATR and absorbance spectra” [13]

In the next section, the differences will be discussed in more detail by introducing the concept of effective thickness in internal reflection spectroscopy.

3.4.1 Effective thickness

The concept of effective thickness plays a big role in the case of absorbing samples. It was developed to establish equivalence between the absorbance obtained by a transmission spectrum with that of the ATR spectra. This applies to most materials where the thickness of the rarer medium is greater than the penetration depth. The effective thickness and penetration depth are related by [10]

$$d_e = \frac{n_{21} E_0{}^2 d_p}{2\cos\theta_i} \tag{3.16}$$

“The effective thickness represents the thickness of sample material that would be required to give the same absorbance in a standard transmission experiment as obtained in IRS [80].” In transmission spectroscopy, the interaction of the incident radiation depends on the sample thickness. The transmission is related to the absorption coefficient by Beer-Lambert law which is written as $T = \frac{I}{I_0} = e^{-\alpha d}$ and ignoring losses due to reflection. Here d is the thickness of the sample and $\alpha = \frac{2n_i\omega}{c}$ is the power absorption coefficient, as defined in Chapter 2. For low absorptions, it can be approximated as $T \approx 1 - \alpha d$. Similarly, the reflectivity for bulk materials or thin films is given by $R = 1 - \alpha d_e$. Hence the ATR spectra is said to resemble a transmission spectrum. Unlike the penetration depth [see equation (3.10)], the effective thickness for thick films depends on the polarization and is given by[81]

$$d_e^{\,s} = \frac{n_{21}\lambda_0 \cos\theta_i}{n_1\pi\left(1-n_{21}^{\,2}\right)\left(\sin^2\theta_i - n_{21}^{\,2}\right)^{1/2}} \tag{3.17}$$

and

$$d_e^{\,p} = \frac{n_{21}\lambda_0 \cos\theta_i\left(2\sin^2\theta_i - n_{21}^{\,2}\right)}{n_1\pi\left(1-n_{21}^{\,2}\right)\left[\left(1+n_{21}^{\,2}\right)\sin^2\theta_i - n_{21}^{\,2}\right]\left(\sin^2\theta_i - n_{21}^{\,2}\right)^{1/2}} \tag{3.18}$$

where $n_{21} = \frac{n_2}{n_1}$ and λ_0 is the incident wavelength in vacuum. The effective thickness is also proportional to the wavelength which leads to discrepancies in the absorption spectra where the absorption bands are stronger for shorter wavelengths (lower frequencies). The absorption spectrum becomes distorted. This complicates the comparison between ATR and transmission spectra. The above equations (3.17) and (3.18) are only valid for weakly absorbing samples and do not apply to thin films. As a result for thin films where the thickness is much less than the penetration depth ($d \ll d_p$), the ATR spectra are usually identical to transmission spectra. But for a physically thin material with unknown refractive index, it becomes even more critical to compare the two accurately. When investigating the metafilm, the refractive index is unknown so the behavior may be optically thin or thick as the optical parameters vary greatly near resonances. The modified expressions for the effective thicknesses of thin films are defined for s-polarization as [10]

$$d_e^{\,s} = \frac{4 n_{21} d \cos\theta}{\left(1 - n_{31}{}^2\right)} \tag{3.19}$$

and for p-polarization

$$d_e^{\,p} = \frac{4 n_{21} d \cos\theta \left[\left(1 + n_{32}{}^4\right)\sin^2\theta - n_{31}{}^2\right]}{\left(1 - n_{31}{}^2\right)\left[\left(1 + n_{31}{}^2\right)\sin^2\theta - n_{31}{}^2\right]} \tag{3.20}$$

where $n_{31} = \dfrac{n_3}{n_1}$ The above equations are pertinent to a three layer system with the sample (medium 2) having refractive index n_2 bounded by medium 3 (air) and medium 1 (ATR prism). For thin films, the critical angle does not depend on the index of the thin film material. It is defined by $\theta_c = \sin^{-1}\left(\dfrac{n_3}{n_1}\right)$.

3.4.2 Dispersion

The variation of the refractive index as a function of wavelength in the vicinity of strong absorbing features, i.e. anomalous dispersion, modifies the internal reflection spectra. An example that compares ATR and transmission spectra [80] is shown Figure

3-10. The differences in the calculated ATR spectra for both s and p polarizations and transmission spectra for a 10 μm thick sample are clearly seen.

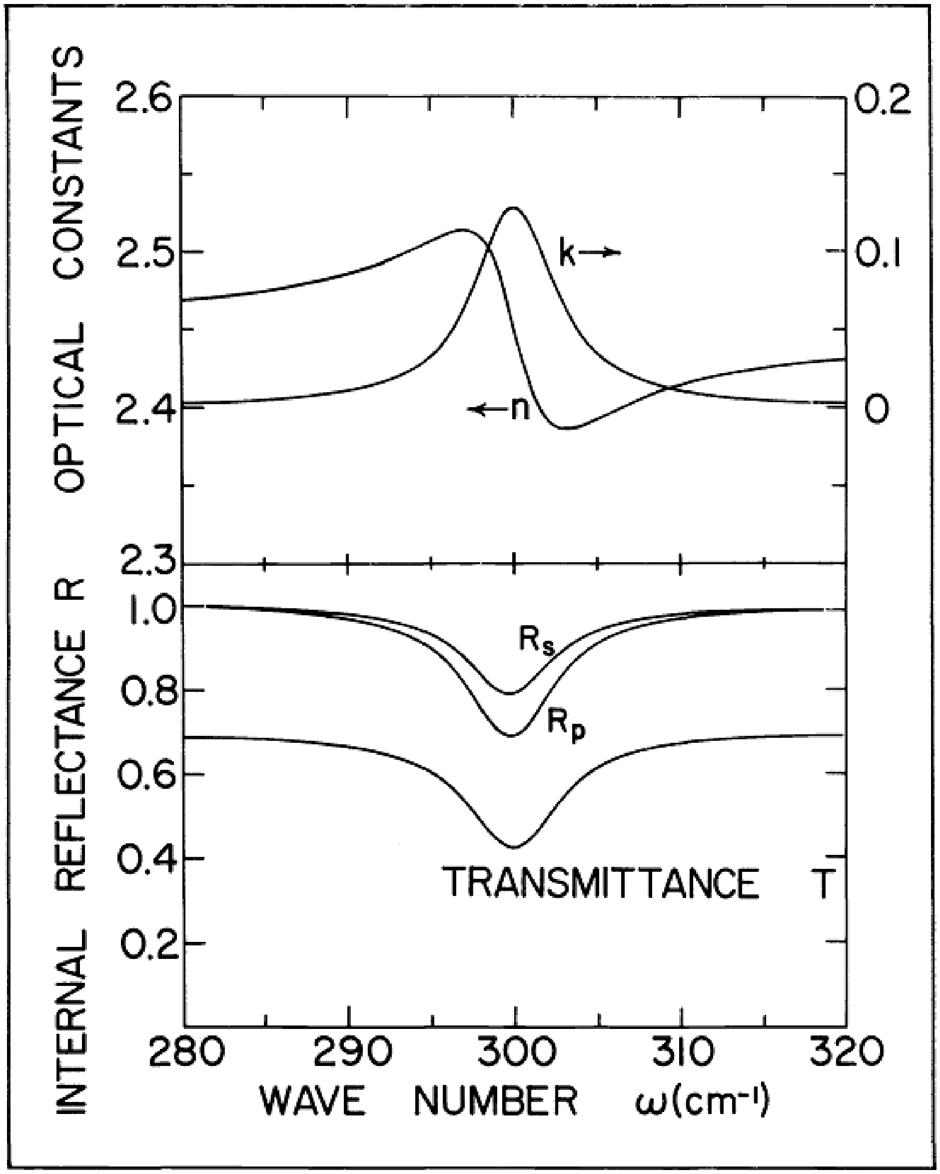

Figure 3-10 " (a) Optical constants (refractive index n and extinction coefficient); (b) Internal-reflectance spectra for s and p polarization for a sample with optical constants shown in (a). The transmittance T for a 10 μm thick sample is also shown." [80]

In the case of thick samples, the effect of dispersion is more distinct for measurements done near the critical angle. The reasons as previously stated are related to the dependence of the penetration depth on the wavelength and the refractive index of the sample and therefore anomalous dispersion distorts the ATR spectra. In order to avoid artifacts due to dispersion, it is best to conduct measurements above the critical angle. For this reason, the 45° incidence angle for the IRE in the experiments detailed in subsequent chapters is significantly larger than the critical angle of 17.01° to eliminate any impact on the measurements due to dispersion.

3.4.3 Correction algorithms

Correction algorithms are commonly required for ATR spectra in order to compensate for the dependence of the penetration depth on the wavelength to closely match the transmission spectra. Commercial software programs are able to perform routine correction algorithms on ATR spectra by scaling the spectra with the penetration depth but they are not available over a wide spectral range. There is disagreement on establishing correction methods available for THz frequencies [15, 18]. The penetration depth for the frequencies of interest (0.1 to 2 THz) lies between 10 µm to 2 mm. Since the thickness of the metafilm arrays used in this work is 0.2 µm, the evanescent field extends well beyond the metafilm sample and should not be an issue. Therefore for the samples under consideration, the ATR spectra do not warrant such a correction.

4 Metamaterials

Artificial materials such as metamaterials (MM) are designed to achieve non-conventional or display unusual properties not found in nature. This relatively new class of engineered materials exhibits a collective response equivalent to a homogenous medium that can be treated by effective medium theory with an effective permeability and permittivity. The main requirement of the metamaterial is that the constituent element dimensions and the spacing between them be much smaller than the wavelength of interest. Other examples of engineered structures include frequency selective surfaces and photonic crystals but the features for these classes of structures are on the order of a wavelength. Split-ring-resonators [21] are typical elements of MMs, chosen for the tunable self-inductance and simple geometry.

4.1 Split Ring Resonator

The split ring resonator (SRR) is an ubiquitous building block of metamaterials as shown in Figure 4-1. It is a sub-wavelength metallic ring with a gap commonly referred to as a “magnetic atom”. SRRs were proposed by Pendry for use in metamaterials in 1999[21].

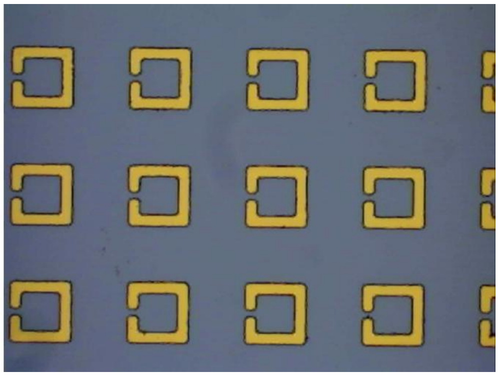

Figure 4-1 Sample array of square split ring resonators.

SRRs are intrinsically non-magnetic but when excited by an external magnetic field can show a magnetic response. An SRR can be described with an equivalent series resonant *LC* circuit model as shown in Figure 4-2, where the loop of the SRR corresponds to a single turn inductor, the gap acts as a capacitive element and the losses are represented by the resistance. According to Faraday's Law, a time varying EM field threading a loop can induce circulating currents in the loop that generates an induced magnetic dipole moment perpendicular to the plane. This current gives rise to accumulating charge at the opposite ends of the gap edges.

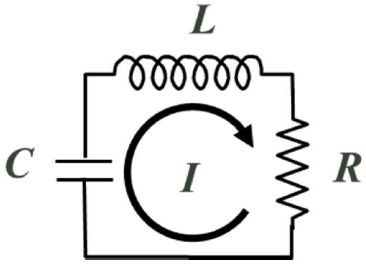

Figure 4-2 Equivalent *RLC* circuit of an SRR.

In a series *RLC* circuit, the impedance *Z* is given by

$$Z = R + X_L + X_C = R + j\left(\omega L - \frac{1}{\omega C}\right) \tag{4.1}$$

At resonance, the circuit impedance is minimal and is purely resistive when the inductive reactance X_L and capacitive reactance X_C cancel out, to give

$$\omega L = \frac{1}{\omega C} \Rightarrow \omega^2 = \frac{1}{LC} \Rightarrow \omega_0 = \frac{1}{\sqrt{LC}} \tag{4.2}$$

This resonance frequency ω_0 also known as the fundamental resonant (*LC*) frequency corresponds to the magnetic resonance frequency of the SRR. A series *RLC* circuit has the quality factor,

$$Q = \frac{\omega_0 L}{R} = \frac{1}{R}\sqrt{\frac{L}{C}} \tag{4.3}$$

The quality factor is a figure of merit that describes how well the *RLC* circuit stores energy. It is also a measure of frequency selectivity for the resonance.

The accumulation of charge at the gap provides the capacitance and the area of the loop dictates the inductance. The presence of the gap gives the structure, a larger resonant wavelength than the actual physical dimension of the loop. The effect of ohmic and radiative losses is lumped into the series resistance *R*. Energy is localized within the gap where the electric field can become 3-4 orders of magnitude higher than the incoming fields [21]. The resonance can be tuned by altering the geometry of the SRR, thickness, permittivity of substrate, shape etc. The complex effective permeability of the periodic array of SRRs under an axially aligned magnetic excitation[21] can be expressed as

$$\mu_{eff}(\omega) = 1 - \frac{F\omega^2}{\omega^2 - \omega_0^2 + i\Gamma\omega} \tag{4.4}$$

where F is the geometric filling factor and Γ represents dissipation factor due to material losses.

The magnetic resonance frequency [21] is defined by

$$\omega_0^2 = \frac{3lc_0^2}{\pi \ln \frac{2c}{d} r^3} \tag{4.5}$$

The phase between the applied magnetic field and the induced magnetic moment determines the sign and the magnitude of the effective permeability. Thus the response can be paramagnetic or diamagnetic including negative values of μ_{eff}. A single SRR element can have both electric and magnetic responses. However, the excitation of planar substrates and normal incidence geometry with purely magnetic field components at terahertz frequencies is nontrivial. The magnetic field must have a vector component normal to the plane of the array to induce a current, which can only occur if the propagation vector is not normal to the plane.

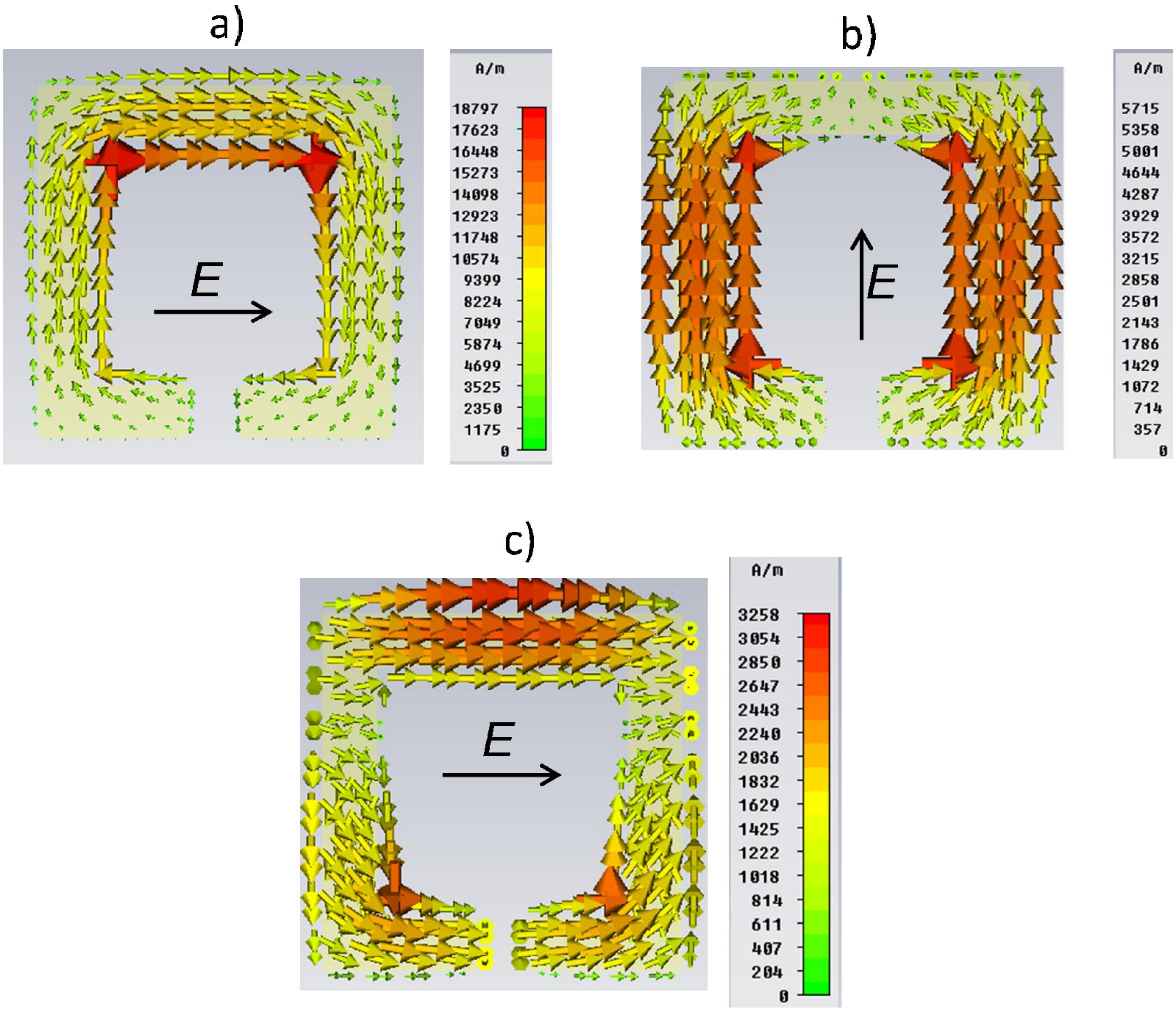

Figure 4-3 Calculated surface current densities for the fundamental *LC* resonance in part (a) and second order dipole mode in part (b) and third order dipole mode shown in (c)

The surface current densities associated with the resonances of an SRR are shown in Figure 4-3. These results are from numerical simulations using CST Microwave Studio. Figure 4-3 (a) corresponds to the circulating *LC* mode and is of primary focus for this work. Higher order dipole modes are shown in Figure 4-3(b) and (c). The fundamental *LC* mode which corresponds to the magnetic resonance frequency can be excited in two ways a) due to the external magnetic fields threading the loop which creates a circulating current and b) when the electric field component couples to the *LC* resonance even if the external magnetic field is oriented parallel to the plane of the SRR. This happens when the mirror symmetry of the SRR is broken due to the electric field component being oriented parallel to the gap bearing arm. In this case, the external magnetic field does not penetrate through the SRR. An unbalanced distribution of charge driven by the incident electric field gives rise to a net circulating current in the loop. This in turn gives rise to a magnetic dipole moment. From Figure 4-3 (a), the current is maximum on the arm opposite to the gap.

The second order dipole mode is excited when the *E*-field is perpendicular to the gap bearing arm. Figure 4-3 (b) shows oscillating currents predominantly in the non-gap bearing SRR arms. There are currents in the gap-bearing arm and the one opposite to it but they are equal and opposite of each other. This results in no net magnetic dipole.

A third order dipole mode is also seen when the SRR is rotated by 90° as shown in Figure 4-3 (c). This again happens when the mirror symmetry is broken by the *E*-field when the electric field component parallel to the gap-bearing side. But unlike the induced currents in the fundamental *LC* mode, there is no circulating current. This also results in no net magnetic dipole. This mode is observed as a higher order resonance in transmission or reflection measurements.

4.1.1 Bianisotropy in SRR

Even though SRRs provide surprising richness in observed phenomena, they pose challenges to describe analytically due to their bianisotropic nature. Asymmetry in the SRR due to the gap introduces bianisotropy in metamaterials. In bianisotropic metamaterials, the SRR exhibits magneto-electric coupling [82] where a coupling exists between the electric and magnetic responses. This implies that magnetic dipoles can be excited not only by the time varying magnetic field of the incident EM wave but also by the time varying electric field component. This applies for electric dipoles too. Accordingly, the constitutive relations are modified by including magnetoelectric coupling coefficients. Katsarakis et al.[83] have shown that the electric field can also couple to the magnetic mode when the magnetic field is oriented parallel to the plane of the SRRs, thus exhibiting magneto-electric coupling. The electric coupling to the magnetic resonance depends on the relative orientation of the SRR with respect to the electric field. Simultaneous excitation by electric and magnetic fields is also possible. The electric *LC* resonance coincides with the magnetic Lorentzian resonance frequency. The effects that result from the coupling of the incident magnetic field resulting in an electric response and vice versa, introduce non-zero off-diagonal in the magneto-optical permittivity and permeability tensors [37] [82]. For bianisotropic materials, the constitutive relations can be written as,

$$\begin{aligned} \overline{\mathrm{D}} &= \overline{\overline{\varepsilon}}.\overline{\mathrm{E}} + \overline{\overline{\xi}}.\overline{\mathrm{H}} \\ \overline{\mathrm{B}} &= \overline{\overline{\zeta}}.\overline{\mathrm{E}} + \overline{\overline{\mu}}.\overline{\mathrm{H}} \end{aligned} \tag{4.6}$$

where ε and μ and the magneto-optical permittivities, ξ and ζ are tensors of rank 2. This makes the retrieval of material parameters even more complicated. In some cases bianisotropy is unwanted, and suitable modifications to the SRR design eliminate or reduce magnetoelectric coupling such as the modified SRR (MSRR) by Marques et al [82] or the electric *LC* resonators to be described later in the chapter.

Here coupling schemes to the fundamental mode using two possible orientations of the SRR, with respect to the two incident electric field polarizations and the directions of propagation are addressed as shown in Figure 4-4.

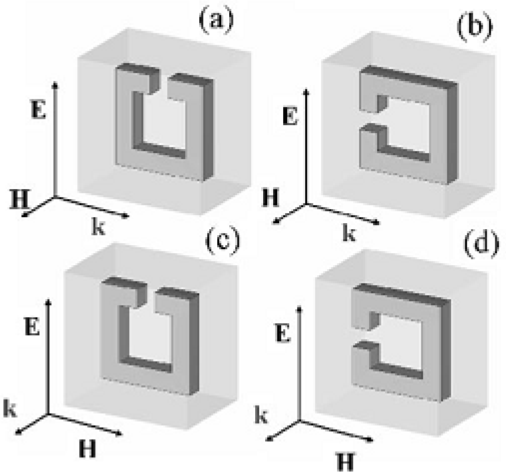

Figure 4-4 Magnetic and electric field coupling for two SRR orientations and two directions of propagation.

Case a) In this orientation [see Figure 4-4(a)], the magnetic field component penetrates the SRR loop with an in-plane propagation direction thus exciting the magnetic resonance. The coupling is only due to the magnetic field.

Case b) Magnetoelectric coupling dominates in this orientation [see Figure 4-4(b)], when the electric field is parallel to the gap bearing side and the magnetic field threads the SRR loop. When the mirror symmetry is broken by the SRR, there is an unequal charge distribution leading to a net circulating current. The resonance is potentially the strongest for this orientation since there is combined contribution of the resonant electric response with the resonant magnetic response. However this depends on the relative phase shift between the magnetic and the electric driving fields.

When the magnetic field lies completely in the SRR plane, there is no coupling to the magnetic resonance due to the magnetic field component. This holds for cases (c) and d).

Case c) There is no coupling due to the electric and magnetic fields and therefore the *LC* resonance for this orientation [see Figure 4-4(c)], is completely suppressed.

Case d) Here the expected coupling is solely due to the electric incident field just as in case b) [see Figure 4-4(d)]. This shows that the electric field can be coupled to the magnetic resonance of the SRR.

While this section addresses the basic orthogonal excitation schemes, with special attention to the polarization of the electric field component of the incident EM wave, it does not address how this manifests within a measurement. Additional cases arise if one considers the cross polarization terms generated by the *LC* resonant current. The cross-polarized terms would be equivalent to that which is detected by rotating the polarization sensitive receiver by 90° with respect to the transmitter. The specifics of the relative orientation of the detector with respect to the incident applied electric field and the symmetry of the SRR will be addressed in a later chapter. Electric, magnetic, both or none excitation schemes can be determined from these parameters.

4.1.2 Topological variations

While the focus of the preceding chapter has been on simple SRRs, the concepts can be applied to a range of different geometries to achieve metamaterial elements.

Variations in topologies for the planar SRR structures at terahertz frequencies are shown in Figure 4-5.

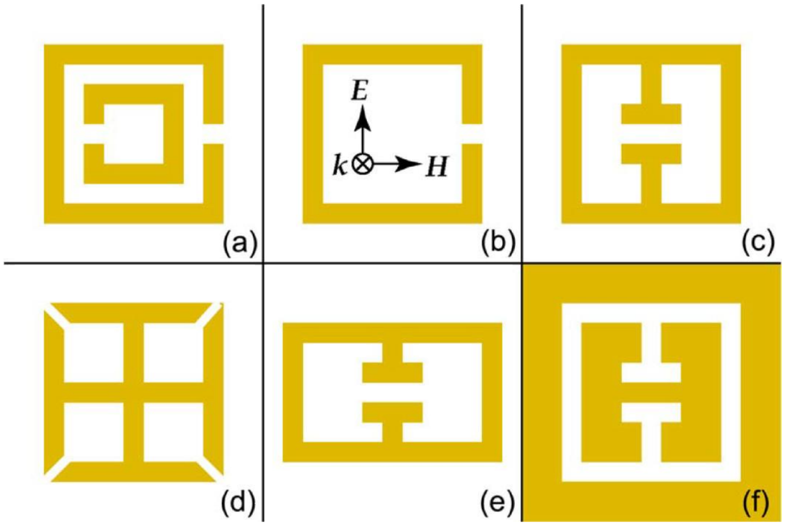

Figure 4-5 Planar SRR topologies from [84]. "a) single gap double resonator (b) single gap single loop, (c) electric *LC* resonators or eSRR, (d) four-fold rotational-symmetry eSRR, (e) rectangular eSRR and (f) complementary eSRR".

For the double SRR shown in Figure 4-5 (a), the resonance frequency is governed by the mutual inductance between the two rings and also by the self-inductance of the individual rings. The inner ring generates a large capacitance and lowers the resonance frequency. Typically this results in dual resonances that are frequency shifted from their isolated *LC* resonances.

SRRs have been most commonly utilized for their magnetic response, as discussed previously. But they can also be used as electrically resonant elements that exhibit no net magnetic dipole at the *LC* resonance. These special types of SRRs have geometries that are designed to suppress the net magnetic field from the *LC* resonance and thus strictly exhibit an electric response [85] while minimizing any coupling to an external magnetic field. They are known as electric *LC* resonators (ELC) or electric SRR (eSRR). Examples of such electric *LC* resonators are shown in Figure 4-5 parts (c) - (f). Under the effect of an external electric field, currents in the two loops are equal and opposite due to the structural symmetry, [see Figure 4-5 (c)] and therefore cancel each other. Hence there is no magneto-electric coupling between adjoining elements.

Others such as Figure 4-5 (d) do not show any sensitivity to polarization of the incident field (exciting field) due to the four-fold symmetry [86].

A purely electric response can also be obtained by the application of Babinet's principle to the standard eSRR unit cell leading to corresponding inverse structures called as complementary eSRRs [87] like Figure 4-5 (f). The band-stop (dips) transmission response seen in ordinary SRRs appear as band-pass (peaks) transmission in the case of complementary metamaterials.

SRRs are not the only subwavelength resonating element, nor are they confined to THz radiation. Over the years, these sub-wavelength resonating elements have evolved from swiss rolls, thin wires[88] , magnetic rods, to simple split ring resonators and fishnet structures to name a few [84]. The lattice of straight wires and its variants are chiefly used for electric response ($\varepsilon < 0$) whereas the loop wire and its variations are explored for their magnetic properties. Fishnet metamaterials [35]are popular in the visible region. These structures consist of a meshwork of stacked metallic layers separated by a dielectric spacer layer.

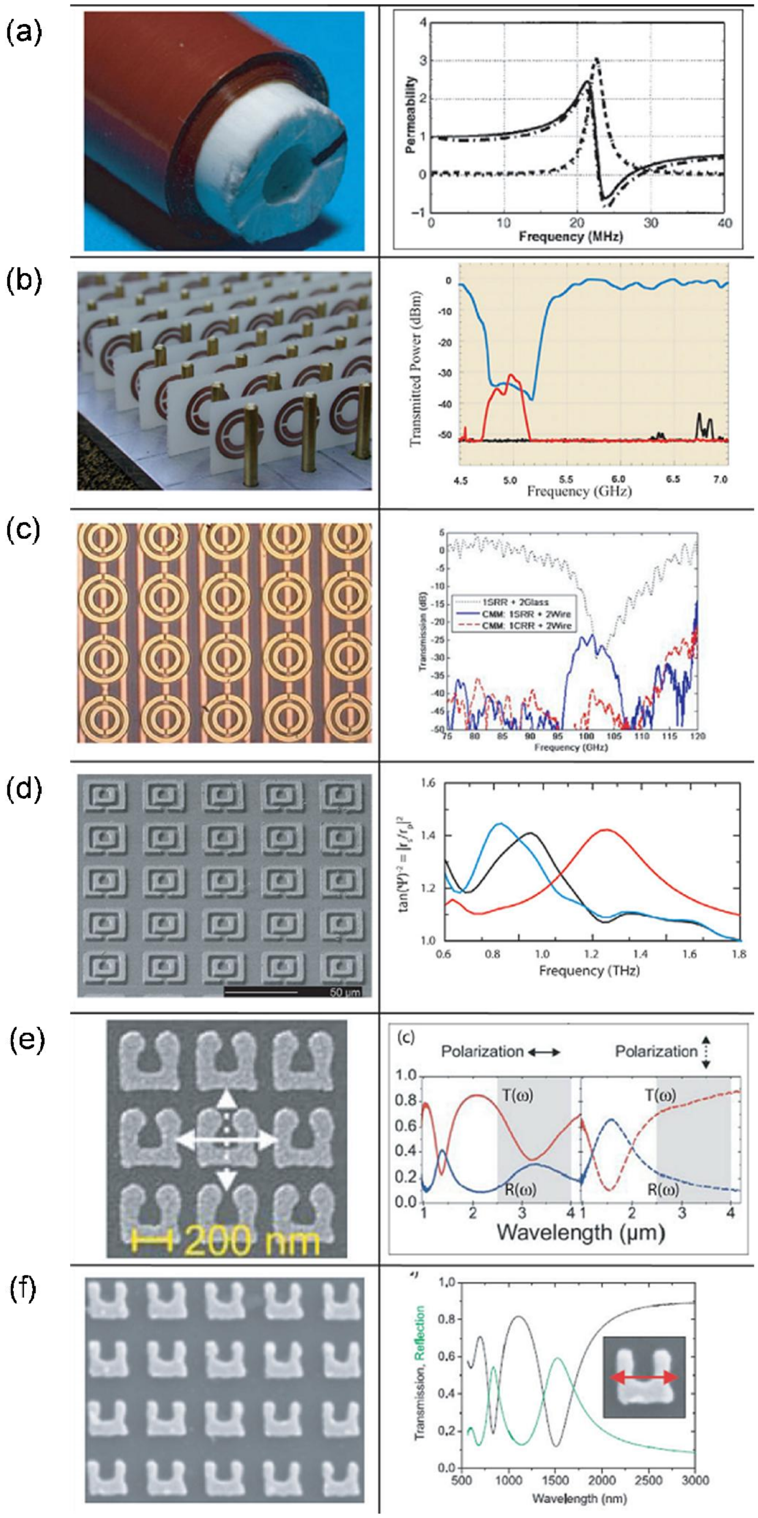

Figure 4-6 Metamaterial variations [89]

The swiss roll metamaterial from [21] [89] shown in Figure 4-6 (b) is a three-dimensional (3D) magnetic metamaterial. It is composed of two-dimensional (2D) conducting sheets rolled into a cylinder and is designed to resonate at RF frequencies [21]. A preliminary experiment at microwave frequencies by Smith et al. in 2000[23] confirmed Veselago's prediction of left-handedness by making use of a combination of ring and wire conducting elements. Such a left-handed structure is shown in Figure 4-6(b) and consists of two concentric metallic rings interrupted with opposite gaps and plasmonic wires deposited on opposite sides of a dielectric substrate arranged into a periodic medium. Figure 4-6 also shows some of the developments extending to other frequency ranges such as mm-wave [part (c)], THz (Figure 4-6 d)), mid-IR (Figure 4-6 (e)) and Near-IR (Figure 4-6 (f)). Metamaterials especially benefit terahertz frequencies where the magnetic response of naturally occurring materials is relatively weak [30] and may provide the capability to engineer novel optics[90].

4.1.3 Metafilm arrays

This research is focused on single-gap single ring split ring resonators (SRR) as the primary elements of the metamaterial array in conjunction with ATR spectroscopy. The metamaterial samples are planar, periodic arrays of split ring resonators on high resistivity silicon or GaAs substrates.

The single gap SRRs are fabricated on a double side polished substrate using standard photolithography and an e-beam evaporation of 200 nm of gold following 10 nm of titanium for adhesion. The two substrates used in this study were: 500 micron thick semi-insulating GaAs and 975 microns thick high resistivity silicon.

The initial sample was fabricated on GaAs substrate. The SRR unit cell was 83 to 103 µm with an outer dimension of 48 µm, 6 µm capacitive gaps, and 5 µm line widths. The fundamental *LC* resonance lies at 0.38 THz. The size of the array was 10 mm x 10 mm which provide sufficient area for transmission TDS measurements.

The larger SRR arrays that were custom designed to eliminate experimental artifacts (to be described in Chapter 6 and uncertainties in the interpretation of results have a 30 mm x 30 mm clear aperture, which is large enough for a focused THz beam in the ATR configuration. The outer dimension of the SRR is 40 µm, 30 µm and 25 µm for MM1, MM2, and MM3 respectively. MM1 is shown in Figure 4-7. All three SRR geometries have a fixed 80 µm unit cell. Each SRR has a capacitive gap 6 µm wide.

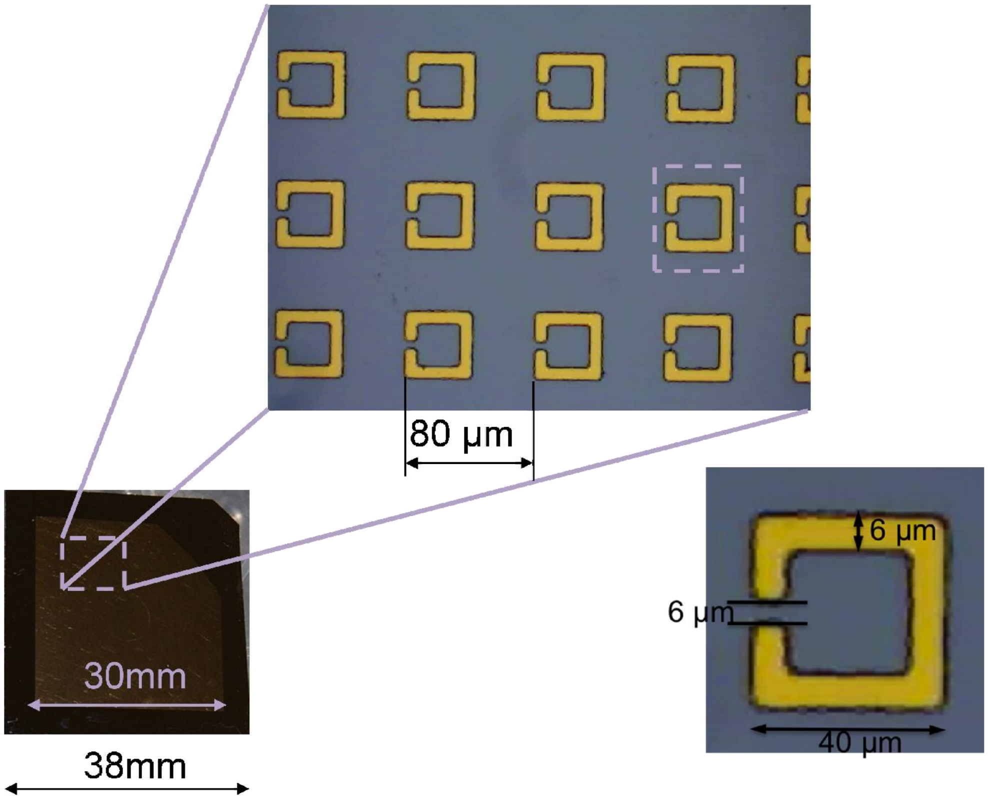

Figure 4-7 SRR array on Silicon substrate (sample MM1)

The analytic procedure for retrieval of effective medium parameters is non-trivial. Therefore numerical simulations are the common starting ground for the design of metamaterials in order to engineer the geometry and understand the resonant properties due to the interaction with EM waves. The metafilm arrays were designed to have resonances in the terahertz range. A commercially available finite element solver (CST microwave studio 2010) was used to determine the physical parameters of the SRR arrays. Simulations were performed at normal incidence. The fundamental resonances of the three samples were chosen to be 0.44THz, 0.65 THz and 0.85 THz. The initial intent was to consider a variety of *LC* resonances determined primarily by the self-inductance of the individual SRRs while holding other parameters fixed. Table 2 lists the details of the samples used in this work.

Sample	SRR size (μm)	Simulated LC mode (THz)
MM1	40	0.44
MM2	30	0.65
MM3	25	0.85

Table 2 Sample size and *LC* resonance

The frequency dependent amplitude transmission and reflection from the simulations are plotted in Figure 4-8 for the samples MM1, MM2 and MM3. The transmission coefficient is equivalent to the S21 scattering parameter and reflection coefficient corresponds to the S11 scattering parameter.

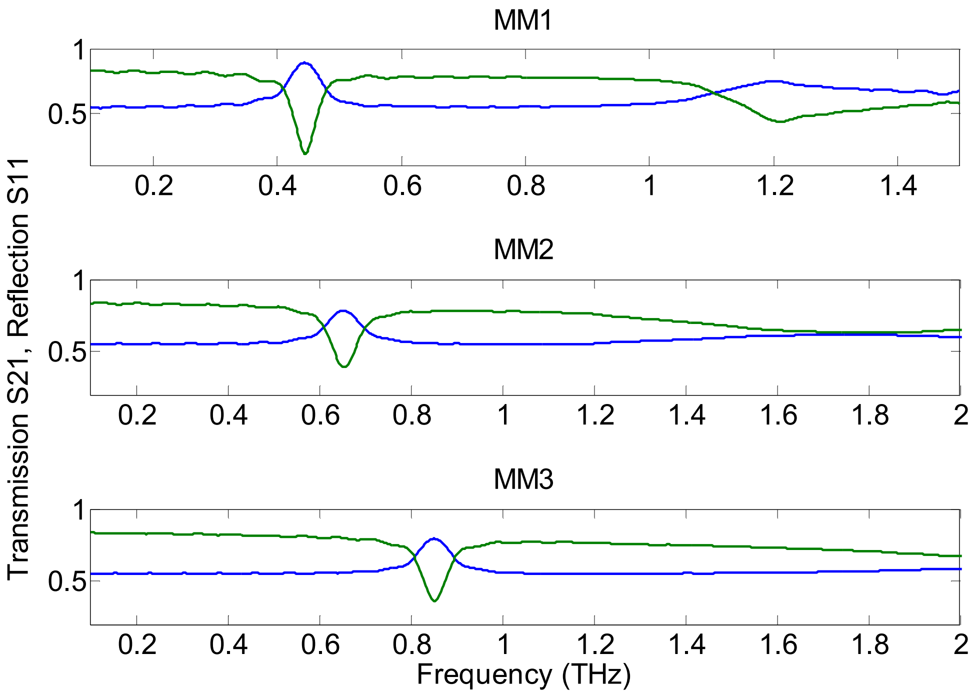

Figure 4-8 Simulated transmission (green) and reflection (blue) spectra for samples MM1, MM2 and MM3.

The dipole resonance for MM1 is located at 1.2 THz. This higher order resonance corresponds to the second order dipole mode as shown in Figure 4-3 b). The trailing edge for the dipole resonance can be seen in MM2 but is out of the range of simulations for the metafilm MM3. Characterization of the resonance modes is commonly performed by directly measuring the relative decrease in the broad transmission spectrum between a MM sample and reference. This follows the standard procedure outlined in Chapter 2 and is one reason for the wide ranging experiments and theory focused in this spectral region.

5 THz-ATR Experimental setup

This chapter discusses the experimental techniques used for implementing THz-ATR. The MM-ATR response is measured using a fiber coupled photoconductive antenna based terahertz ranging system which is capable of performing THz time domain spectroscopy in both transmission (Figure 5-1) and reflection modes at any angle within mechanical limits. This differs from the THz-TDS system in Chapter 2 by replacing reflective optics with refractive optics and changing from 4*f* to 8*f* geometry that will be described later. Figure 5-2 shows the experimental layout of a fiber coupled THz ranging system further modified for THz-ATR measurements. The ranging system was modified in order to accommodate the introduction of a silicon prism and sample by changing the spacing between the transmitter and the receiver arms.

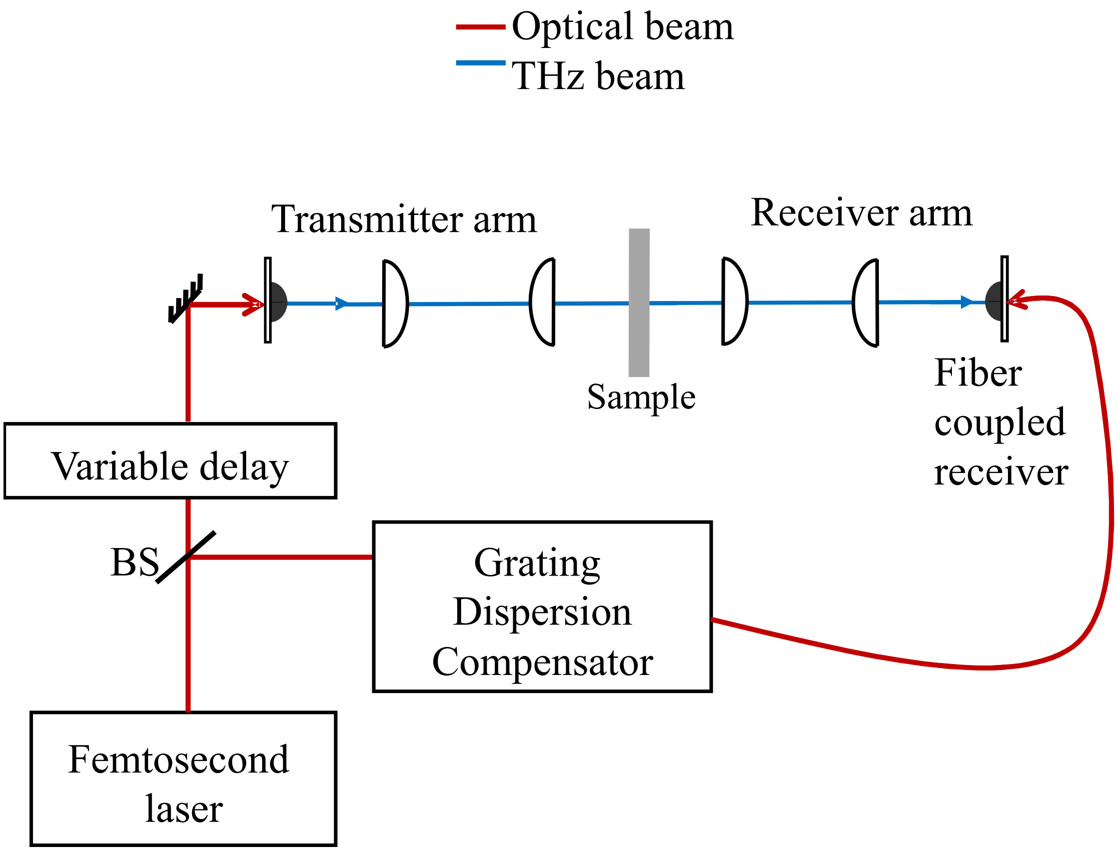

Figure 5-1 Fiber coupled THz TDS arrangement for direct transmission measurements $\theta = 0°$.

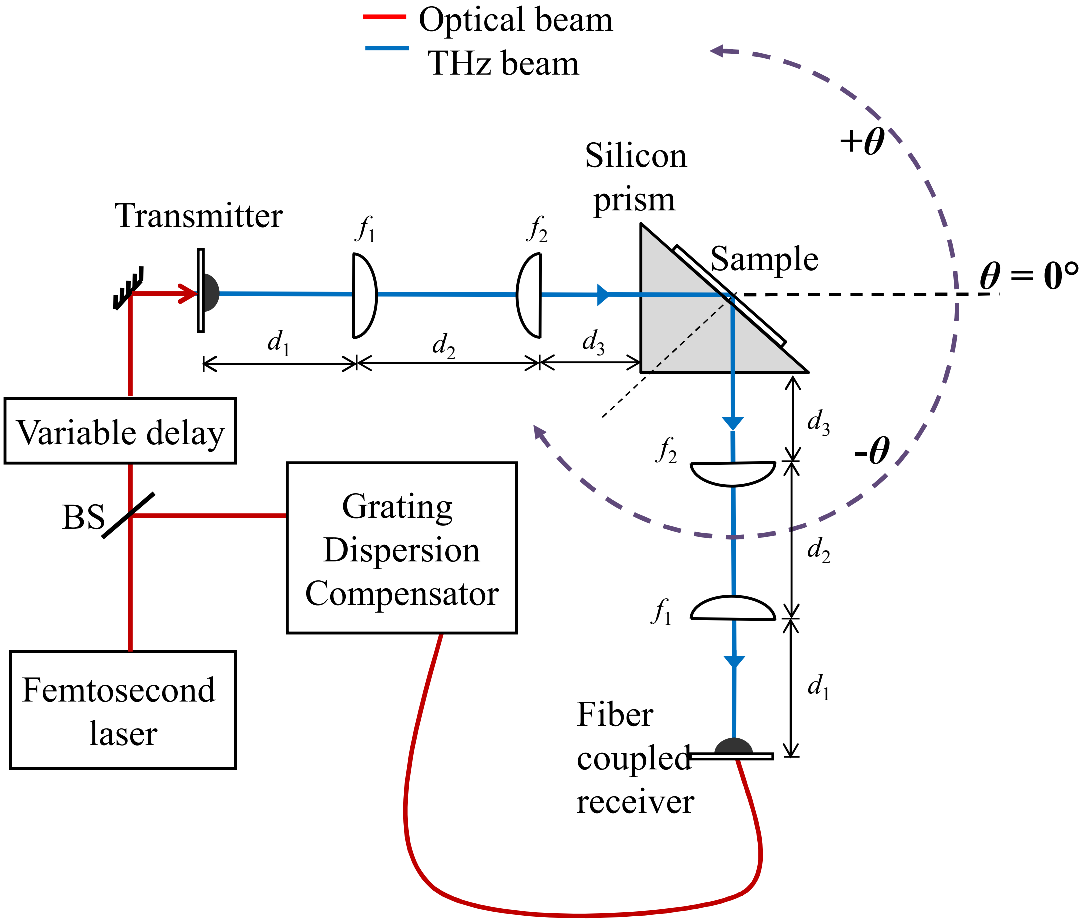

Figure 5-2 Fiber coupled THz TDS arrangement for THz ATR measurements. Here $\theta = -90°$. Angle defines the position of the receiver arm with respect to the direct transmission measurements.

The THz time domain ranging spectrometer is a modification of the standard THz-TDS system described in Chapter 2. It consists of a grating dispersion compensator, a terahertz transmitter, fiber-coupled receiver and beam shaping optics.

The ranging system uses a passively mode-locked titanium-doped aluminium oxide (Ti:sapphire) laser (Griffin, manufactured by KML, Inc.) that is pumped by a 4.5 W at 532 nm frequency doubled diode pump solid state laser (Finesse by laser Quantum). The Ti:sapphire oscillator produces 500 mW of femtosecond optical pulses centered at

800nm at a repetition rate of 87 MHz and approximately 31 fs in duration [91] when in peak operating condition. The spectral bandwidth has a FWHM of 20 nm. The laser oscillator is air cooled, which minimizes maintenance by removing the water cooling system, but increases laser sensitivity to ambient laboratory temperatures. The drawback of having such an air cooled laser is a longer warm up period for stable operation.

The optical beam is split into two beams after passing through a 30-70 beamsplitter (BS) with the low power beam directed to the transmitter and the higher power beam for the receiver. The relatively low powered optical beam passes through a variable delay line and is steered into the terahertz transmitter. The available time delay is around 800 ps (2x12 cm). The resolution of the time domain measurements is approximately 33 fs which corresponds to a 5 μm step on the delay line.

The GaAs THz transmitter operates at a typical optical power of 10 mW. When excited by the laser pulse, a transient photocurrent generates a near single cycle pulse of THz radiation. The optical beam is linearly polarized perpendicular to the transmitter striplines. The second high powered optical beam undergoes dispersion compensation through a grating pair assembly arranged in Littrow configuration. Due to losses incurred at the compression optics in the grating cell, the input of ~100 mW is reduced to 17 mW of optical power. This pre-compensated optical beam is directed onto a three dimensional flexure stage with differential micrometers. The flexure stage has a 10 mm f.l. focusing lens to ensure that the light fills the fiber core. This is then launched into a 2 m long polarization maintaining fiber. Around 6 mW of optical power is available at the output of the fiber going into the detector. The realizable coupling efficiency is around

35%. A collimating lens with a focal length of 10 mm is connected at the fiber end. The receiver is fiber coupled to maintain absolute timing and relative focus on the receiver antenna. Timing is controlled through a mechanical delay line that consists of a retro-reflector on a stepper motor driven translation stage

Both the transmitter and receiver chips are housed in a module referred to as a Field Replaceable unit (FRU) [92] shown in Figure 5-3.

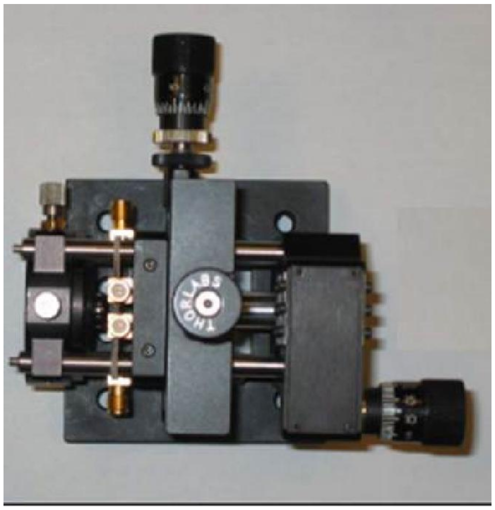

Figure 5-3 Field Replaceable Unit (FRU) module for THz transmitter and receiver, from [92]

A FRU consists of translation stages with differential micrometers that help steer the optical beam on the source and detector chips. The silicon lens attached to the back of the chip can be moved in the x and y directions. The chip can also be moved along the x and y axes. Additionally, the position of the optical lens can be varied to focus the laser beam onto the chip.

The transmitter antenna structure is essentially a pair of coplanar transmission lines, 10 μm wide, photo-lithographically deposited on a semi-insulating GaAs substrate and is biased at 55 V_{DC}. The transmission lines are separated by a gap of 80 μm on this transmitter chip.

The receiver antenna structure (10-30-10) is a photo-conductively switched dipole pair (Grischowsky-dipole [66]) photo-lithographically fabricated on ErAs nano-islands embedded in GaAs substrate. These special receiver substrates have demonstrated an enhanced response with low input optical powers [91]. The strong response with low optical gating power is important due to the reduced power available out of the single mode fiber. The receiver is mounted on a rotation arm capable of measuring a continuous range of angles between the emitter and the detector [93].

The terahertz antenna chips on the surface of the substrate are backed by hyper-hemispherical silicon lenses. These lenses act as collimating lenses since the height of the lens corresponds to the focal length less substrate thickness. Thus the antenna on the surface of the substrate is at the focal point for the lens.

Since it is not possible to view the antenna pattern on the fiber coupled receiver using standard back-reflection techniques, this type of receiver is aligned by mounting it in a standard THz TDS setup for transmission measurements (as shown in Chapter 2). The back-reflection of the antenna is then imaged on a card with a hole punched to let the laser beam through the hole. The laser spot is initially defocused using the z knob in the FRU and thereafter gradually focused by observing the rise in the THz signal and using the x and y micrometers to steer the antenna onto the optical focal spot.

Some initial work was done using a photonic crystal fiber in order to replace the dispersion compensation and reduce the demands on the limited optical power from the oscillator, but the difficulties in characterizing the beam out and matching timing (as well as the user facility requirement) prevented full implementation of the upgrade. The THz ranging system was preserved in its original state with the single mode fiber and lossy dispersion compensator. The polarization maintaining fiber was checked for damaged by visually inspecting the fiber through a fiberscope. The fiber required periodic polishing when there was no gain in the THz signal through traditional optimizing methods and the far-field mode from the fiber was distorted due to surface imperfections.

The receiver and a pair of lenses for shaping the THz beam are mounted as a unit on optical rails. The rotation assembly physically limits the available angles to a range of +70° and −140° with 0° being the reference for direct transmission measurements (see Figure 5-1). Due to the restraints introduced by the opto-mechanical components; the allowable range of rotation for the terahertz ranging system is 250° from the transmitter.

Two pairs of plano-convex Picarin lenses [94] (1.5” diameter) are used to collimate and shape the terahertz beam. The Picarin lenses are initially arranged in a linear $8f$ confocal geometry (f_1 = 100 mm, f_2 = 50 mm, f_2 = 50 mm, f_1=100 mm) from the system shown in Figure 5-1 and mounted in a cage assembly using cage rods and cage posts (Figure 5-4) to enable ease of movement.

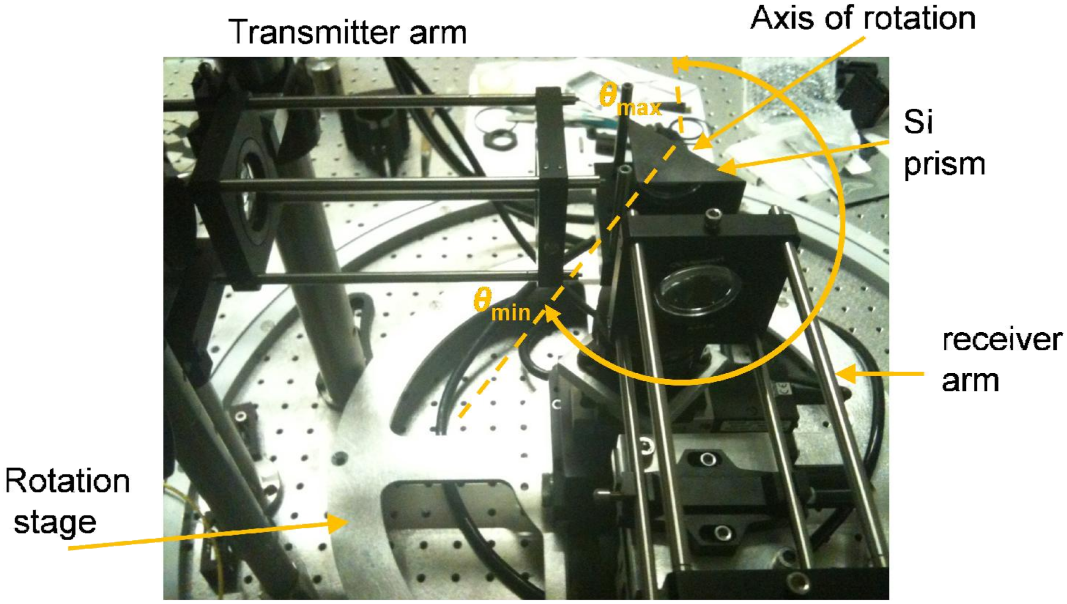

Figure 5-4 Transmitter and receiver arms cage system plus prism.

The lenses are separated by distances indicated in Figure 5-2 where $d_1 = f_1 = 100$ mm, $d_2 = f_1 + f_2 = 150$ mm. The distance between the inner lenses with focal lengths f_2 and the front face of the prism is set to $d_3 = 36$ mm. The lens pair with focal lengths f_1 and f_2 can also move together as a unit when reconfiguration is required without introducing major perturbations to the system. The system was considerably improved by introducing the cage system thus eliminating a mechanically unstable mount. The original opto-mechanical support was not reconfigurable. The improved cage assembly made it modular which is important especially when introducing the high index prism at the focus. Due to the requirements that the ranging system be part of a user facility, the lens holders for the cage system were modified in order to make reflection measurements at near normal incidence. This necessitated significant time and effort in careful design to meet such requirements while maintaining the robustness and modularity of the system.

With the modifications to the design of the lens holders, the minimum angle between the transmitter and receiver was 43°. These changes increased the terahertz system's flexibility to handle thicker samples and maximized the optical transfer function, a capability that was non-existent at the beginning of this research.

This confocal symmetry is modified to allow insertion of a large high index prism at the frequency independent beam waist. The prism material is high resistivity silicon which exhibits very low index dispersion and an absorption coefficient less than 0.05 cm^{-1} across the accessible frequency range [66]. A custom cradle holder was designed to seat the 45°- 45°- 90° silicon prism (see Figure 5-5). This prism mount was fashioned from Delrin at the Los Alamos National Laboratory (LANL) machine shop. It kept the TIR interface of the prism placed along the axis of rotation for the motorized stage supporting it. It also made the TIR face of the prism accessible for sample mounting. Small posts initially served as a mechanical means of securing the sample. Later on these posts were used as hard points to secure rubber bands.

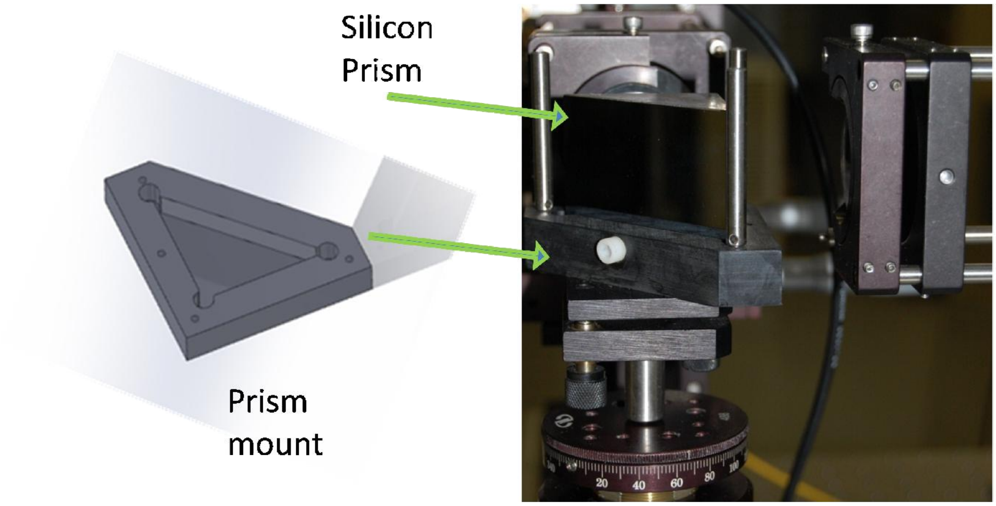

Figure 5-5 Custom Prism mounting assembly.

Stacked translation and rotational stages provided multiple degrees of freedom. The sample mount is able to move using the rotational arm of the ranging system, a rotation mount attached to the base of the mount and additional linear translation stages. The rotation stages are mounted such that the axis of rotation was common to all the stages. The axis of rotation is maintained at the prism's TIR face for all the stages. A motorized linear stage and a manual micrometer allow linear displacement along two orthogonal linear axes. The height and the tilt of the prism are also adjustable using suitable opto-mechanical components. Alignment procedures were followed to maintain a common axis. These procedures will be discussed in a later section.

With no sample, the incident s-polarized pulse enters the silicon prism at normal incidence on the entrance face and undergoes total reflection at the TIR surface, with a 45° angle of incidence which is well beyond the critical angle ($\theta_c = 17.1°$) for the silicon-air interface. This prevents any k-vector filtering due to variations in the phase front curvature of the short pulses which can yield anomalous results near critical angle [22]. The reflected signal is measured when the receiver arm is oriented at $\theta = -90°$ with respect to the transmitter, as indicated (Figure 5-2). When the angle between the transmitter line and receiver is 0°, the system is in the direct transmission configuration (Figure 5-1).

5.1 Terahertz beam propagation

In order to achieve optimum coupling between the THz transmitter and the receiver, it is necessary to understand THz beam free–space propagation from the point of generation to the point of detection. Figure 5-6 to Figure 5-8 show the THz beam propagation through the system. The terahertz beam follows the ABCD formalism from Gaussian optics since the field pattern resembles a $TEM_{0,0}$ Gaussian, although it is more complex [77]. Figure 5-6 shows the terahertz beam radius as a function of distance while propagating through the spectrometer before prism insertion [case a)]. This figure shows the beam radius as a function of position along the optical axis. The calculated frequency independent beam waist at the sample plane is 1 mm assuming a starting beam waist of 2 mm. The calculation was performed for different frequencies from 0.1 to 2 THz with a frequency step of 0.2 THz. The calculation assumes paraxial rays in free space and treats the optics as thin lenses and assumes that they are perfectly aligned. Although this treatment is far from ideal, it does give a physical understanding of the beam propagation through such a complex system. The introduction of a large volume of the higher index Si material dramatically impacts the beam characteristics.

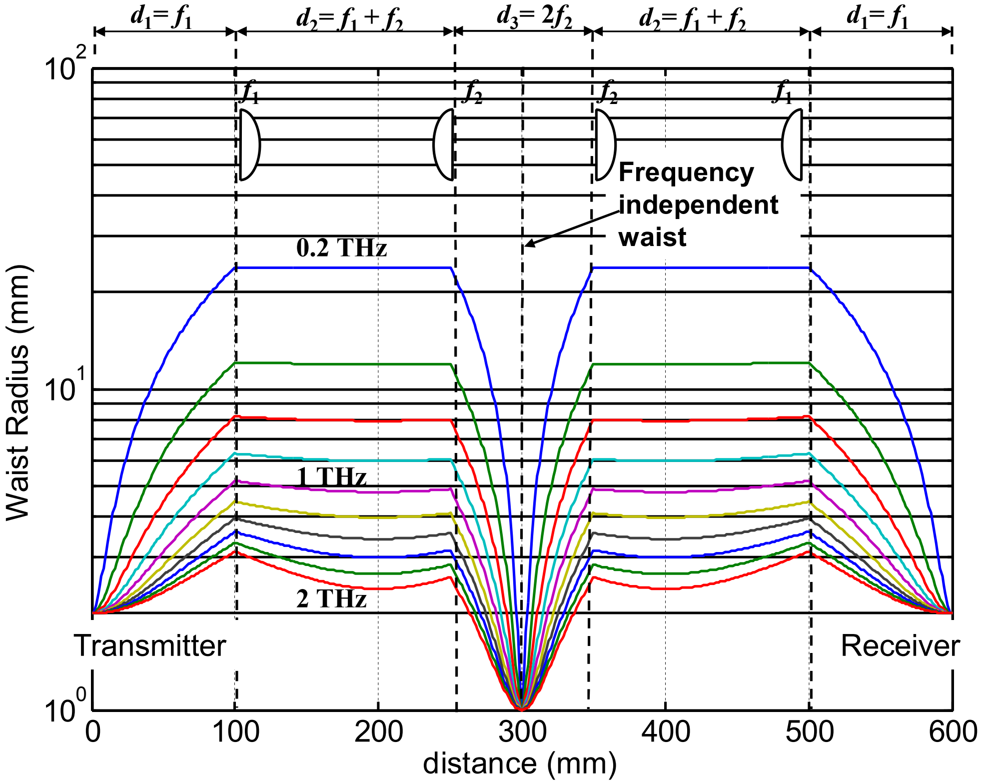

Figure 5-6 Case a) Beam radius as a function of distance propagating through an 8*f* confocal THz-TDS system.

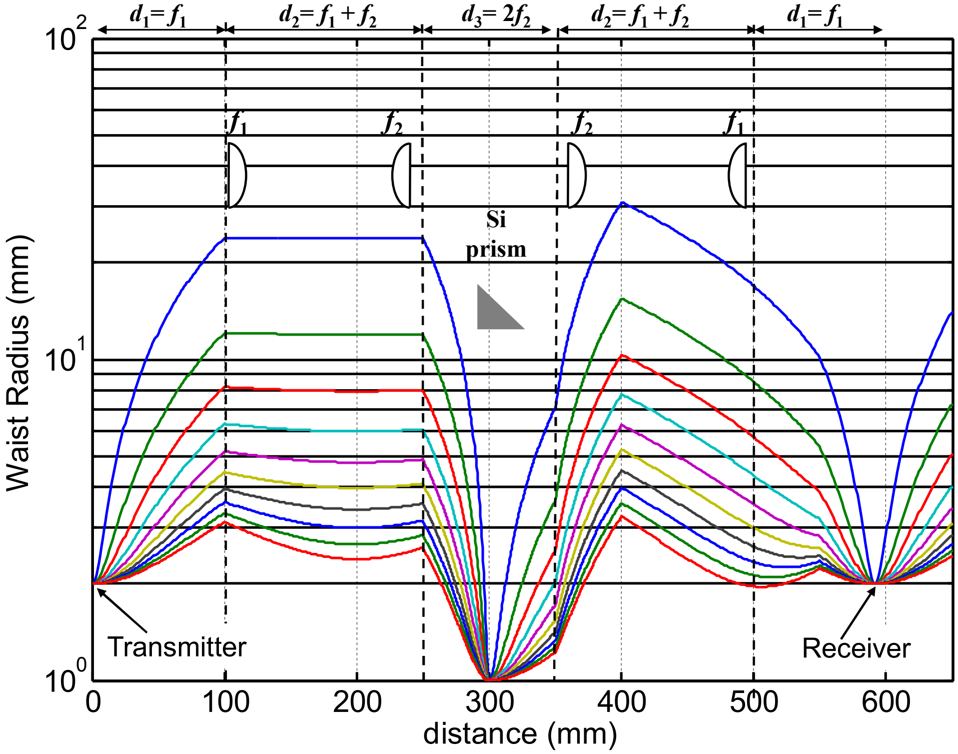

Figure 5-7 Case b) Beam propagation after inserting 50 mm thick Si prism maintaining 8*f*-confocal distances from Figure 5-6.

Introducing the prism bends the beam path by 90° at the TIR face and the receiver arm is rotated to $\theta = -90°$. After insertion of the 50 mm thick prism with input face located at 300 mm, with the aforementioned confocal distances, the coupling becomes distorted [see Figure 5-7 case (b)]. The high index of the Si prism modifies the optical component spacing from the direct transmission configuration. The overlap between the beam profiles in the transmitter and the receiver arms is therefore non-optimal. The low frequencies suffer the most due to finite aperture size of the lenses thus lowering the coupling efficiency. Hence the spacing between the short focal length lenses (f_2 = 50 mm) was adjusted to accommodate the additional 50 mm of silicon. It was found that the distance between the short focal length lens in the transmitter arm and the prism had a large effect in making the beam propagation symmetrical. By keeping all other distances constant, this parameter was adjusted to achieve the result shown in Figure 5-8 case (c). The criterion for this decision was the placement of the frequency independent beam waist at the TIR interface on the prism. This location corresponds to the location of the sample. As a result, the distance between the two lenses is greater than the original configuration and the resulting length of the system is increased with the constraint that the system could be returned to the original configuration with a minimum of effort to support the shared nature of the facility. The beam propagation is shown in Figure 5-8 (c).

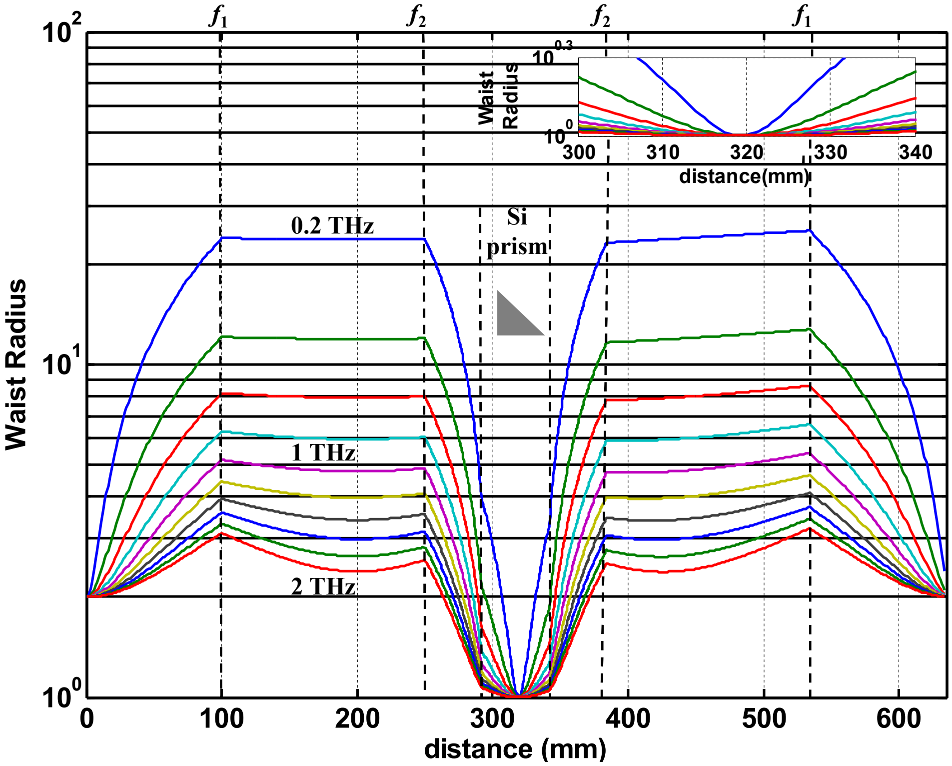

Figure 5-8 Case c) Beam propagation after inserting 50 mm of silicon and adjusted spacings. The focus shown as an inset is located at the TIR (oblique) face of the prism.

The calculated frequency independent beam waist at the prism is unchanged. Thus the symmetry becomes non-confocal due to insertion of a high index material at the focal plane. The beam phase front is not perfectly flat, but located within the Rayleigh range for the frequencies of interest; the angular spread for propagation of the Gaussian beam is minimized.

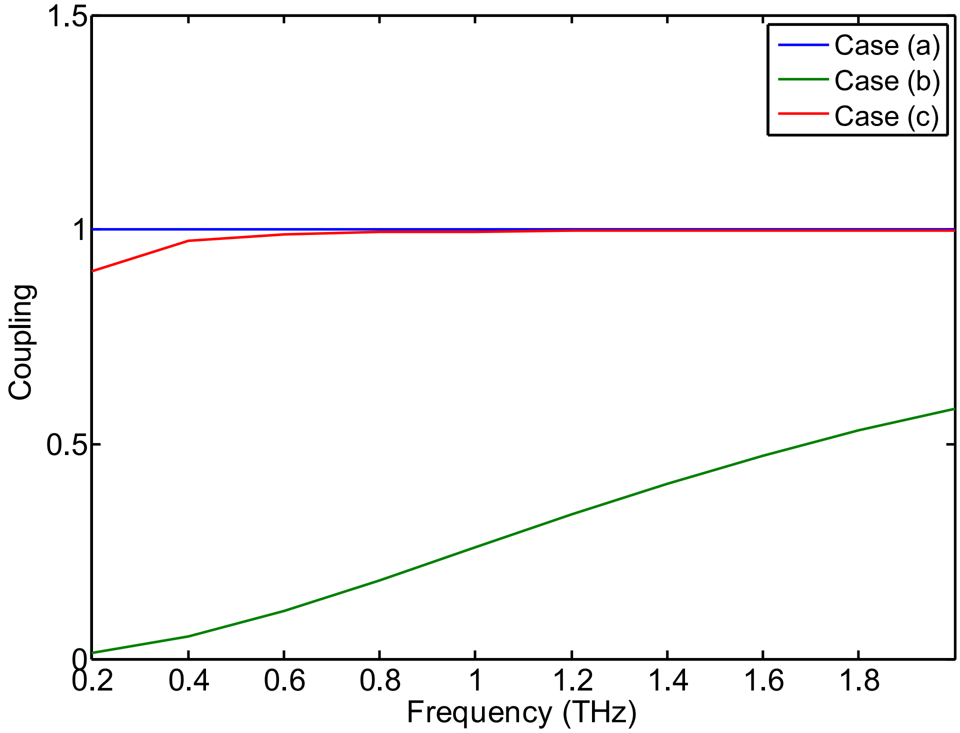

Figure 5-9 Coupling efficiency for the cases (a) shown in Figure 5-6, (b) shown in Figure 5-7 and (c) shown in Figure 5-8.

The coupling after adjusting the distances is vastly improved as seen in Figure 5-9. The coupling efficiency plotted in Figure 5-9 is expressed as

$$C(\omega)=\frac{4}{\left(\frac{w_s(\omega)}{w_d(\omega)}+\frac{w_d(\omega)}{w_s(\omega)}\right)^2+\left(\frac{kw_s w_d}{2}\right)^2\left(\frac{1}{R_d(\omega)}-\frac{1}{R_s(\omega)}\right)^2} \tag{5.1}$$

“Where w_s is the amplitude profile 1/e radius at some point in the system of a specific mode from the source, w_d is the radius of the beam from the THz detector at the same point, R_s and R_d are the radii of curvatures with c the speed of light in free space and $k = \frac{2\pi}{\lambda}$." [53] Case (a) is the perfect optical transfer function for a symmetric 8*f* configuration. Case (b) is after the introduction of the slab of Si without modifying the placement of the optics. For case (b), the low frequency components are strongly attenuated. Case (c) is with the modification of the optics.

5.2 Terahertz beam characterization

A priori knowledge of the terahertz beam width at the reflecting surface of the prism is critical to useful measurements. The THz beam width was estimated using several methods to check for consistency.

The first method was a Gaussian beam calculation. It starts with an estimated ~2 mm starting beam waist at the terahertz transmitter which is focused by a factor of $f_1/f_2 = 2$ resulting in a waist radius of 1 mm or beam waist diameter of 2 mm at the sample focal plane (TIR face of the prism). This calculation (see Figure 5-8) assumes a paraxial Gaussian beam with a fundamental mode and ignores aperture effects due to lenses.

The second method was a measurement where the terahertz beam was characterized by lateral translation of the detector assembly. The sensitivity of the system with lateral off-set of the receiver in confocal geometry was measured over a range of ± 7 mm orthogonal to the optical axis. The experimental configuration for this measurement is shown in Figure 5-10.

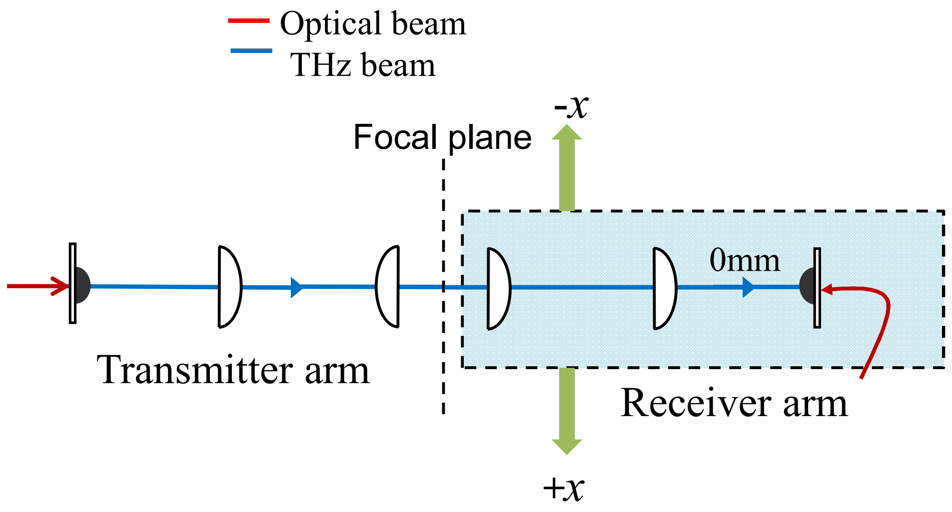

Figure 5-10 Transmission configuration used for characterizing the THz beam profile.

The opto-mechanical components that house the lenses and the terahertz receiver are mounted on a micrometer-adjustable base and rail assembly allowing controlled movement both along the optical axis and perpendicular to the optical axis. The highlighted box indicates the lateral movement of the receiver arm as one unit in the plane of the table normal to the optical axis of the THz beam. Optical axis corresponds to peak measured signal which is defined to be $x = 0$ mm. The measured beam profile is plotted for two frequencies of interest in Figure 5-11 as a function of the lateral movement ± x mm.

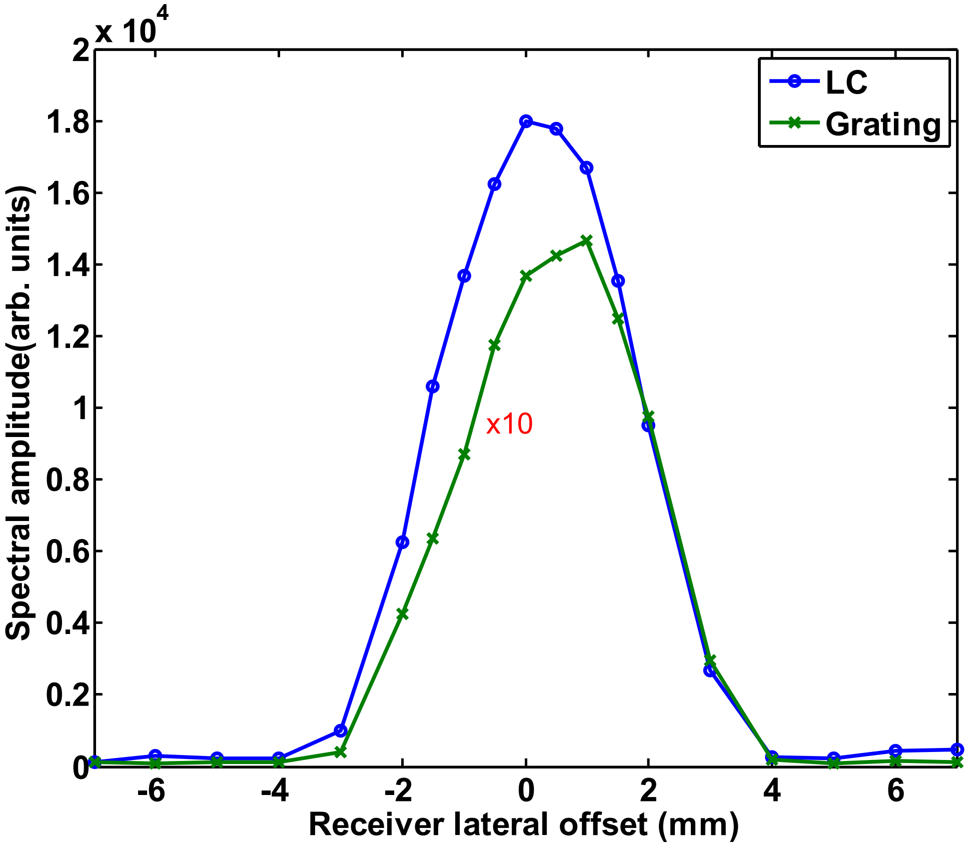

Figure 5-11 Measured beam profile in the confocal configuration as shown in Figure 5-10. The amplitude of the grating frequency profile is x10 for comparison of the beam widths.

The *LC* curve in blue in Figure 5-11 indicates the integrated spectral magnitude for the frequency range of 0.41 THz to 0.46 THz for different lateral off-sets. The green curve indicated as "grating" in Figure 5-11 is the integrated spectral magnitude for the frequency range of 1.51 to 1.56 THz, which corresponds to the grating resonance that was observed in preliminary measurements. The average was taken in order to eliminate minor variations near the fundamental resonance mode of 0.44 THz and near the grating resonance of 1.5 THz. This measurement is a result of the convolution of the optical transfer functions of the transmitter with that of the receiver. The grating response is fixed in size and indicates the center and size of the incident beam as it is a frequency independent beam waist. The actual beam width can be determined by comparing the above measurement with the convolution of two identical Gaussian beam profiles. This is a justified assumption because the transmitter and receiver arm optics are symmetrical. The de-convolution of the beam profile resulted in a beam width of 3.2 mm. (4.5 mm at 45°). The results of the beam diameters obtained for both *LC* and grating frequency responses agree with each other although there is a slight shift of 250 μm between the peaks and a minor asymmetry in the beam profile for the grating resonance.

5.3 Experimental challenges and Tips & Techniques

5.3.1 Axis of rotation

The THz ranging system allows motion over a wide range of angles. Before carrying out measurements it is important to ensure that the reflecting surface of the prism coincides with the rotational axis of the ranging system. This way the focus at the prism TIR face will remain fixed when the receiver arm undergoes any rotational movement. Before arriving at the procedure described in the following paragraph, there were many trials and failed methods to align the ranging system. The following steps outline the alignment procedure.

a) A thin long cylinder is inserted at the focal plane in confocal geometry. The THz-TDS system is optimized in the confocal configuration before the insertion of the cylinder. The stacked rotation and linear stages used for sample mounting were zeroed.

b) With the cylinder in place as reference, the length of the system is increased by sliding the lenses in the cage system. These distances were obtained from the Gaussian beam calculation. The distance between the short focal length lenses (f_2 = 50 mm) in each arm and the cylinder is increased from 50 mm to 67 mm, making the THz TDS spectrometer non-confocal.

c) Keeping the optical elements in the transmitter arm in place, the cylinder is removed temporarily. The optics in the receiver arm along with the receiver is moved towards the transmitter such that the system is back to confocal distances. The THz signal is optimized in this direct transmission configuration.

d) Having optimized the signal, the optics in the receiver arm are set to their original positions which overall corresponds to a non-confocal length. There may be some reduction in the signal due to non-ideal alignment but no attempt is made to optimize the THz signal in this non-confocal configuration.

e) The prism mount assembly consisting of the cradle holder and various stacked rotational and linear displacement stages is then seated onto the magnetic base and is moved to match the distances with the cylinder. The cradle holder ensured that the TIR face was co-aligned with the rotational stages.

f) The THz signal is optimized with the prism, noting losses due to Fresnel reflections.

5.3.2 Uncertainty in the beam position at the focus

Ideally, the focus will be co-located with the reflecting surface of the prism, equidistant from the two short focal length lenses. But due to systemic changes, this position is challenging to locate. The introduction of the prism and the care required to ensure that the alignment is correct can lead to positional and angular changes through the system. A change in the Si lens on the transmitter could lead to slightly off axis propagation, which can then lead to a dramatic shift in the beam location on the receiver. This can be compensated both by the angle and position of the prism to achieve a high signal, but results in a poorly aligned terahertz beam path. The method used in this work to obtain an estimate of the location of the terahertz focus is as follows:

a) A 20 mW compact laser with a center wavelength of 780 nm is utilized to isolate the focal spot on the TIR surface. This technique relies on the generation of photocarriers near the surface so that the silicon surface behaves like a metallic surface. And the reflection from a metallic surface causes a relative phase shift compared to the reflection from a dielectric which in turn causes a change in the integrated signal at the receiver due to destructive interference. The laser is steered in the x and y directions until the THz signal is minimized which coincides with the THz beam focus. A change in the terahertz signal with the laser on and laser off is noted.

b) With the 780 nm laser beam position set, a 5 mW He-Ne laser centered at 630 nm is then steered to coincide with the 780 nm laser position. The two laser beams are made to overlap as close as possible using steering mirrors. And the higher power 780 nm laser is turned off for safety.

c) The receiver arm is rotated to $\theta = 45°$. The He-Ne beam spot acts a visible low power marker to the terahertz beam focus [see Figure 5-12].

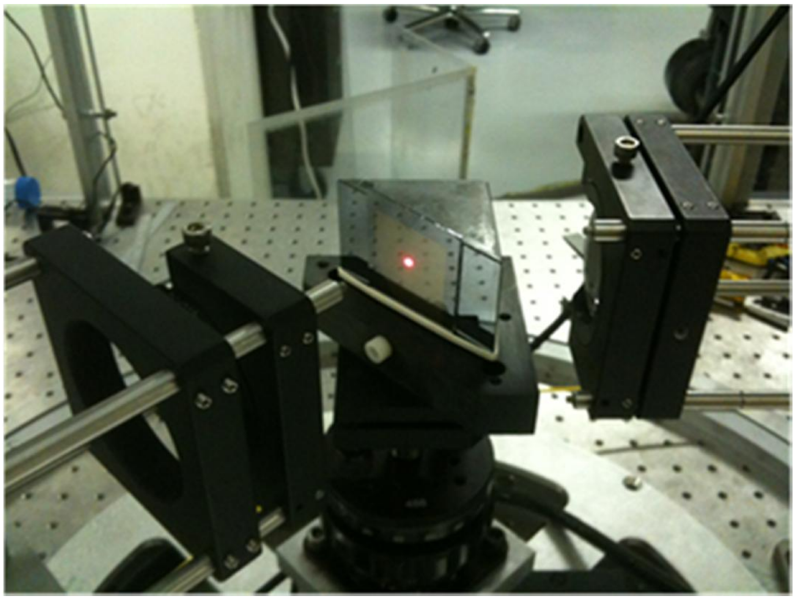

Figure 5-12 Terahertz focus detection

5.3.3 Optical adhesion

Based on the Kretschmann ATR configuration, the samples were contact mounted onto the TIR surface. Once again attempts were made to mount the sample onto the prism without scratching the prism and preventing any air gaps. Rubber bands, sticky tape etc. were used to mount the sample but the risk of the sample sliding off or application of too much pressure due to the rubber bands were causes for concern as it could result in damaging the sample or the only Si prism available. The following method worked reliably. A drop of methanol was used on the back surface of the cleaned substrate and immediately contacted onto the clean prism via surface tension. Additionally, rubber bands were wrapped around the prism at the top and the bottom of the prism to prevent the sample from accidentally falling onto the optical table. The samples and prism were cleaned each time to ensure good optical contact. Index matching fluid such as benzene, a non-polar solvent can be used in normal cases, but was not easily accessible at Los

Alamos National Laboratory requiring significant administrative and procedural changes to standard operation. Perfect contact is hard to achieve outside of an ultraclean environment and hence an air gap between the substrate and the TIR surface is always present. Necessary steps are taken to minimize this effect which is evident as ringing in the THz temporal waveform. Due to the variable presence of air gaps introduced by repositioning a metafilm sample and a separate bare reference substrate, the bare prism was chosen as the most reproducible reference instead of bare substrate for consistency.

6 Experimental Results

This chapter contains the experimental results obtained from metafilms using THz- attenuated total reflection technique and is broadly divided into 1) Initial measurements on small metafilm arrays and 2) ATR measurements on improved large metafilm arrays and 3) re-radiation measurements on improved large metafilm arrays. The impact of various factors such as beam position, SRR array sizes etc. are discussed in detail.

6.1 Initial measurements on small metafilms

Due to limited initial availability of samples, measurements were performed on SRR arrays on hand. The samples which consisted of 1 cm^2 SRRs on 375 μm thick GaAs substrates (see Chapter 4) had a measurable transverse area deemed sufficient for transmission measurements as the only requirement is that the sample area be larger than the incident THz beam area. A single 4” GaAs substrate was processed to create several 1 cm^2 SRR arrays with varying unit cell sizes and SRR sizes.

6.1.1 Initial ATR measurements

The measured fundamental resonance for the small sample with periodicity of 100 μm occurs at 0.38 THz. The s-polarized THz field excites the *LC* resonance of the SRR elements on the GaAs surface. For this measurement (see Figure 5-2 for experimental setup), the incident terahertz radiation has an electric field component parallel to the gap bearing arm and a net magnetic field component perpendicular to the plane of the SRRs while undergoing TIR (combined E & H excitation). Figure 6-1 shows ATR time domain measurements performed on the small metafilm. The plot contains the reflected terahertz signals in the time domain for the bare prism, prism with a bare GaAs substrate 375 μm thick and the ATR signal for the metafilm when the beam position is centered on the 1 cm^2 SRR array. These waveforms were measured when the receiver is oriented at 90° from the transmitter ($\theta = -90°$).

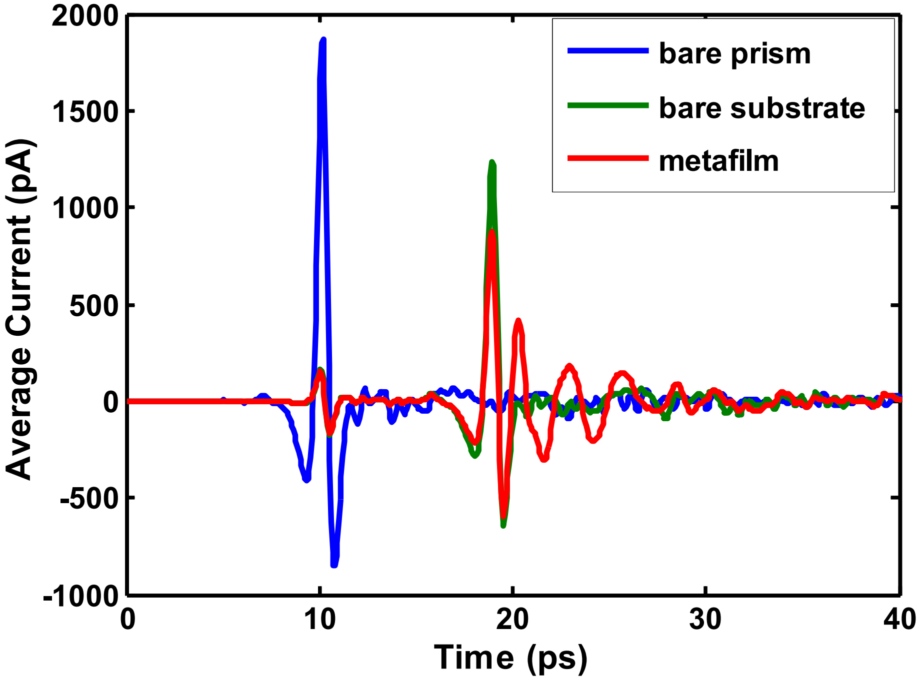

Figure 6-1 Temporal ATR waveforms of bare prism, bare substrate and 1 cm^2 metafilm sample.

The Fresnel reflection from the first surface occurs around 10 ps before the main ATR pulse and is coincident with the signal from the bare prism. The Fresnel reflection is prominent, implying that the adhesion of the sample to the prism was not good. There is also a small reflection trailing the primary pulse by approximately 11 ps that adds periodic structure on all the spectra. It is due to the optical reflection in the transmitter. Although this is a small pulse, it does create some beating in the spectra and is an artifact of the experimental system.

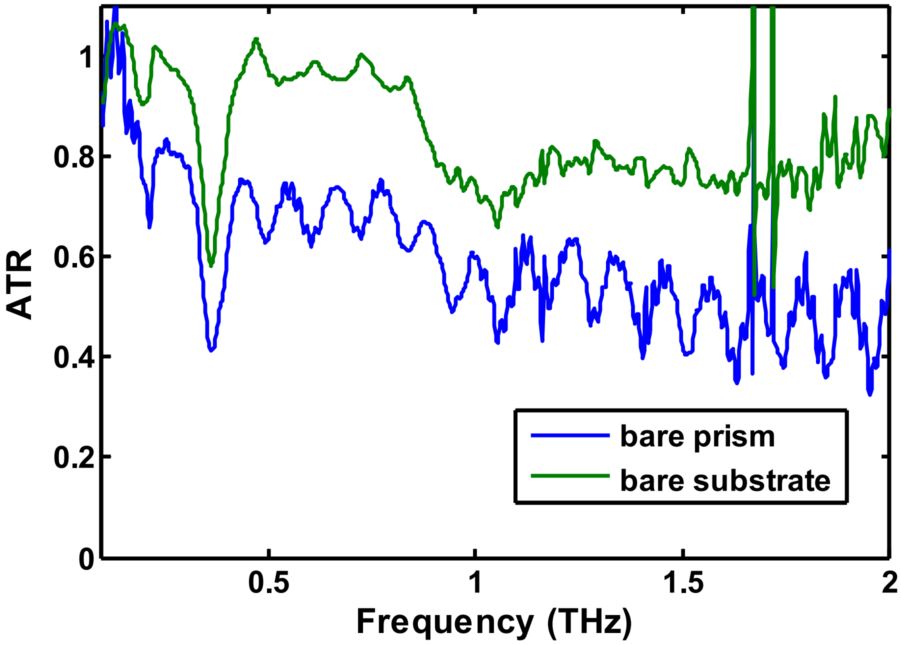

Figure 6-2 Frequency dependent ATR using prism reference (blue) and silicon substrate reference (green).

The frequency dependent amplitude reflection coefficient with a suitable reference yields the amplitude ATR coefficient, $r_{ATR}(\omega) = E_{ATR}(\omega)/E_{ref}(\omega)$. $E_{ATR}(\omega)$ and $E_{ref}(\omega)$ are the reflected spectra from the reference with and without the sample respectively. Figure 6-2 shows the ATR coefficients referenced to the bare prism and bare substrate signals respectively. The sharp dip in the reflection coefficient near 0.4 THz corresponds to the fundamental *LC* mode whereas the broad dip at higher frequencies near 1 THz corresponds to a higher order dipole mode. The expected magnitude of the reflection coefficient for a TIR boundary between silicon and air for oblique angle of incidence beyond the critical angle is 1. But the measured off-resonance reflection coefficient using reference as the bare prism is much less than 1. The reason for this reduction is misalignment at the receiver and uncertainty in the position of the prism. The effect of the air gap in the sample waveform is seen as ringing in the spectra for both spectral coefficients.

The corresponding measured magnitude using bare substrate as reference is closer to the expected reflection coefficient. Since the sample did not have > 5 mm space devoid of SRRs, a separate blank substrate of GaAs was used. This introduced experimental artifacts dependent on the mounting of the sample and the substrate reference. There is additional uncertainty due to the reflection from the air gap between the silicon prism and the GaAs substrate.

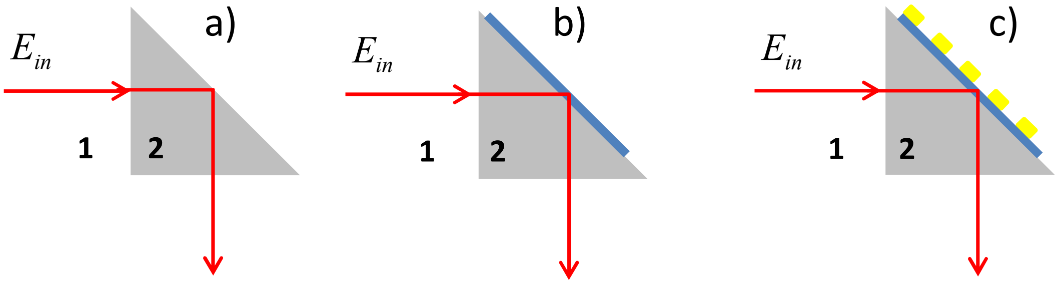

$$E_{prism} = t_{21} r_{21} t_{12} E_{in} \qquad E_{substrate} = t_{21} \tau'_{22} r_{21} \tau'_{22} t_{12} E_{in} \qquad E_{sample} = t_{21} \tau_{22} r_{ATR} \tau_{22} t_{12} E_{in}$$

Figure 6-3 Resultant electric field for a) bare prism, b) bare substrate and c) sample.

It is difficult to obtain identical Fresnel reflections from the air gaps between the sample and the reference after physical replacement of the reference substrate and sample. Figure 6-3 shows the resulting electric field for the three possible measurements with associated Fresnel transmission and reflection coefficients. τ_{22} (τ'_{22}) represents transmission through the air gap for the sample (bare substrate). Thus introducing the separate reference substrate adds an additional experimental error. This is evident from equations (6.1) and (6.2). $|r_{21}|$ is equal to 1 for total internal reflection so it can be ignored for absolute magnitude but will still impart a phase shift.

$$\frac{E_{sample}}{E_{substrate}} = \frac{t_{21}\tau_{22}r_{ATR}\tau_{22}t_{12}E_{in}}{t_{21}\tau'_{22}\,r_{21}\tau'_{22}\,t_{12}E_{in}} = \frac{\tau_{22}^{2}}{\tau'^{2}_{22}}\frac{r_{ATR}}{r_{21}} \tag{6.1}$$

$$\frac{E_{sample}}{E_{prism}} = \frac{t_{21}\tau_{22}r_{ATR}\tau_{22}t_{12}E_{in}}{t_{21}r_{21}t_{12}E_{in}} = \tau_{22}^{2}\frac{r_{ATR}}{r_{21}} \tag{6.2}$$

$|\tau_{22}|$ will always be ≤ 1, so the sample with the reference as the prism [equation (6.2)] will have a reduced spectral amplitude. But the sample with the reference using a separate bare substrate [equation (6.1)] where $\tau_{22} \neq \tau'_{22}$ would give rise to a reflection coefficient possibly greater than 1.So it was decided to use the bare prism as the reference for ATR measurements.

6.1.2 Initial Re-radiation measurements

It was conjectured that the SRRs would act as loop antennas and could possibly re-radiate across the TIR boundary. The conventional thinking at this point was that there should be no observable signal. This conjecture was hotly contested and utilizing the available experiment, this hypothesis was tested.

After aligning in 90° ATR configuration, the receiver arm was rotated to be normal to the prism TIR surface (see Figure 6-4).

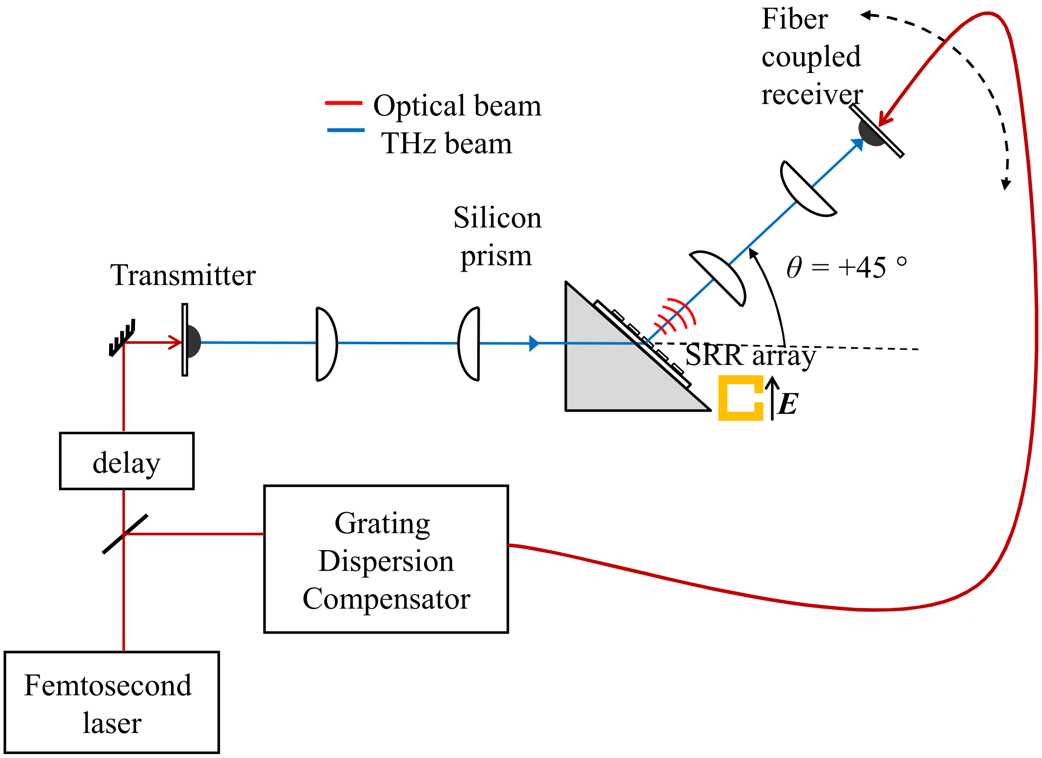

Figure 6-4 Experimental layout to detect re-radiation**.** Incident electric field polarized as indicated.

A re-radiated signal across the TIR boundary was observed using THz-ATR where no signal was expected. The measured re-radiation signal is shown in Figure 6-5.

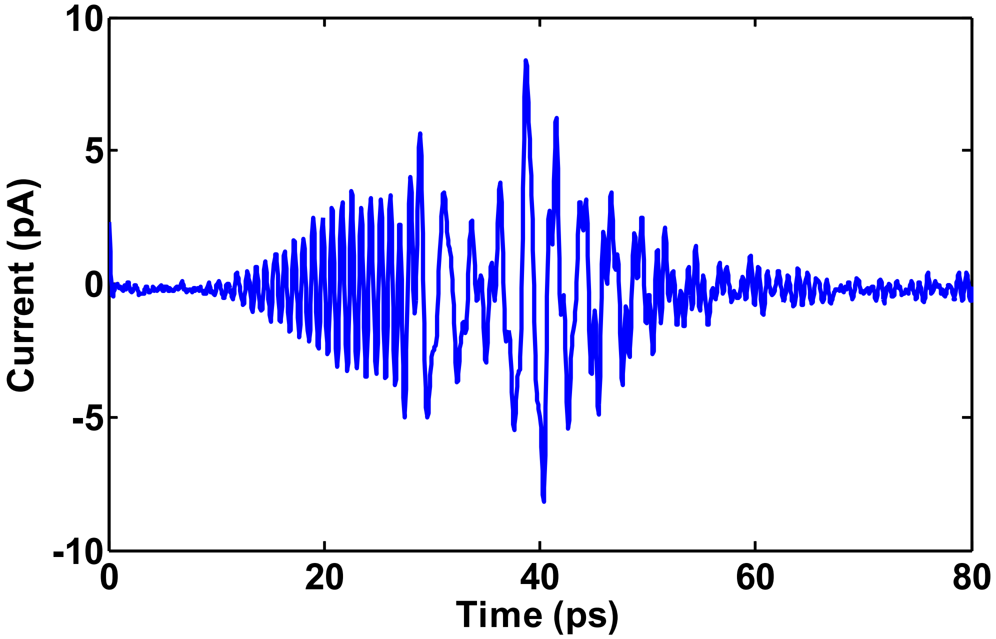

Figure 6-5 Re-radiation signal from a 1 cm^2 metafilm array.

This signal was measured across the TIR boundary at the fundamental *LC* resonance which indicated that the SRR array was intimately involved with this re-radiation mechanism. Re-radiation appeared to be concentrated near the edge of the arrays as determined by physically blocking the signal. To further probe the directionality of this signal, the THz detector was rotated by ± 20° with respect to the normal of prism's diagonal face ($\theta = 45°$) and the re-radiation signal was recorded.

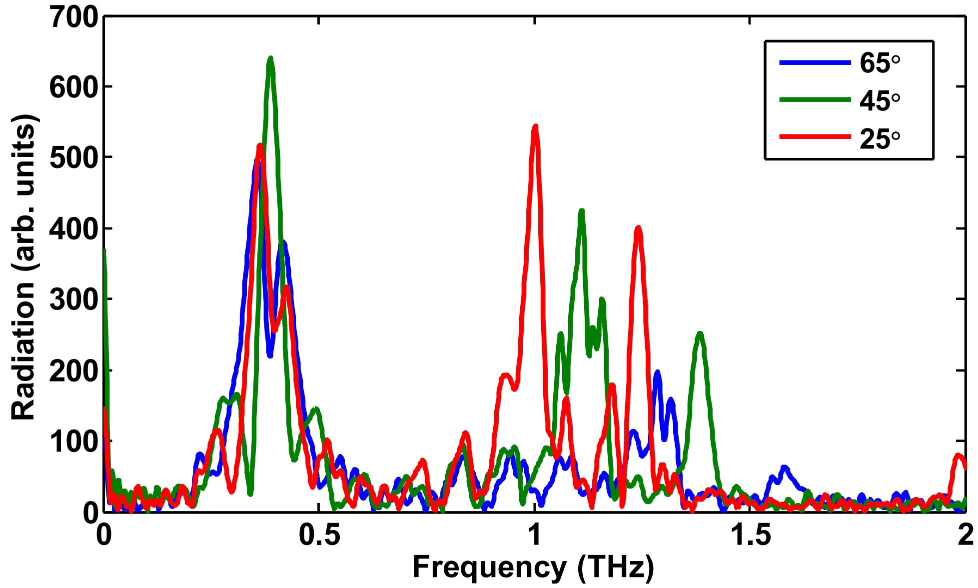

Figure 6-6 Angularly resolved spectra for re-radiation measurements at 25°, 45°and 65° from the optical axis, showing *LC* radiation and transmission grating signals.

Figure 6-6 shows the corresponding THz spectrum of radiated THz pulses at three different angles. The re-radiation spectrum is comprised of a low frequency *LC* resonance component at ~0.4 THz and high frequency components around 1.0 THz, a grating response due to the periodic nature of the array that will be discussed later. The high frequency response is identified as peaks due to the transmission grating signals. These initial measurements did not show any shift in *LC* resonance frequencies with changes in detection angle but the transmission grating response shifted with a change in the detection angle.

These unexpected results justify the use of THz-ATR in investigating finite SRR arrays. The re-radiation signal would be difficult to observe except in an ATR configuration with a low background signal. Illuminating the SRR array with a terahertz beam away from the edge shows a barely detectable re-radiation signal. The effect is suppressed but still present. Noise in the receiver is the main contributor to the background signal.

In standard transmission THz-TDS measurements with metamaterials, small changes are dominated by a large background signal i.e. broad bandwidth pulse. The peak field of the incident main pulse to that of the re-radiated field is on the order of 200:1 and could be easily overlooked as unimportant noise. Loss or scattering mechanisms are not considered that can potentially change the measured response. The collection optics would capture transmitted fields through the sample at normal incidence and close to normal incidence angles. Any non-paraxial radiation or radiation that occurs later in time is not measured. Therefore the re-radiation signal would not be measured in the direct transmission configuration. Any variations would be attributed to the noise in the system and would go undetected.

6.1.3 Issues with small samples

There were many issues that arose with the physical nature of these small metafilm arrays. With a beam waist diameter of ~ 5 mm on the TIR surface, the positional uncertainty is on the order of the beam size which is on the same order as the size of the small array. At this point, although crude measurements indicated the radiation seemed to be strongest from near the edge, it was unclear what precisely was occurring. All the SRRs had the same outer dimension so the *LC* resonance did not vary from array to array. The unit cell size varied from array to array, which resulted in the transmission grating response varying from sample to sample. The arrays were spaced close together to maximize the yield of a single wafer. However this resulted in beam overlap of multiple arrays, unless the beam was well centered on the array. The sample was fabricated on GaAs substrates preventing good optical contact. With an index of 3.6 compared to the Si prism of 3.42, ensured that there would always be a Fresnel loss at the interface.

6.2 ATR measurements on improved metafilms

6.2.1 Improved metafilm arrays

New larger metamaterial arrays as described in Chapter 4 were required to isolate the observed effects in both the ATR and re-radiation measurements. This led to the fabrication of large samples in order to minimize the impact of positional uncertainty of the THz beam with respect to the array. The measurements on larger SRR arrays gave new insight. The following sections focus on measurements done on the newer large SRR arrays.

They were also fabricated on double polished Si substrates that gave no index difference resulting in improved optical contact with the Si prism. The substrate was also thicker to increase the time window limited by secondary reflections. The arrays were significantly larger at 2.5 cm x 2.5 cm than the largest beam dimensions and still fitting on the prism face. The geometries of the SRRs were varied, so different *LC* resonances could be observed in re-radiation. The unit cell size was fixed, which resulted in the transmission grating response being the sample for all samples.

6.2.2 *Effect of beam position on ATR spectra*

The ATR measurements were repeated on the 2.5 cm x 2.5 cm SRR arrays (MM1, MM2 and MM3) which were initiated to investigate the impact on measurements due to uncertainty in the position of the terahertz beam with a smaller 1 cm x 1 cm array size.

The largest SRR array MM1 was measured at two different positions in the ATR configuration ($\theta = -90°$), with the terahertz beam focused at the center and at the edge of the SRR array. Figure 6-7 a) shows a comparison of the ATR THz signals in the time domain for two beam positions on the sample, one near the edge of the array and one centered on the array.

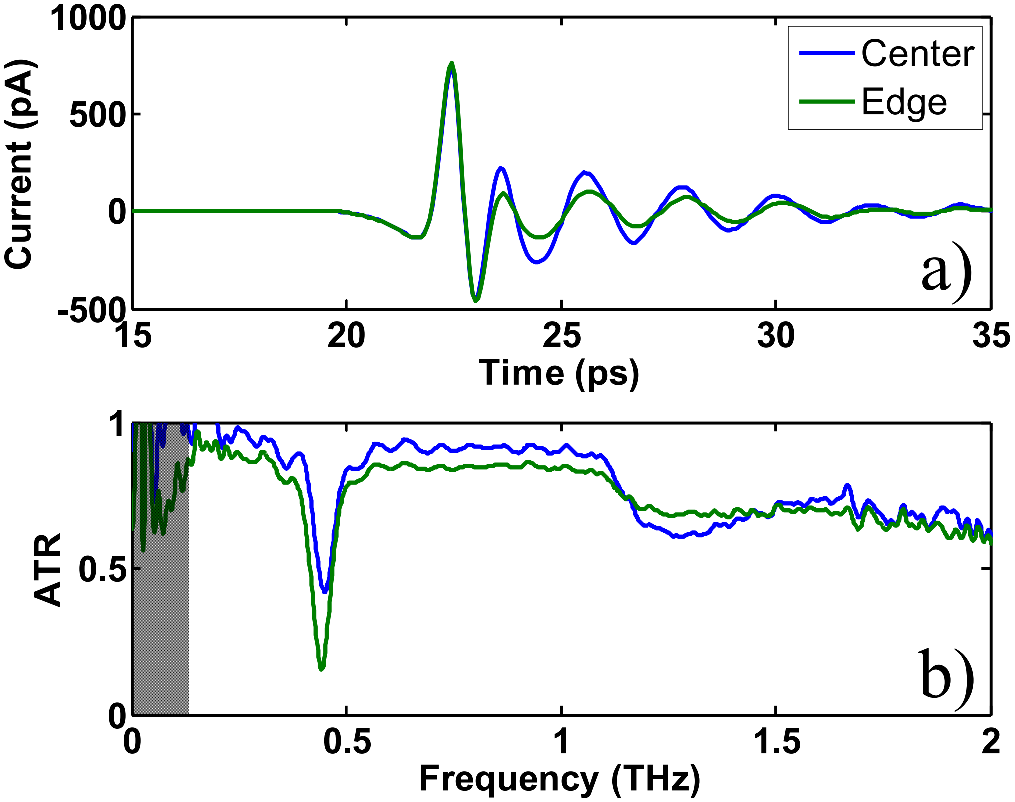

Figure 6-7 Comparison of ATR measurements on sample MM1 for incident beam at the center (blue) and edge (green). a) Reflected terahertz signals and b) ATR coefficients.

The ratio of the Fourier transformed spectra of the temporal waveforms in Figure 6-7 a) with a suitable reference yields the ATR coefficient. The magnitude of the ATR coefficient is plotted in Figure 6-7 b). Here only the attenuated total reflection coefficient with reference as the bare prism is shown for clarity. An immediate observation from Figure 6-7 b) is that the reflection coefficient in ATR is 63% lower when the terahertz beam is near the edge of the MM array than when it is in the center of the array. This behavior was unexpected. One would expect the response to be weaker when measurements are made at the edge since fewer SRRs are illuminated as is the case with the transmission measurements as is discussed in a following section. The cause of the reduction in the reflection coefficient near the edge which would appear as a strengthening of the LC resonance response is henceforth referred to as the “anomalous edge enhancement”. Thus the uncertainty in the beam position led to the observation of this edge resonance enhancement, indicating the position of the excitation beam on the finite sample array was a concern.

To investigate this anomalous resonant behavior, the sample position with respect to the point of excitation d_{edge}, was varied across the width of the MM samples and the reflected signals were measured. Here d_{edge} is the relative displacement of the array with respect to the incident THz beam and increasing positive numbers for d_{edge} imply that the beam is within the array and moving towards the center, schematically shown in Figure 6-8. For example, $d_{\mathrm{edge}} = 0$ mm at the edge of the array and $d_{\mathrm{edge}} = 12$ mm at the center. With a change in the sample position, the distance between the edge of the prism and the edge of the sample was noted for each measurement. This determined how far the array was moved. The edge of the prism was best suited as a reference for maintaining relative position changes rather than using the HeNe laser as a marker. For every position d_{edge}, the sample was reseated manually, often times requiring re-application of methanol to help achieve optical contact. The position of the incident beam and the prism was fixed.

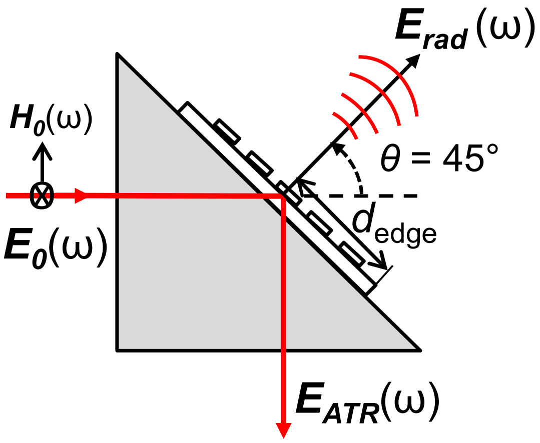

Figure 6-8 Schematic for ATR position dependent measurements**.**

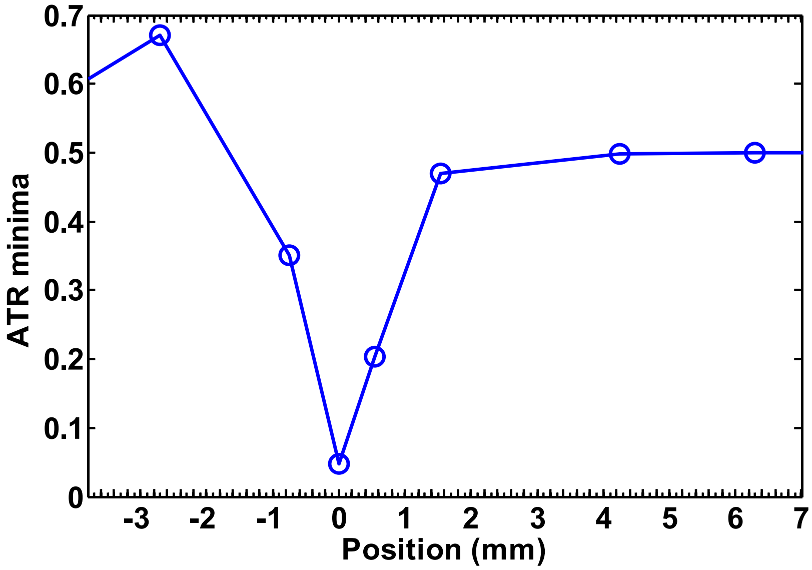

Figure 6-9 Magnitude of the on-resonance ATR coefficient of sample MM1 as a function of the displacement d_{edge}.

The magnitude of the ATR spectrum of MM1 is plotted in Figure 6-9 around the resonance frequency of 0.45 THz as a function of the displacement d_{edge}. The region $d_{\mathrm{edge}} > 2$ mm shows minor variation in the resonant response and is considered to be the infinite array regime, where edge effects are not significant. Below $d_{\mathrm{edge}} = 2$ mm, there is a marked decrease in the reflection coefficient. It would appear that the absorbance A is anomalously enhanced at the edge of the SRR arrays by 29 % for MM1 where $A = 1 - R = 1 - |r|^2$. Datapoints beyond $d_{\mathrm{edge}} = -3$ mm can be ignored since the beam is partially in the silicon substrate and is no longer in the SRR array entirely and is approaching the physical edge of the substrate. The uncertainty in the position of the THz beam in these experiments is 0.4 mm.

Identical THz-ATR spatial measurements as described earlier for MM1 were performed on samples MM2 and MM3 for various beam positions to investigate the anomalous edge enhancement.

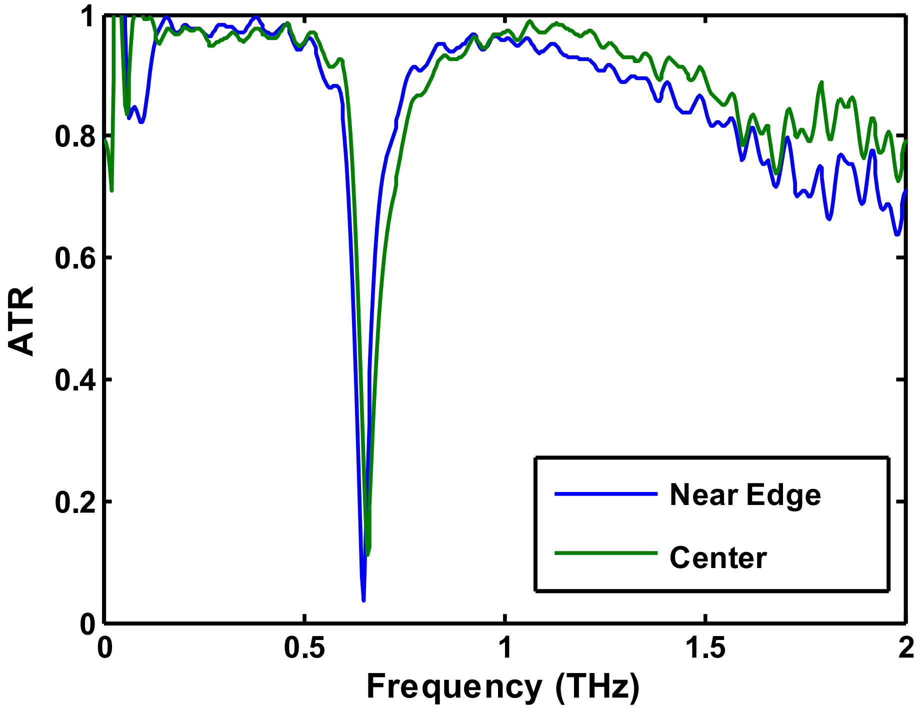

Figure 6-10: Measured ATR coefficients of MM2 for the edge (blue) and center (green) beam positions

The measured frequency dependent amplitude reflection coefficient for MM2 sample derived from the Fourier transformation of the temporal waveforms for two different beam positions is plotted in Figure 6-10. The resonance dips exhibit a small change for the edge and center beam positions.

Similar measurements were made on MM3 and the measured frequency dependent magnitude of the reflection coefficient is shown in Figure 6-11 for two different beam positions.

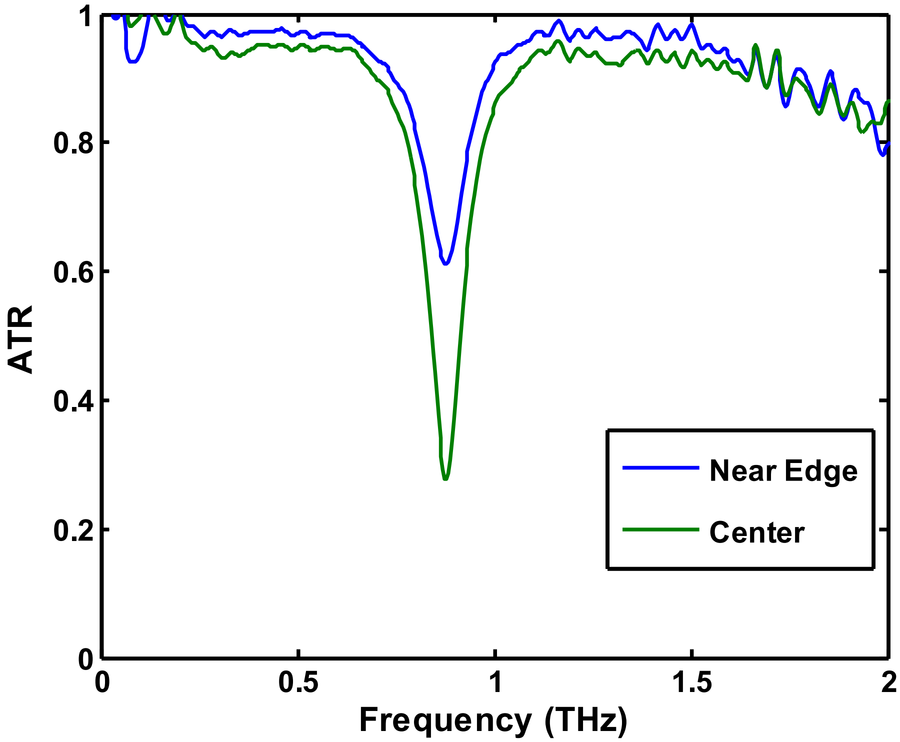

Figure 6-11: Measured ATR coefficients of MM3 for near edge (blue) and near center (green) beam positions

In contrast to the reflection response seen in samples MM1 and MM2, here the response is stronger at the center rather than the edge.

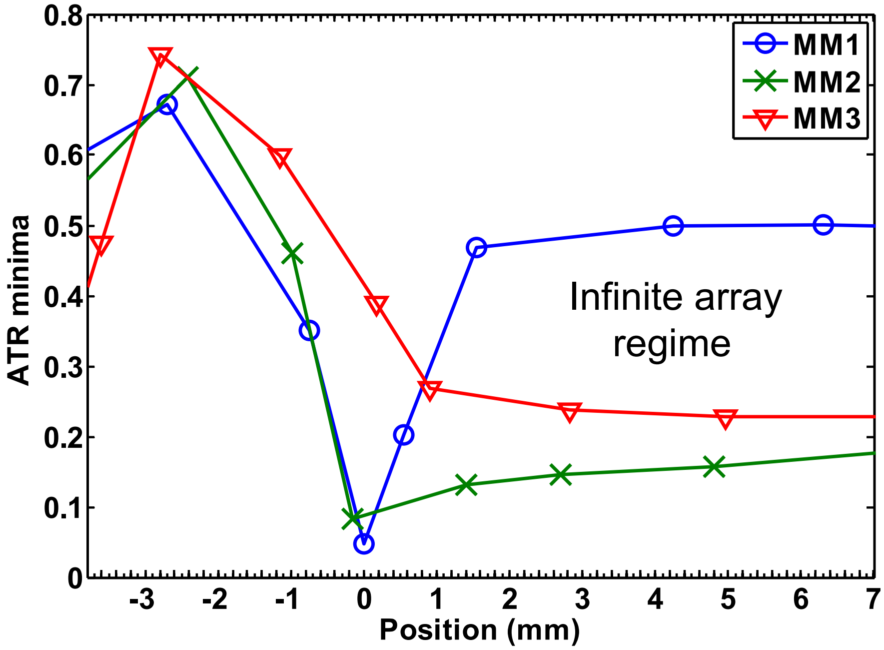

Figure 6-12: Comparison of position dependent on-resonance reflection (ATR) coefficients for MM1, MM2 and MM3.

Figure 6-12 compares the position dependent reflection coefficients for the three large SRR arrays at their fundamental resonances. Spatially resolved reflection measurements with MM2 (green x curve in Figure 6-12) show a small dip in the reflection coefficient at/near edge. The edge for the 0.64 THz resonance (MM2) occurs at a relative position of −0.2 mm. This is likely due to the uncertainty in the relative beam positions between samples. There is a ~36% relative decrease in the reflection coefficient for MM2 from the center to the edge of the array compared to the 89% change in the reflection coefficient for sample MM1. MM3 displays a different behavior with the resonance dip decreasing towards center (red curve in Figure 6-12).

Perhaps this is due to the decrease of inter-element coupling at the *LC* resonant frequency. The SRRs interact with adjoining cells inductively and/or capacitively [95].

So the current driven in one element can cause currents in neighboring elements. With a fixed unit cell for all arrays, the actual separation between elements changes with SRR size and can be effectively expressed in units of resonant wavelength.

The anomalous edge enhancement is most strongly observed in MM1 with SRR separations of $\lambda_0/9$ and not observed with MM3 which has $\lambda_0/4$ spacing between elements. Here λ_0 is the resonant wavelength of the SRR in free space. One could conclude that the more densely packed elements would potentially interact—share energy—while the less densely packed SRRs would be isolated from neighboring elements. For all samples, when the beam is well centered within the array, the ATR minima are no longer a function of position. The response is considered to be that of an infinite array.

6.2.3 Effect of beam position on Transmission spectra

The question arises: is the anomalous behavior an effect confined to ATR or is it due to the behavior of illuminating a metamaterial near an array boundary? Further measurements were carried out in standard THz-TDS transmission and reflection modes on the same samples as a function of beam position on the array.

Characterization of the resonance of these metafilms is commonly performed by measuring the relative change in a broad transmission spectrum between the MF sample and reference signals shown in Figure 6-13 (top panel). The corresponding spectra are plotted in Figure 6-13 (bottom panel).

The ratio of these spectra $t(\omega) = \dfrac{E_{sam}(\omega)}{E_{ref}(\omega)}$ is the MF transfer function. The MF transfer function for MM1 was measured using the THz-TDS ranging spectrometer in direct transmission mode (refer to Figure 5-1) where the angle with respect to the line of direct THz beam transmission and the receiver is 0°.

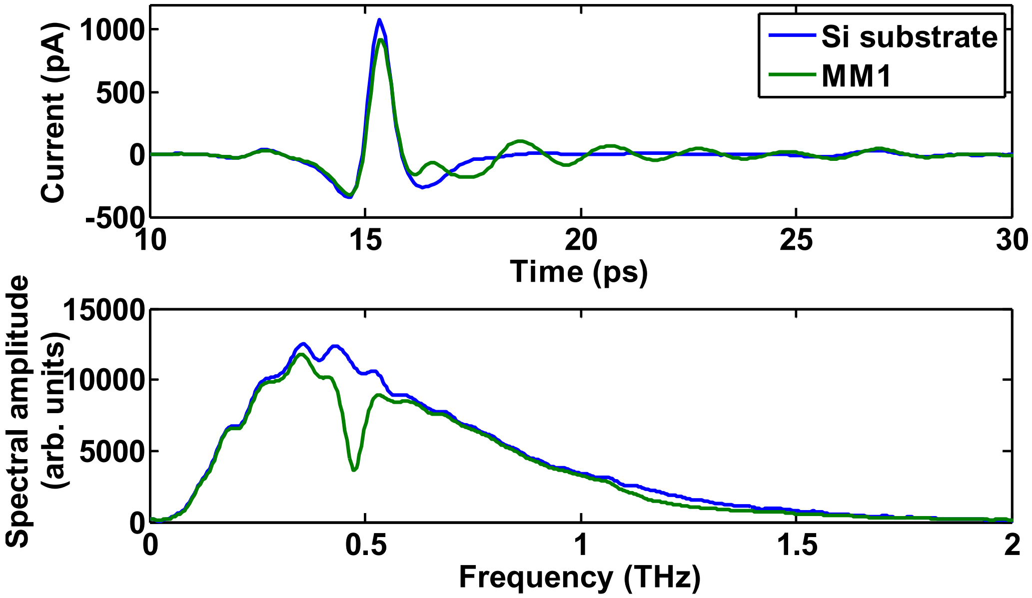

Figure 6-13 Top panel: Measured temporal waveforms for MM1 sample (green) and bare Si reference (blue). Bottom panel: Corresponding transmission spectra**.**

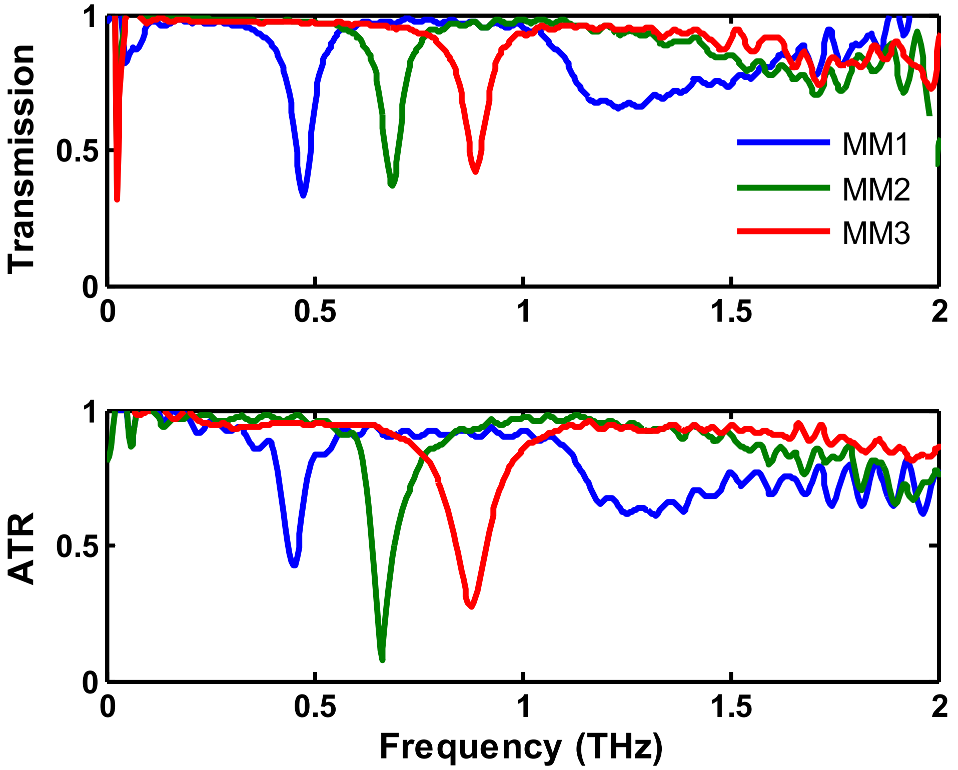

Figure 6-14 Measured transmission coefficient (top panel) and ATR reflection coefficient for samples MM1, MM2 and MM3 (bottom panel).

Figure 6-14 compares the ATR response to that obtained from direct THz-TDS transmission measurement from the three samples. The ATR measurement does show a similar behavior to transmission measurements. The transmission measurement uses a silicon substrate as a reference whereas for the ATR measurement, the sample scans were compared against a bare prism. The ATR spectra reveal that *reflection* measurements produce band-stop behavior very similar to the *transmission* response in normal THz-TDS of similar MFs. The resonance strength from transmission measurements displays a decreasing trend with an increase in inter-element spacing (MM1 to MM3), as expected. In contrast to the behavior observed in transmission, the reflection coefficient measured in ATR is smallest for MM2.

Spatial measurements similar to the THz-ATR spatial measurements seen in Figure 6-12 were conducted on the largest sized SRR sample MM1. The magnitude of the on-resonance transmission coefficient is shown in Figure 6-15 for focus positions across the width of the array.

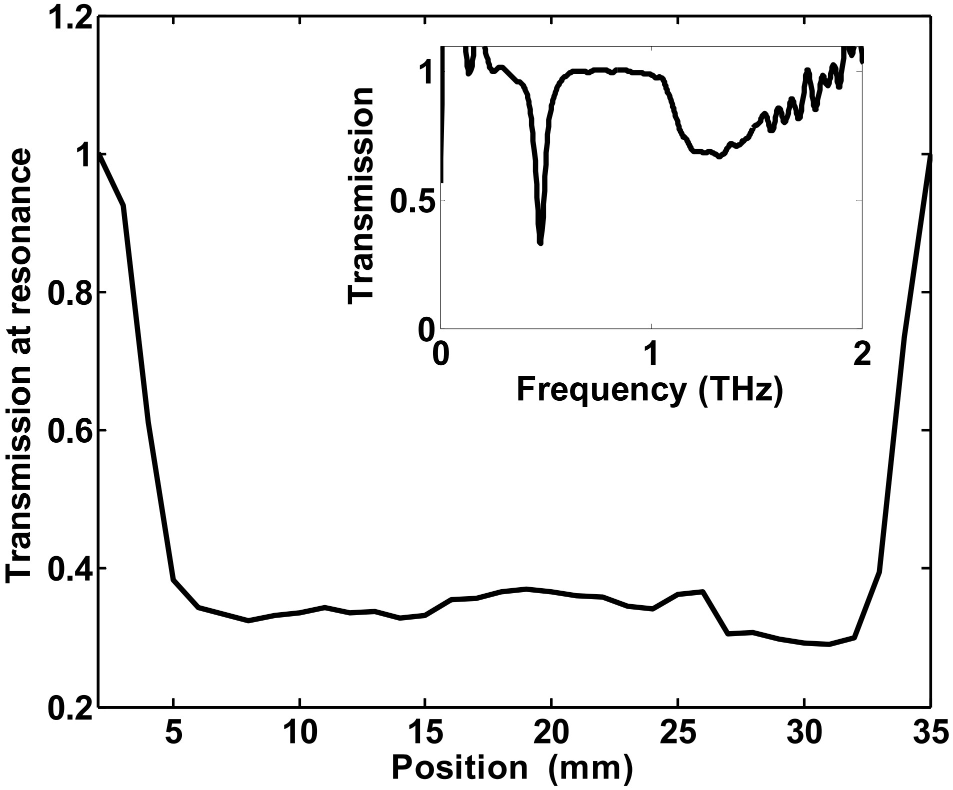

Figure 6-15 Position dependent Transmission (magnitude) at resonance for metafilm MM1. Inset: Frequency dependent transmission on resonance.

In contrast to the "anomalous edge enhancement" observed in the ATR response shown in Figure 6-12, the strength of the resonance is greater (lower transmission coefficient) away from the edges in Figure 6-15. The sample was mounted on a motorized linear stage and measurements were taken in steps of 1 mm. The range of travel for the motorized linear stage is 25 mm. In order to map out the entire width of the sample, some adjustments were made manually. The feature at 25 mm is due to this adjustment.

6.2.4 Effect of beam position on Reflection spectra

To find out if the trend observed in ATR measurements was due to the obliqueness of the incidence terahertz radiation, further studies were conducted on sample MM1 in THz-TDS reflection geometry without using the ATR prism. The schematic for this measurement is shown in Figure 6-16.

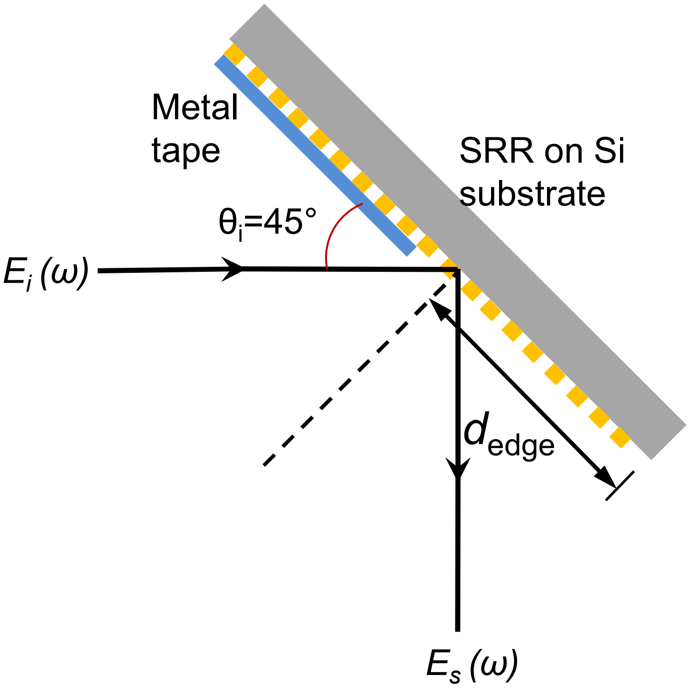

Figure 6-16 Arrangement for Reflection measurements at 45° on sample MM1. Here d_{edge} indicates the relative displacement of the terahertz beam with respect to the edge of the array.

The sample was mounted in a linear motorized stage and oriented at 45°. Half of the sample was covered with aluminum tape which served as a reference. The temporal waveforms and corresponding reflection spectra from the metal reference and from beam positions corresponding to center of the array (d_{edge} = 10 mm) and past the edge of the SRR array (d_{edge} = 3 mm) onto bare substrate are plotted in Figure 6-17.

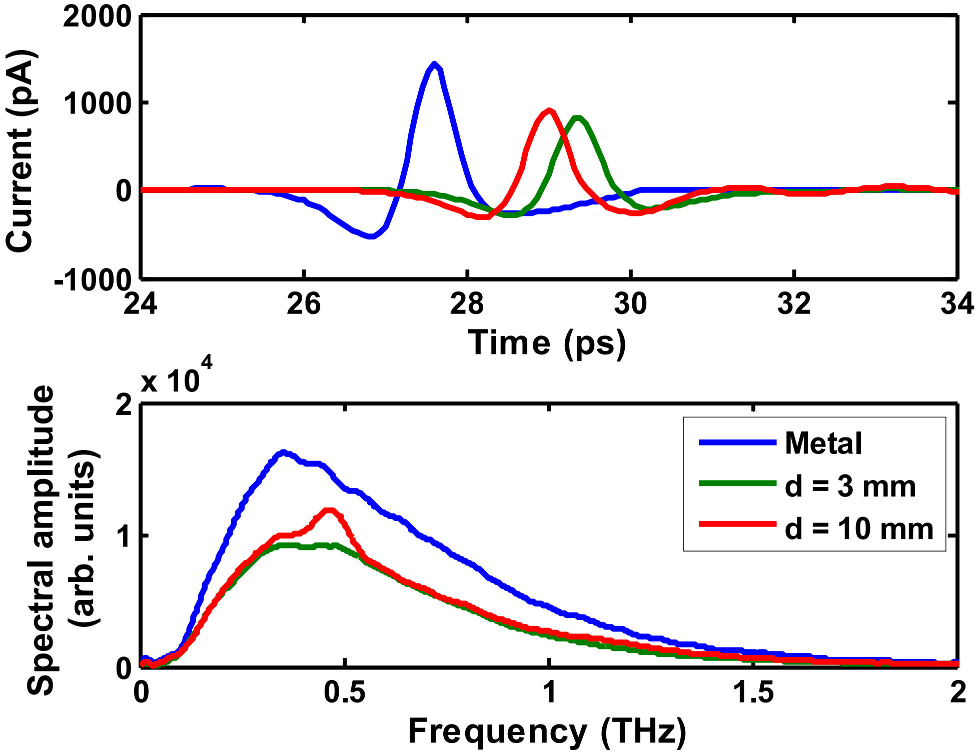

Figure 6-17 Time (top) and frequency(bottom) for THz beam positions on metal (blue), near edge (green : d_{edge} = 3 mm) and near center (red: d_{edge} = 10 mm).

The resonance appears as a peak in the reflection measurements for position d_{edge} =10 mm corresponding to the center of the array. Figure 6-18 shows the position dependent reflection response. The magnitude of the reflection coefficient is obtained through the ratio of $r_{refl}(\omega) = \left|\frac{E_s(\omega)}{E_{metal}(\omega)}\right|$ where $E_s(\omega)$ is the reflected terahertz field from the sample and $E_{metal}(\omega)$ is the reflected terahertz field from the aluminum tape.

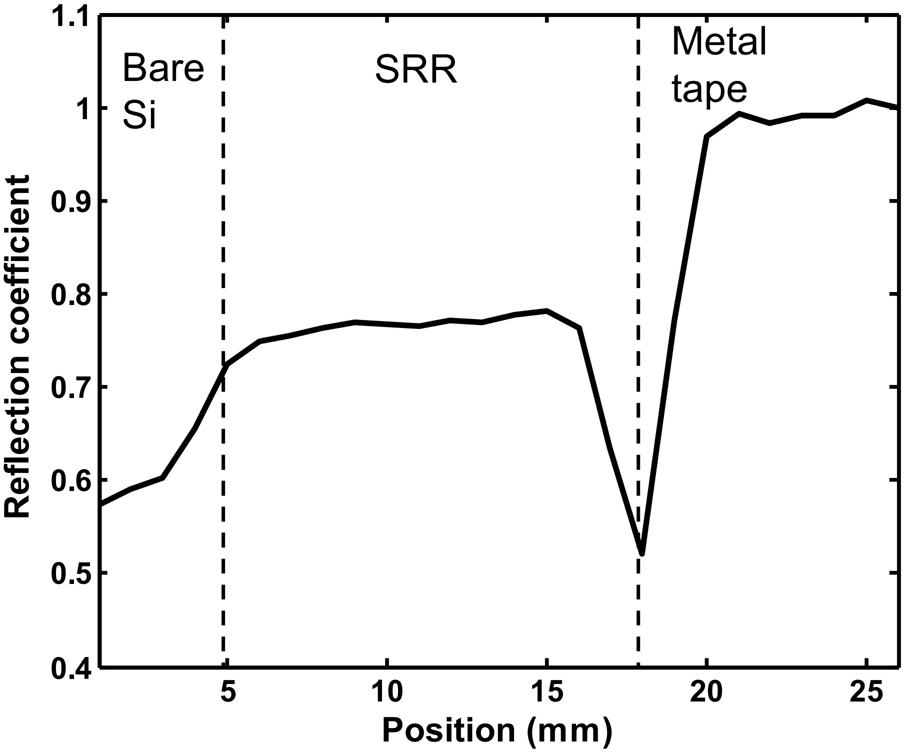

Figure 6-18 Spatially dependent on-resonance (0.45 THz) reflection coefficient for MM1 using reflection THz-TDS

The trend observed in Figure 6-18 is due to the reflection peaks instead of resonant dips seen in the transmission and ATR measurements. Comparing to the ATR measurements on MM1, there is no clear sharp transition near the edge where the response is purely due to the beam in the silicon substrate. The large dip in reflectivity between 15mm and 20mm is due to metal tape. To begin to explain this, the spectral signature for this region is broadband in nature indicating that it is due to the transition to the metallic region. The relative phase shift from the beam half on the metal reference and half on the effective dielectric surface of the SRR array is measured through an effective integration over the entire collected beam and results in destructive interference.

From the results of the spatially resolved transmission and reflection measurements, this anomalous edge effect appears to be confined to ATR measurements.

6.3 Re-Radiation measurements on improved metafilms

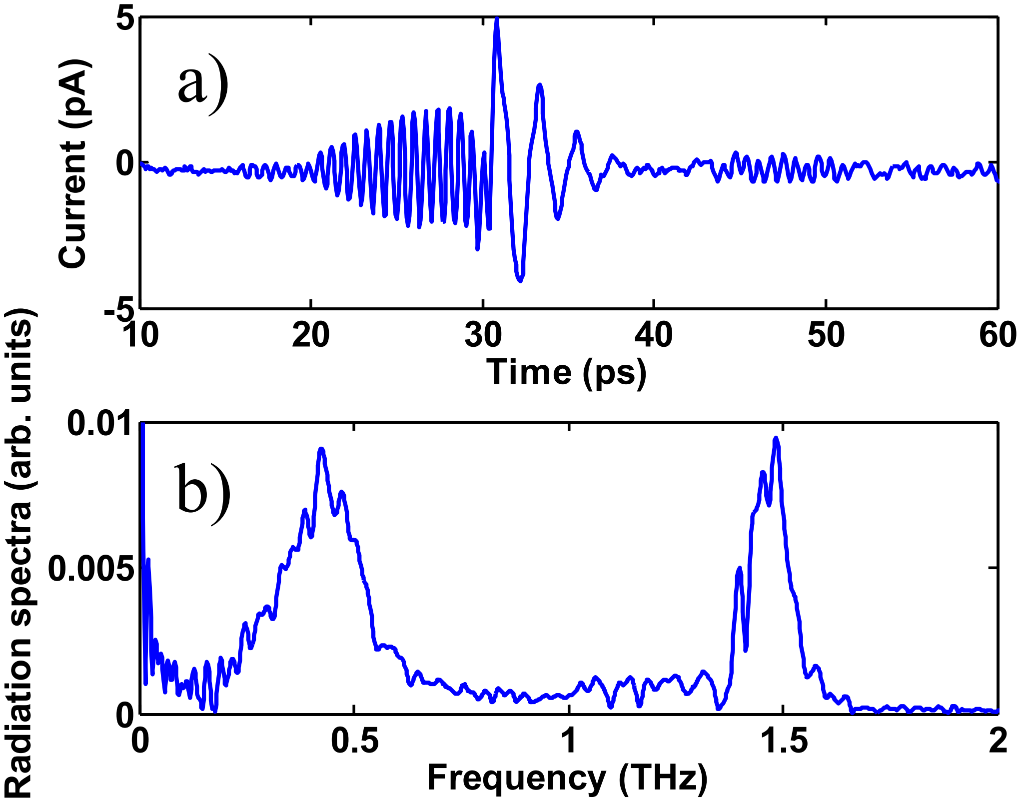

Figure 6-19 Measured re-radiation waveform in the time domain (top panel) and spectra (bottom panel) for metafilm MM1.

The re-radiation measurements were performed on the large SRR arrays MM1, MM2 and MM3. The receiver was once again oriented such that it was normal to the metafilm array on the TIR surface, or $\theta_i = 45°$ from the optical axis for direct transmission measurements (see Figure 5-1 and Figure 6-4). The incident terahertz beam was focused near the edge of the SRR array where the anomalous resonance enhancement was observed in ATR. The measured re-radiated signal for the large array MM1 in Figure 6-19 shows a low frequency response near 0.44 THz, the fundamental resonance for MM1, and a high frequency ringing at 1.5 THz.

The 1.5 THz response is due to the grating diffraction obeying the transmission grating formula, due to the 80 μm periodicity of the MF.

$$a(\sin\theta_d - n_{Si}\sin\theta_i) = m\lambda \tag{6.3}$$

where *a* is the periodicity of the metafilm and m is the diffraction grating order. θ_i is the angle of incidence and θ_d is the diffracted angle. Both the angles are measured from the normal to the TIR interface. For $\theta_i = 45°$, $n_{si} = 3.42$ and $\theta_d = 0°$ which corresponds to a grating frequency of 1.55 THz. In Figure 6-19 b), the measured grating transmission is slightly lower than the calculation. Measurements near the center show the 1.55 THz grating frequency as predicted. Measurements near the edge of the array give rise to an imperfect grating response. Unlike the traditional transmission/reflection measurement, no reference measurement was required to extract these spectral features. Qualitatively, the spectral signatures are similar but the mechanisms responsible for generating them are significantly different.

6.3.1 Beam profile measurements

To determine the spatial extent of the re-radiation, lateral displacement measurements were taken for the re-radiation configuration ($\theta = +45°$) on the metafilm MM1 similar to the beam characterization measurements shown in Figure 5-11. A schematic of the experimental layout is shown in Figure 6-20 below. Instead of generating a convolution between identical transfer functions associated with the transmitter optics and the receiver optics, the incident beam has propagated through the Si prism to strike the TIR interface with the MF. The incident beam will be elongated in the plane of incidence and will no longer match the Gaussian profile determined from simple transmission. However, the receiver arm Gaussian profile will not have changed allowing us to deconvolve the beam pattern on the surface.

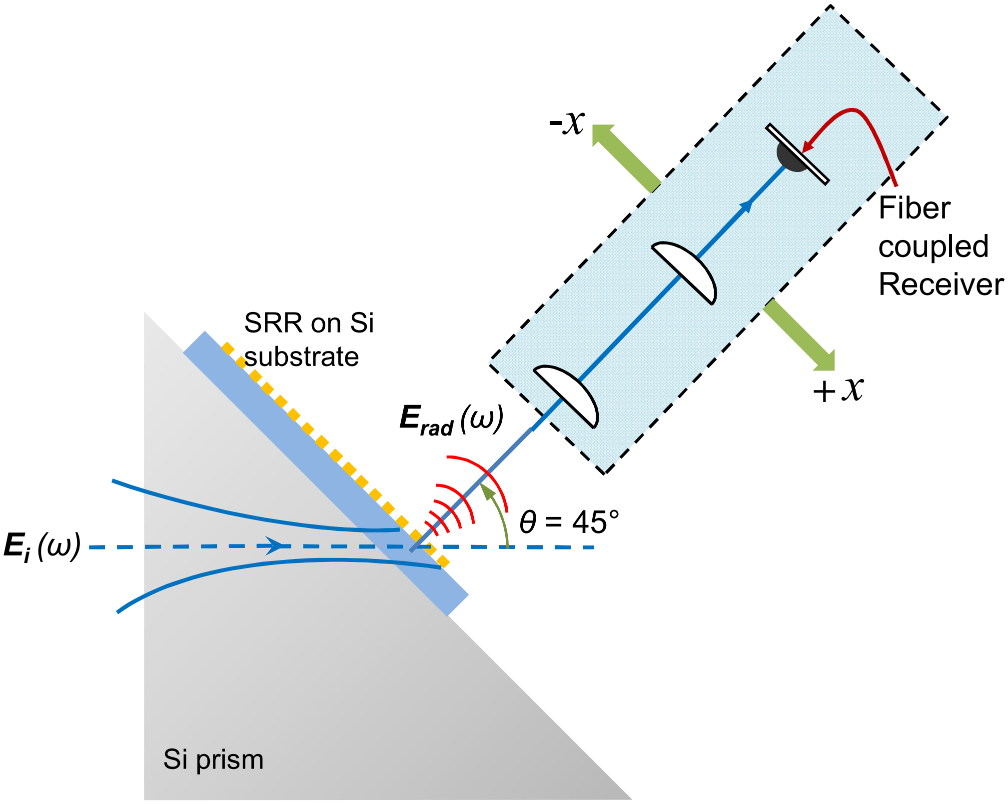

Figure 6-20: Schematic for lateral displacement measurements for re-radiation configuration.

Edge excitation

The terahertz beam was incident on the edge of the SRR array. Measurements were taken by displacing the receiver arm over the range ± 3 mm from the optical axis with a time constant of 300 ms and averaged 4 times. The *LC* curve in blue in Figure 6-21 indicates the integrated spectral magnitude for the frequency range of 0.41 THz to

0.46 THz for different lateral off-sets. The green curve indicated as grating in Figure 6-21 is the integrated spectral magnitude for the frequency range of 1.51 to 1.56 THz, which corresponds to the grating resonance that was previously measured in re-radiation at normal incidence from the plane of the MM. The average was taken in order to eliminate minor variations near the fundamental resonance mode of 0.44 THz and near the grating resonance of 1.5 THz.

The resulting lateral beam profiles as a function of the lateral movement ± *x* mm are shown in Figure 6-21. It can be seen that the *LC* response (blue curve) is no longer co-located with the grating response. The edge position measurement at the *LC* frequency

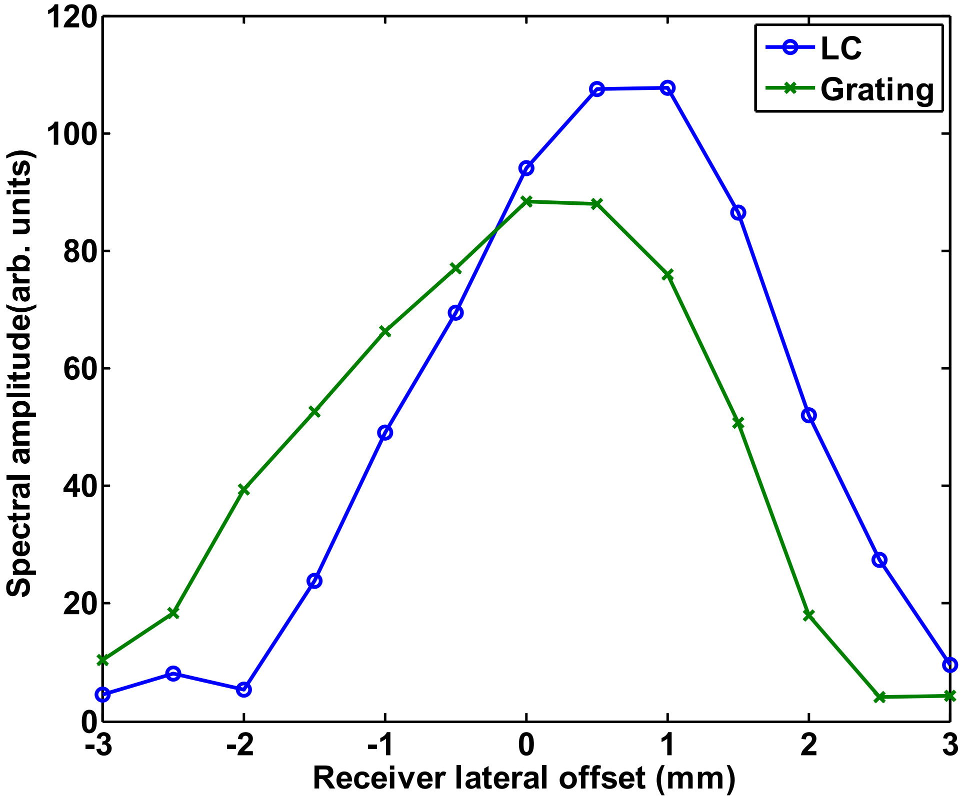

Figure 6-21: Edge excited beam profile measurements from re-radiation waveforms shown here for fundamental *LC* (blue) and the transmission grating (green) frequencies. Positive offset *x* is towards the edge and negative offsets *x* are toward the center of the array (see Figure 6-20).

shows a lateral displacement of the re-radiation signal with respect to the grating transmission toward the edge of the array. This measurement is a result of the convolution between the optical transfer function of the receiver determined from the confocal measurement plotted in Figure 5-11 and another beam profile. Initial attempts to match the resultant beam profile with a Gaussian profile convoluted with the receiver optical transfer function gave an approximate beam diameter of the incident field at the edge of the array to be 1.6 mm. Asymmetric beam shapes such as half-Gaussian and triangular were used to get a better match with the measured asymmetric beam profile for the grating response shown in Figure 6-21. But the results did not show improvement over the estimate using a Gaussian for the convolution. The deconvolved beam is clearly more complicated than these standard waveforms. The reduction in size of the estimated beam from ~5 mm to 1.6 mm can be explained by the incident beam being only partially on the array. The grating signal can only come from the portion of the array illuminated by the incident THz field.

Excitation towards center

To determine if the *LC* frequency radiation propagates along the array towards the edge and to determine if the re-radiation is an effect only observed when excitation is near the edge vs. near the center of the array, the terahertz beam was made incident on the array 5 mm away from the edge, closer to the center by shifting the entire array as described previously.

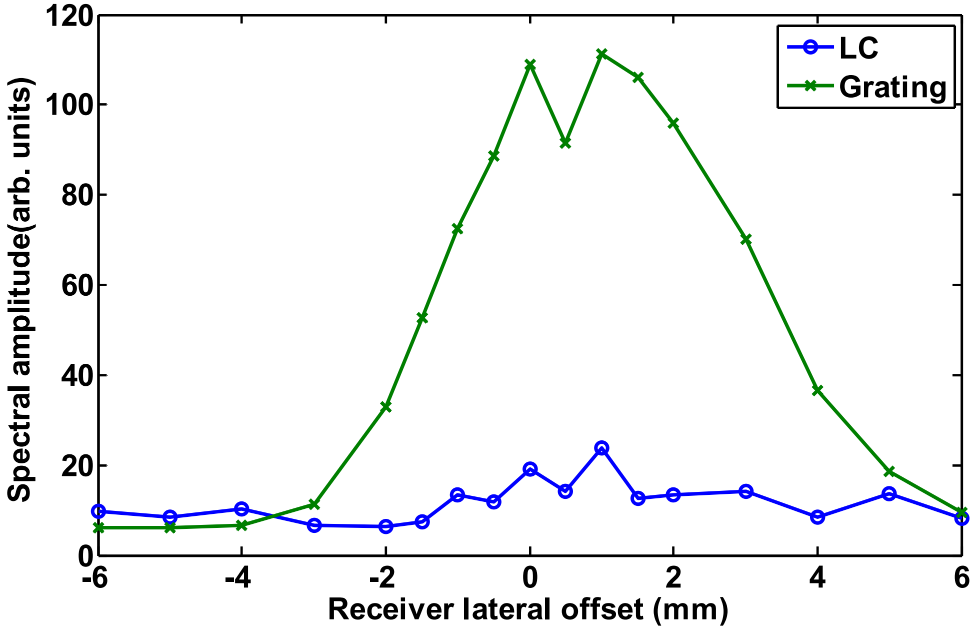

Figure 6-22: Near center excited beam profiles from re-radiation waveforms shown here for fundamental *LC* (blue) and the transmission grating (green) frequencies. Positive offset *x* is towards the edge and negative offsets *x* are toward the center of the array (see Figure 6-20).

From Figure 6-22, the re-radiation for the *LC* resonance when the beam is positioned toward the center of the array is significantly weaker by an order of magnitude than the re-radiation when the terahertz beam excites the edge of the array. This may be due to the "preferential radiation" into the high-index substrate [96] or may be due to coupling into a surface wave that can only re-radiate when it strikes the edge of the array. But the re-radiation toward the center is present and noticeable above the noise floor of the system. From these observations, it is possible that edge effects may not be the only mechanism for the measured anomalous behavior.

Once again the beam size was estimated using the convolution method described in the edge excited beam profile measurements, resulting in a beam diameter of approximately 5.5 mm that matches the predicted beam profile on the TIR interface from the characterization measurements in Chapter 5.

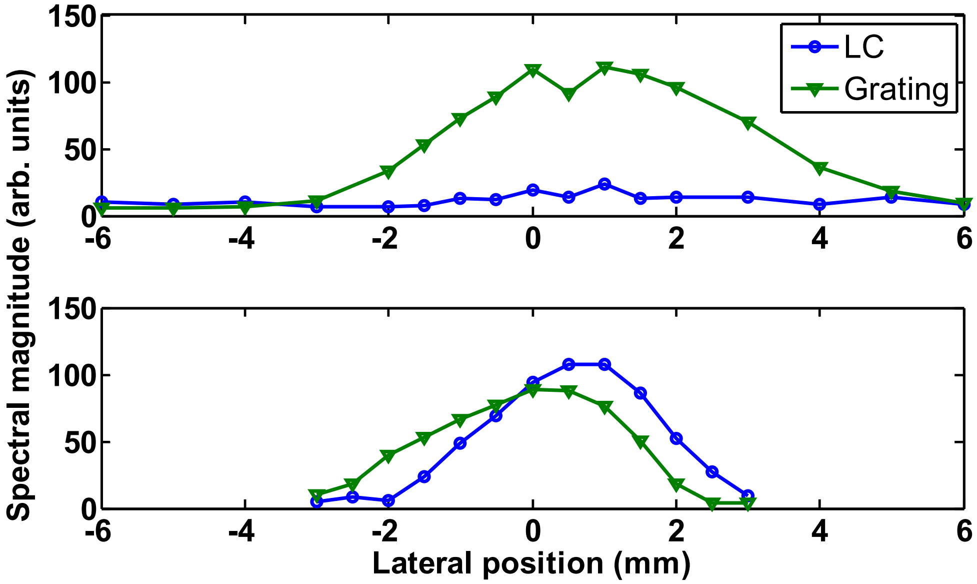

Figure 6-23: Near center (top panel same as Figure 6-22) and near edge (bottom panel same as Figure 6-21) excited beam profile measurements from re-radiation waveforms shown here for fundamental *LC* (blue) and the transmission grating (green) frequencies. Positive offset is towards the edge and negative offsets are toward the center of the array.

.

The results of the lateral offset measurements from Figure 6-21 and Figure 6-22 are compared in Figure 6-23. The experimental results are plotted on the same x-axis scale for clarity. Comparing the response from the edge with the response from 5 mm into the array (near center- excited), the grating transmission decreases in size when near the edge of the array. The measurements validate that the re-radiation is predominately from a spatially localized source corresponding to the excitation of the array edge.

Additional information can be obtained from examining the time envelope of the grating waveform. The grating response from the lateral displacement re-radiation measurement is shown in Figure 6-24 (a).

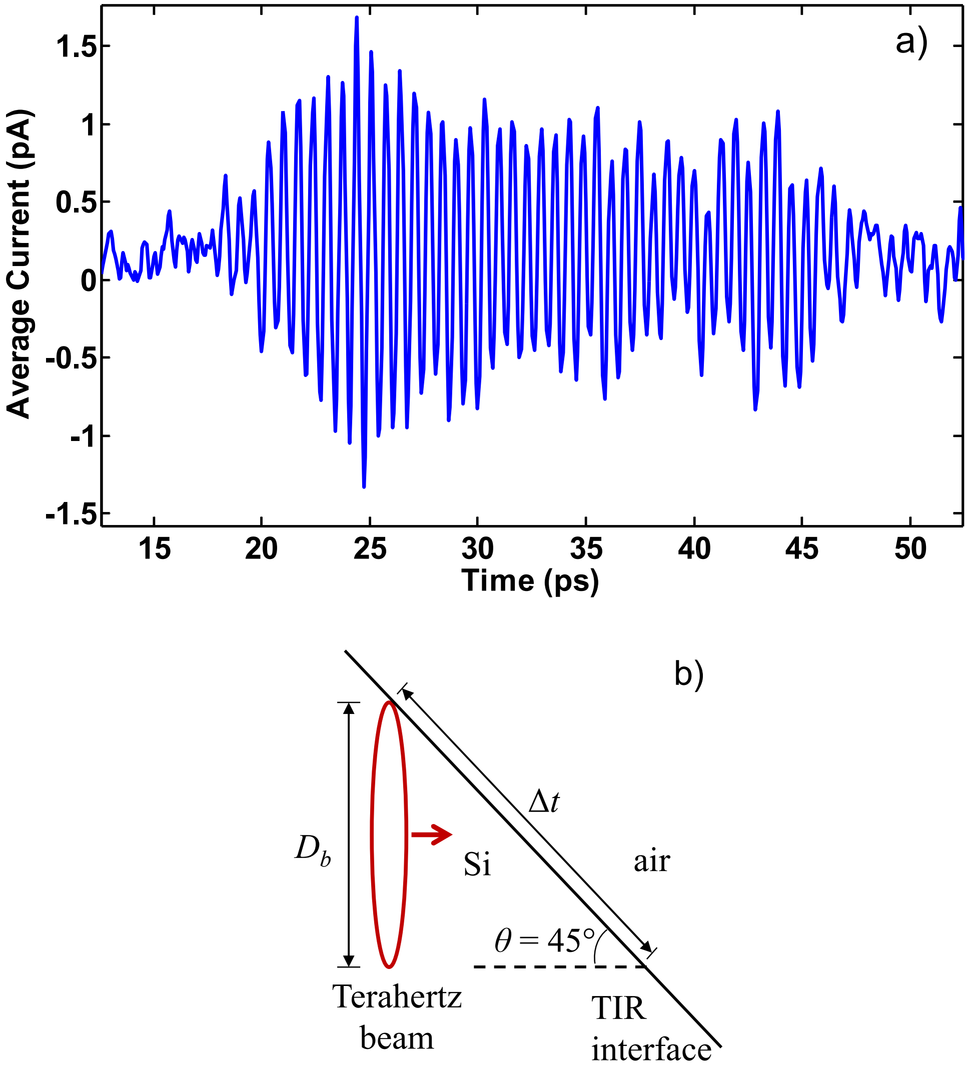

Figure 6-24 a) Transmission grating response from near center excited SRR array in the time domain b) Beam width calculation geometry.

The terahertz beam is incident near the center of the SRR array. The beam diameter D_b can be calculated as

$$D_b = \frac{c\Delta t}{n\sin\theta_i} \tag{6.4}$$

where c is the speed of light in vacuum, n is the index of the substrate, in this case n =3.42 for Si, Δt is the duration of the grating transmission and θ_i is the angle of incidence. This time envelope is a measure of how long the incident pulse interacts with the array. The transmission grating wavepacket roughly extends from 17 ps to 47 ps, making Δt = 30 ps. For θ_i = 45°, the beam diameter x was calculated to be 3.7 mm. The beam width of the THz field striking the TIR surface from the Si side is $\frac{3.7\text{ mm}}{\sin 45} = 5.2\text{ mm}$. The estimated beam width from this measurement is in close agreement with the estimates of the beam sizes obtained from measurements discussed in the previous section and in Chapter 5.

6.3.2 Directionality of the radiation signal-Angular dependence

If the re-radiation is localized to the edge of the array it would give rise to a radiation pattern similar to a line source emitting cylindrical waves. To measure the angular dependence of terahertz radiation emitted from the excited metamaterial, the receiver was rotated over a range of 0 to 65° from θ = 45° in steps of 5°, ensuring that the axis of rotation is at the prism surface. The rotation stage physically limits the available angles for rotation in the negative direction from the normal to the sample (see Figure 6-4). For each detection angle θ, the prism was rotated such that the terahertz beam entered the prism normally so the end result was the receiver arm changed angle and all other components were fixed. A series of waveforms was measured at different angular positions of the receiver relative to the position of the prism.

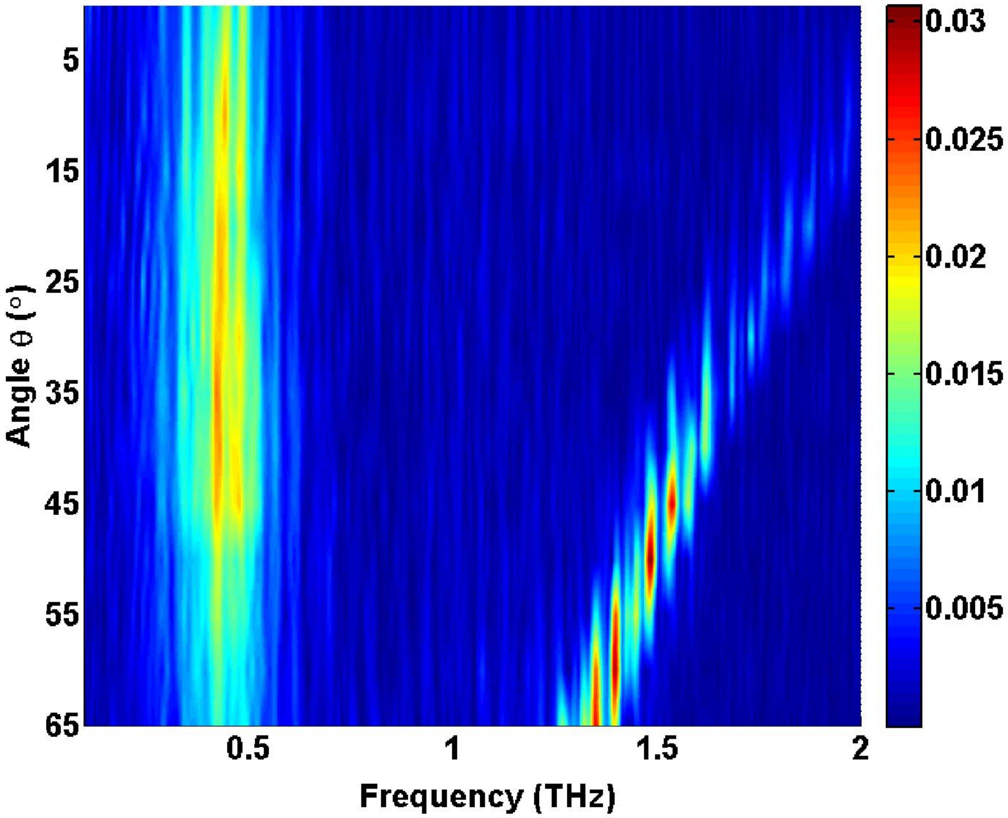

Figure 6-25: Angularly resolved spectra for radiation measurements from 0 to 65° from prism normal showing *LC* radiation and transmission grating signals.

Figure 6-25 shows the Fourier transformed normalized spectra of these re-radiated terahertz pulses as a function of receiver angle. The radiation spectra centered at 0.44 THz was essentially unchanged for a large range of angles 0 to 40° from the optical axis indicating that the signal possibly radiated preferentially from the edge of the array. The radiated signal seems to be isotropic in the plane of measurement which is consistent with a line source oriented out of the plane of incidence. The radiation spectrum is comprised of a low frequency *LC* resonance component near 0.44 THz and high frequency components around 1.5 THz. The higher order grating resonance changes with the detection angle, in accordance with the transmission grating equation. Other measurements on smaller SRR arrays showcased earlier in the chapter depict similar behavior further corroborating the isotropic *LC* re-radiation.

6.3.3 Effect of polarization on the radiation signal

Incident s-polarized field

To characterize the polarization of the re-radiation signal, additional measurements were performed using sample MM1 as it gave the most interesting response. The SRR gap was oriented both parallel and perpendicular to the incident s-polarized electric field E_{in} using a polarization sensitive receiver. Only the linear component of the electric field is measureable. The polarization of the incident field is important for excitation of the *LC* resonance in a SRR with broken symmetry; such that electric field polarized parallel to the gap bearing arm can induce a circulating current while the electric field along the non-gap bearing arm excites only a dipole mode [83] as discussed in Chapter 4. On the other hand a magnetic field perpendicular to the plane of SRR can also excite the *LC* resonance by inducing a circulating current which can occur while undergoing TIR. The polarization sensitive re-radiation response E_{meas} shown in Figure 6-26 were measured with two different SRR gap orientations and two different receiver polarizations (s and p). The results are normalized to the bare prism ATR spectrum. In addition, the ATR spectra are shown in Figure 6-27 for the corresponding excitation and measurement scenarios. The ATR measurements were all taken when the incident beam excited the edge of the SRR array to ensure the anomalous edge effect was observed assuming that re-radiation would occur.

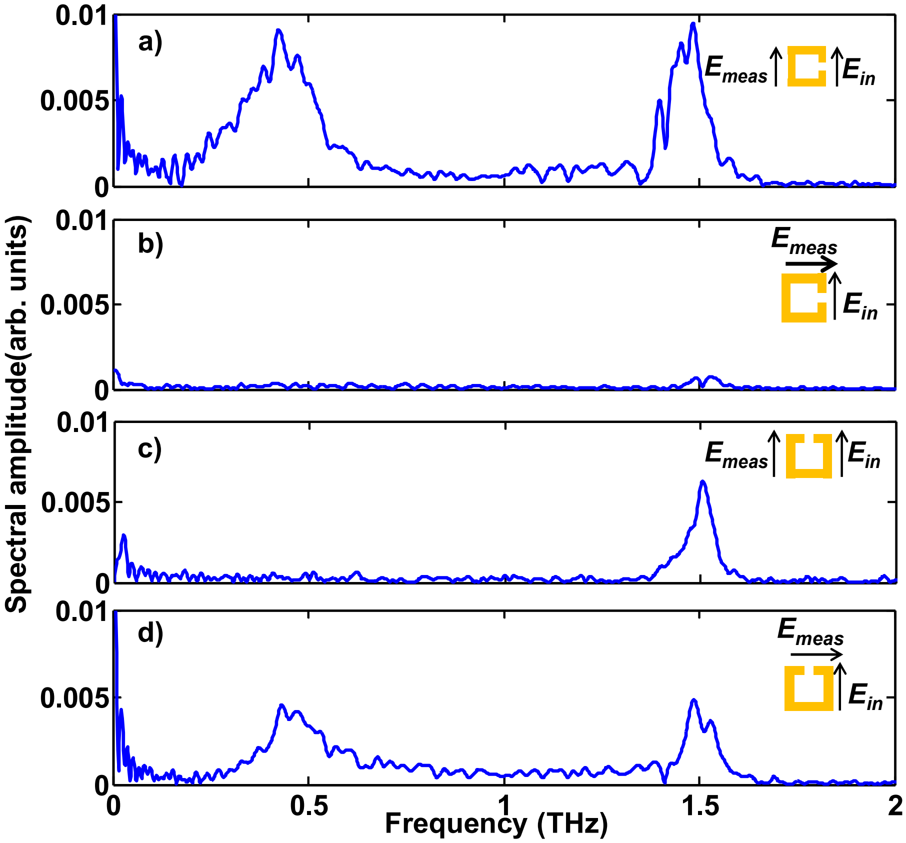

Figure 6-26: Re-radiation spectra for different orientations of the SRR and detector. Incident field is s-polarized.

For the radiation spectra in Figure 6-26 a), the THz emitter and detector are both s –polarized and oriented parallel to the SRR gap. The incident EM field has an electric field component parallel to the gap and a magnetic field vector component perpendicular to the plane of the SRRs while undergoing reflection. The incident EM field induces a circulating current which then re-radiates into the *LC* resonance. Both E and H fields drive the fundamental *LC* resonance near 0.44 THz. Due to the broken asymmetry of the SRR, there is an imbalance in the current from the gap bearing arms and that of arm opposite to the gap. The net current contributes to the *LC* resonance radiation. The contribution from the dipole mode, even if present is not detected. This is the standard transmitter and receiver polarization orientation that was used for the majority of the fundamental investigation of this re-radiation phenomenon. The re-radiation response shown in Figure 6-26a) and the ATR response shown in Figure 6-27a) are results shown previously in this chapter.

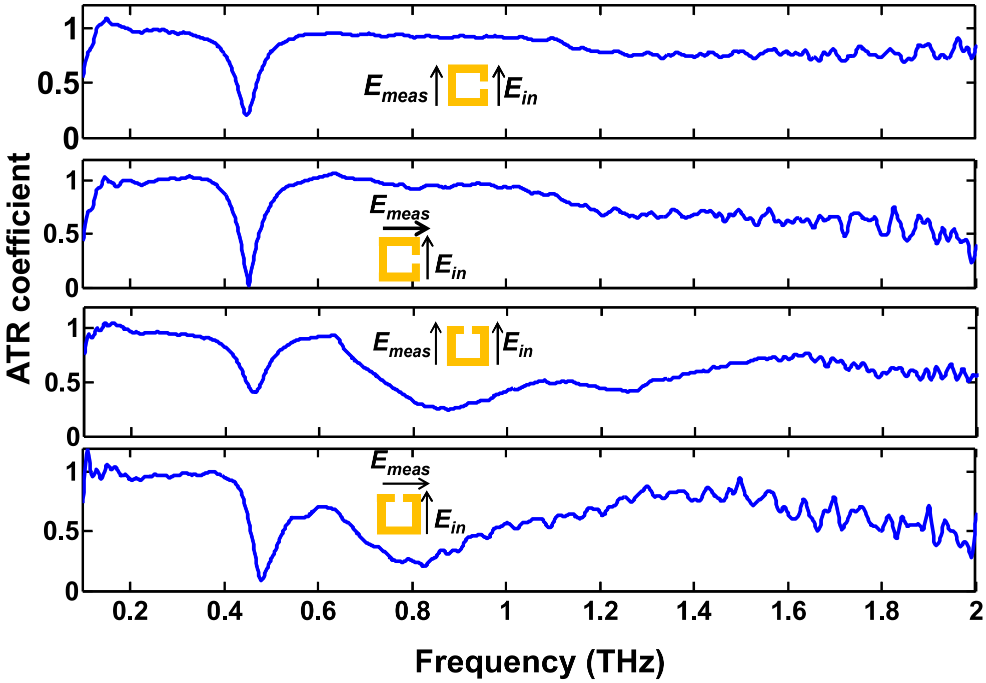

Figure 6-27 ATR spectra for different orientations of the SRR and detector. Incident field is s-polarized.

For the measurement in Figure 6-26 (b), the SRR array was oriented with the *E*-field along the gap bearing arm. In order to rotate the receiver by 90° with respect to the transmitter to detect p-polarized radiation, the following alignment procedure was followed. This measurement was performed by placing a wire grid polarizer rotated to 45° in front of the s-polarized terahertz detector. The terahertz signal is maximized to ~

$\frac{1}{\sqrt{2}}$ of the peak amplitude of the previously co-polarized signal. The receiver was rotated by 90° with respect to the transmitter to detect p-polarized radiation. The signal was once again optimized to the previously maximized $\frac{1}{\sqrt{2}}$ of the peak amplitude because the receiver antenna may not be precisely on the axis of rotation for the FRU. The ATR measurement as shown in Figure 6-27 b) shows a strong *LC* resonance. This is because a 45° polarizer was still in place in front of the receiver to observe both s and p contributions.

The polarizer was removed. The receiver arm was rotated to $\theta = 45°$ and the cross-polarized re-radiation signal was detected. Figure 6-26 (b) depicts the scenario where no radiated field is detected by the p-polarized receiver, as expected, for both the *LC* resonance and the grating transmission. There are some weak features at higher frequencies near the grating transmission which may be due to possible misalignment between the terahertz transmitter and receiver or imperfect polarization sensitivity.

For the measurement shown in Figure 6-26 (c), the SRR array was oriented with the *E*-field along the non-gap bearing arm. Thus the *E*-field fails to induce a circulating current in the SRR. The *LC* resonance should be excited due to the incident magnetic field but it is not detected due to the orientation of the receiver. When the receiver is polarized perpendicular to the gap, it cannot measure the radiation from the two equal arms in the *LC* mode. Only the grating resonance is visible in this scenario. A very strong first order electric dipole mode is present in the ATR measurement [Figure 6-27 c)] corresponding to this orientation. The *LC* resonance is strongly observed which demonstrates that the magnetic field undergoing TIR can excite the mode.

Lastly, both the receiver and the SRRs were rotated for the case of Figure 6-26 (d). The *LC* resonance is clearly distinguishable above the background noise. The dominant mechanism for this radiation is likely caused by the excitation due to the magnetic field only which induces circulating currents. The incident field is s-polarized. So the re-radiation is rotated 90° with respect to the incident field due to the capacitive gap providing the linearly polarized re-radiation mechanism via bianistropy. Therefore the response at the receiver is cross-polarized (p-polarized). Comparing the transmission grating response in Figure 6-26 b) The ATR spectrum in Figure 6-27 d) shows the same response as c).

For all cases in Figure 6-26, the re-radiation measurements were averaged 16 times with a 300ms time constant.

The characterization of the behavior of MM is seen to rely on excitation, resonances, and detection. This implies that the reflected or transmitted responses may be simply outside the scope of the measurement and must be taken into account. The ATR configuration additionally allows us access to multiple modes for excitation and detection that are not readily available in a single standard TDS transmission experiment with a planar metafilm.

Incident p-polarized field

Identical measurements were performed using p-polarized incident EM field. Figure 6-28 a)-d) reveal the effect of p-polarized THz field on the SRRs with fields oriented parallel and perpendicular to the capacitive gap and for different SRR orientations.

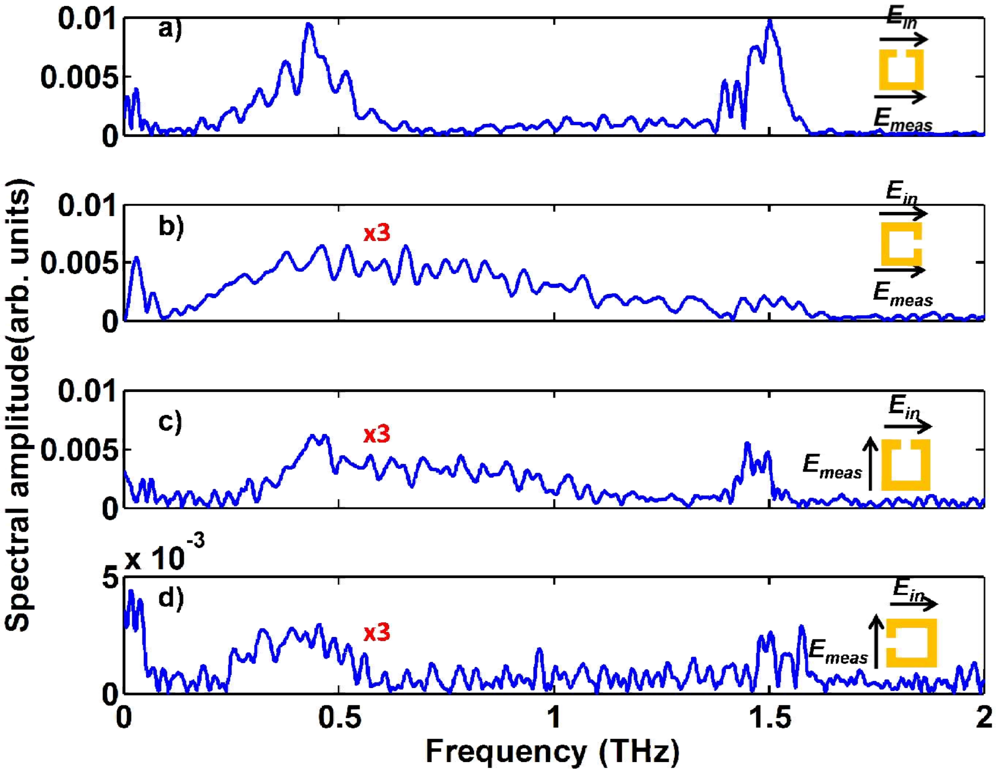

Figure 6-28 Re-radiation spectra for different orientations of the SRR and detector. Incident field is p-polarized.

For cases a)-d), the magnetic component of the incident field lies along the plane of the SRRs and as a result, does not contribute to exciting the fundamental *LC* current mode. Hence the expected excitation mechanism resulting in re-radiation is only due to the electric field as seen in Figure 6-28(a). Extremely weak *LC* resonance in Figure 6-28(d) is observed which is possibly due to the substrate induced bianisotropy [24]. Currently, the reason for the broadband signatures although extremely weak seen in

Figure 6-28 (b) and c) are not clear. This may possibly be due to diffraction at the edge of the SRR array.

6.3.4 Re-radiation from MM2 and MM3

Re-radiation measurements were also attempted on the metafilms MM2 and MM3, despite not observing a strong edge enhancement in them.

6.3.4.1 MM2

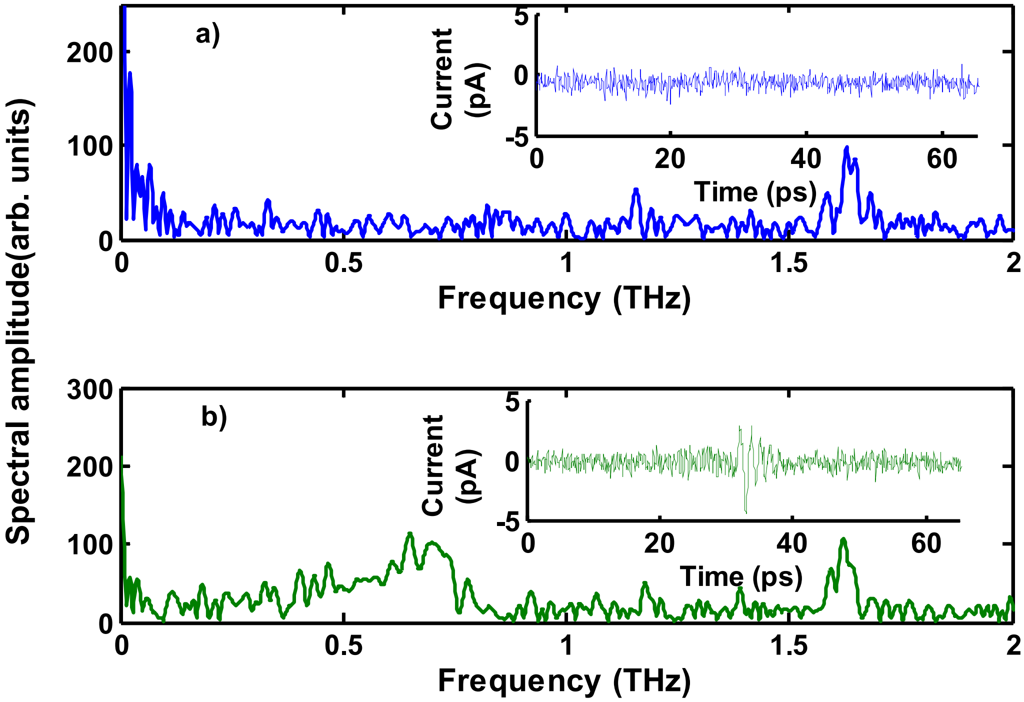

Figure 6-29 Re-radiation measurements on MM2 measured normal to the prism face with inset showing time domain signal. Incident beam a) near the center of the array and b) near the array edge.

Re-radiation was detected when the terahertz beam was focused at the edge of the metafilm MM2. As seen from Figure 6-29, the relative magnitude of the measured signal was significantly weaker than that from MM1. There was no detectable radiation when the focus position was the center of the MM2 array.

6.3.4.2 MM3

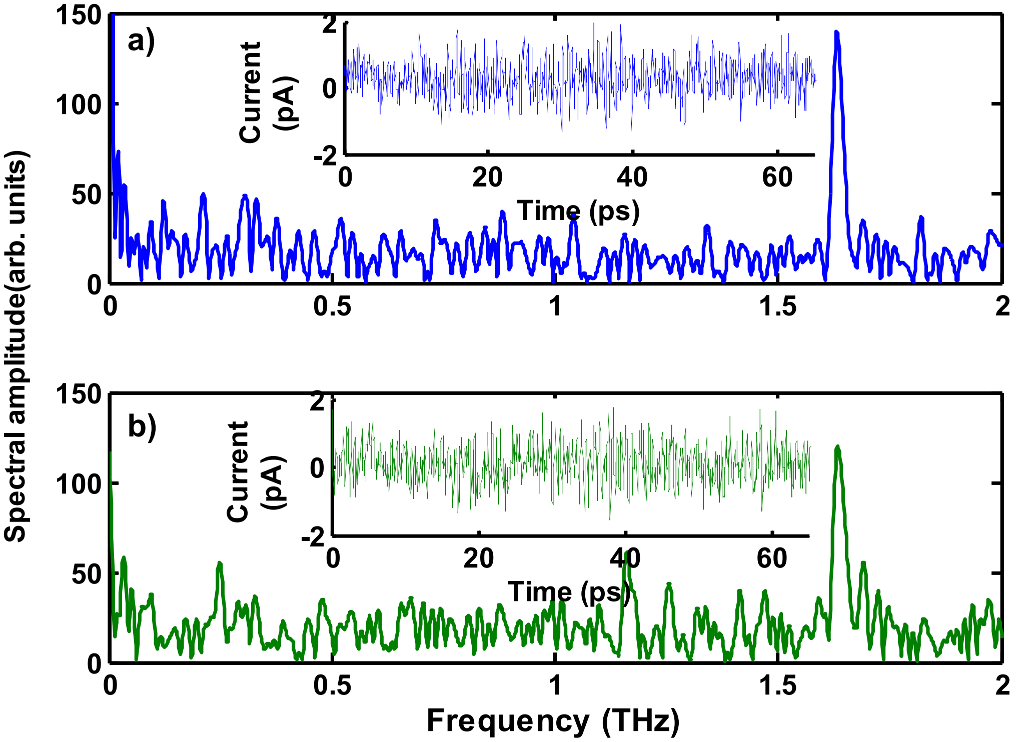

Figure 6-30 Re-radiation measurements on MM3 measured normal to the prism face with inset showing time domain signal. Incident beam near a) the center of the array and b) the array edge.

For completeness, despite the weak re-radiation detected in MM2, these measurements were performed on sample MM3. This is shown in Figure 6-30. Re-radiation was absent or below the detection threshold in the metafilm array MM3.

6.4 *Experimental Summaries*

The experimental results can be summarized as follows.

1. Trends observed from the measured ATR responses from metafilms MM1, MM2 and MM3 differ from those obtained from direct THz-TDS transmission measurements at normal incidence. Sample MM1 shows a sharp drop in the reflection coefficient when the incident THz beam illuminates the sample near the edge. MM2 exhibits this feature weakly and MM3 does not exhibit this feature at all.
2. The large SRR array MM1 shows re-radiation from the TIR surface over a range of angles with the largest amplitude at/near the normal to the plane of the metafilm. This re-radiation shows a lower order mode corresponding to the fundamental resonance of the SRRs and a higher order transmission grating mode. Additionally, MM2 also exhibited weak re-radiation.
3. There is an apparent correlation between the anomalous edge enhancement observed in ATR and the re-radiation signal strength. Re-radiation is strongest at the array edge which could be due to possible launch of surface mode, even when excitation is away from the edge.
4. The re-radiation signal seems to be predominately in line with a line source localized near the array edge.

Attempts to explain these observations are dealt with in the following chapter.

7 Theoretical models

In this chapter, the theories to explain the re-radiation signal that is localized at the edge of the metafilms are discussed. To sum up previous results, re-radiation was observed in MM1 but the response was greatly reduced in the metafilm sample MM2 and not observed in MM3. Experimental results reveal an anomalous increase in the resonance strength in the ATR reflection while the sample is illuminated near the edge of the metamaterial array with a finite size terahertz beam.

Edge effects play a dominant role in the re-radiation mechanism, but this does not eliminate the possibility of a surface wave carrying energy to the edge of the MM array. Surface waves are the transfer of energy that can exist at the interface of two media. Surface waves on metamaterial arrays may develop based on the exchange of EM energy between adjacent SRRs. Surface waves, if they exist, could be a loss mechanism that is radiatively coupled to free space when reaching the boundary of the metafilm array. This could be interpreted as anomalous enhancement of the resonance in ATR but are measured as "re-radiation". The exact nature of the re-radiation mechanism is not obvious from the experimental results.

Following are the approaches taken in this chapter to demystify the re-radiation signal.

1. Study of the inductive coupling between SRRs using CST microwave studio
2. Analysis based on the transmission line *RLC* circuit model.

3. Finite Difference Time Domain using Lumerical 3D
4. Floquet approach
5. Surface wave analysis
6. Method of moments approach

7.1 Surface waves and Finite arrays

Surface wave studies propagating along finite antenna arrays have demonstrated non-homogenous behavior. For example, surface waves that occur below resonance on truncated periodic arrays have been examined using a Method of Moments approach. It was shown that large surface wave currents could exist on truncated arrays in addition to the Floquet currents seen in infinite periodic arrays [97]. These currents were found to be due to travelling waves arising from the left and the right edges of the array. Scattering in finite arrays also include reflections or end currents from the right and the left edges of the array [98]. The edge currents of a finite array of dipoles differ from those located towards the center, although the edge current radiation is typically at a lower frequency (~20%) than the resonance of the dipoles [99]. Robertson *et al*. studied surface waves on truncated frequency selective surfaces and found similar effects on loop resonator arrays, except that the edge current radiation was at the same resonant frequency as the infinite array[100]. These surface waves, regardless of coupling mechanism, will propagate to the edge of the finite array and re-radiate because of the impedance mismatch at the sample boundary.

A type of surface wave called magneto-inductive (MI) surface wave that arises due to the coupling between magnetic metamaterial elements is also known to occur on patterned structures capable of supporting a magnetic dipole moment [101]. The magneto-inductive (MI) wave that is present due to the inductive coupling in these resonators is also referred to as a magnetization wave [102, 103]. MI waves were characterized on transversely and longitudinally oriented SRR arrays in the GHz region [105]. MI waves in the terahertz regime were inferred from transmission measurements on metasurfaces using THz-TDS at oblique incidence[104]. Studies show the existence of these MI waves in chains of nano-particles in the far infra-red [104].

There are no metamaterial samples that are infinite in size. This is an important problem to investigate, because every sample will have edges regardless of the beam size. Finite arrays obviously exhibit different effects when a finite excitation wave overlaps the edge of the array.

7.2 CST microwave studio investigation of Magneto-inductive (MI) waves

An effort to identify potential surface wave mechanism responsible for bringing energy to the edge is described using a commercial finite integration solver CST Microwave Studio. Effective medium approaches ignore the effect of these localized near-field interactions occurring between elements.

To investigate whether MI waves were dominant in the samples used in this work, finite integration simulations using CST Microwave Studio were performed. CST is commonly used to perform simulations of MMs. A line of SRRs was simulated in a virtual waveguide using perfect electric conductor (PEC) and perfect magnetic conductor (PMC) boundaries. This is a common technique in MM simulations to make the model computationally tractable and to approximate an infinite array. The structure consisted of a single row of 25 split ring resonators with unit cell sizes of 80 μm on a high resistive silicon substrate as shown in Figure 7-1.

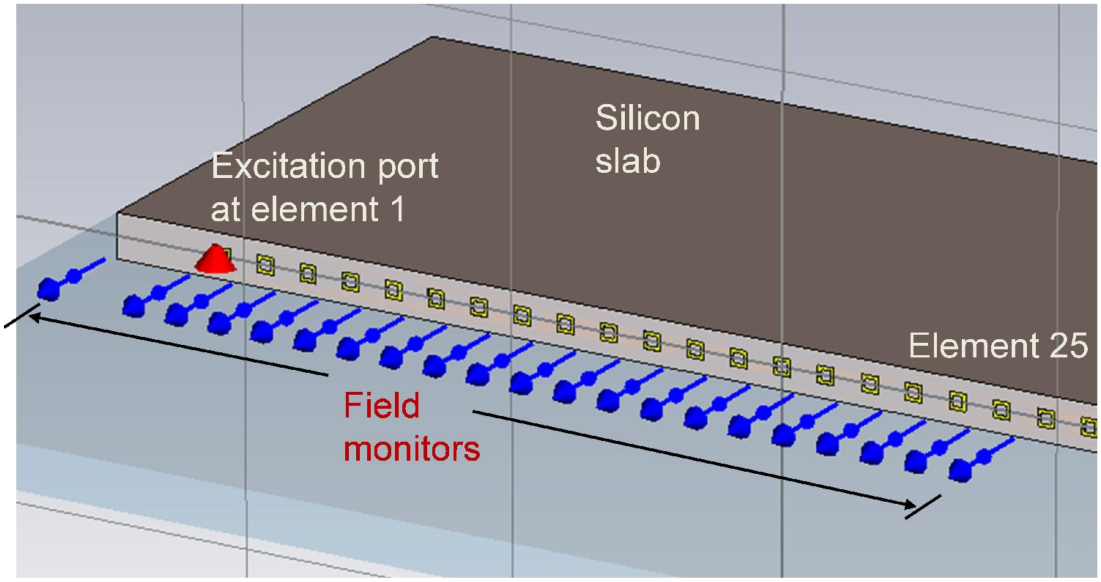

Figure 7-1: CST microwave studio simulation setup to observe inductive coupling between nearest neighbors.

A single resonator has dimensions same as MM1 and therefore resonates at 0.44 THz. Element 1 was directly excited by the introduction of a field port across the gap and the effect of the inductive coupling on the resonating elements located away from element 1 was studied. The excitation was broadband between 0.1 THz and 2 THz. Numerical studies were also performed on MM2 and MM3 sample geometries with 25 resonators. The on-resonance magnetic field generated by the circulating currents at normal incidence was investigated.

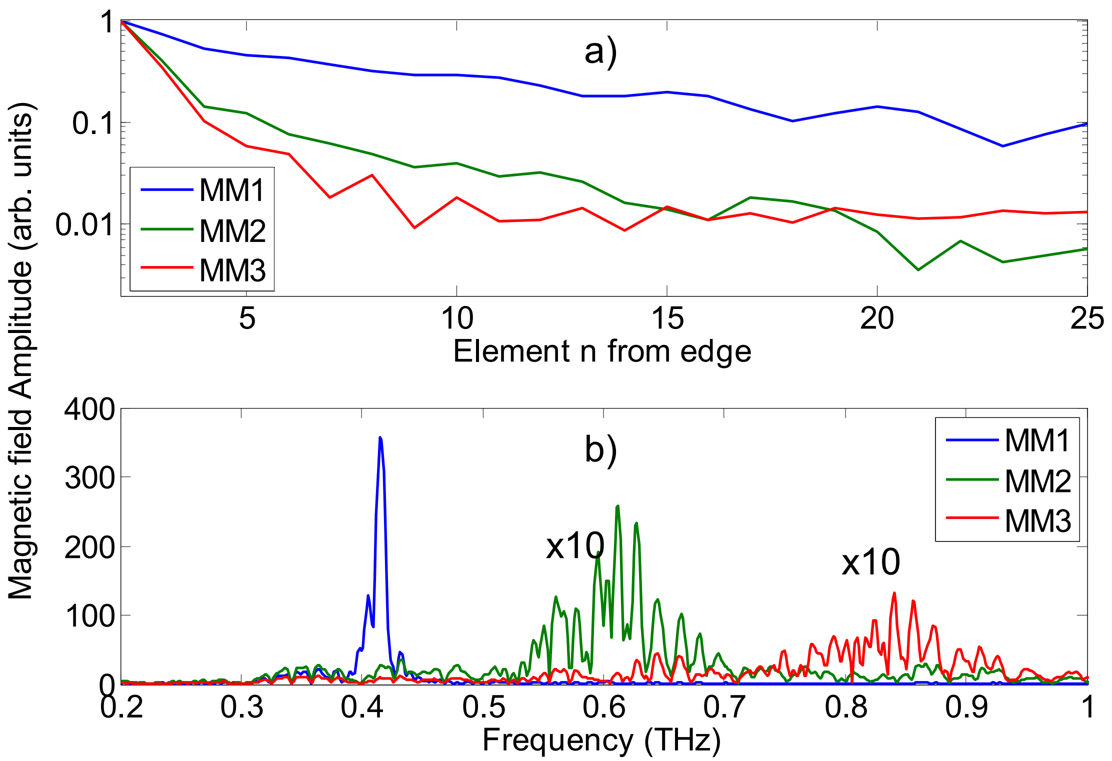

Figure 7-2 Simulation results from CST microwave studio. a) Top panel: Normalized magnetic field strength as function of element position b) Bottom panel: Magnetic field strength as a function of frequency at furthest monitored element (25).

The peak amplitude of the magnetic field strength as a function of element position from the edge is plotted Figure 7-2 a). For clarity, the field in element 1 is not included. The coupling effect is noticeably higher for the case of MM1 by an order of magnitude. This indicates strong coupling for sample MM1 thus implying that energy can be carried away from the excitation point through inductive coupling. Since the unit cell is maintained at 100 µm for all 3 samples, the effect is significantly weaker for samples MM2 and MM3 matching experimental observations. This can be additionally seen in Figure 7-2 b) where the frequency dependence of the inductively coupled effect on element 25 for samples MM1, MM2 and MM3 is plotted. Element 25 is 2.5 mm from the excitation which is on the order of the beam radius.

CST software does not handle complex excitations and non-standard geometries such as the ATR work presented here directly in time domain analysis. But the results yield insight into the inter-element coupling which gets weaker as the distance relative to resonant wavelength between the SRRs increases. It is difficult to isolate specific mechanisms responsible for behavior of interest in full wave simulations.

In response to the limitations of the CST simulation, a simple analytic approach employing transmission line theory was undertaken.

7.3 RLC-TL model

Due to the sub-wavelength nature of the SRRs, the effective medium approximation is a commonly applied approach for extracting the constitutive parameters of a metamaterial in terms of bulk parameters $\mu(\omega)$ and $\varepsilon(\omega)$. In case of very thin films of planar metamaterials such as metafilms, it becomes hard to assign an effective thickness giving rise to artifacts in the calculations. A lumped circuit model in conjunction with a transmission line model provides a relatively simple means for describing 2D planar metamaterials [105, 106]. This model can be easily translated to a stratified model which is convenient for describing several layers of stacked metafilms. An analytical solution which uses the transmission line *RLC* circuit model has been developed by Shamonina *et al*. [101]. Additionally, it is advantageous in comparing with simulations since the expressions for the transmitted and reflected fields can be easily compared with scattering and transfer matrices. However this model does not sufficiently capture the mechanisms responsible for the re-radiation.

7.3.1 Transmission line model for standard THz TDS

As described previously in Chapter 6, the three MF arrays were characterized in a standard transmission Terahertz TDS experiment in addition to ATR measurements.

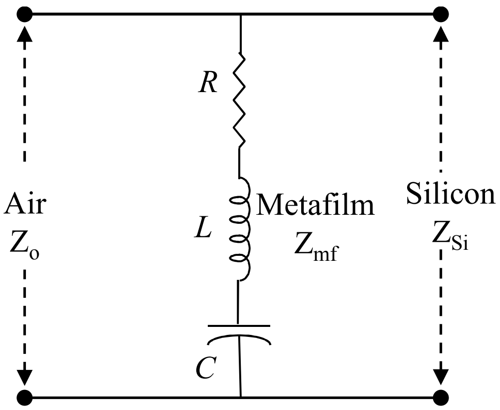

Figure 7-3 Equivalent circuit for metafilm on Silicon substrate

To match the experimental arrangement, the metafilm is modeled as an equivalent lumped *RLC* circuit element that couples to the transmission lines of air and silicon substrate on opposite sides and this is illustrated in Figure 7-3. This model uses basic circuit theory to find the modified complex boundary impedance for the metafilm sandwiched between silicon and air. The transmission lines of silicon and air have characteristic impedances Z_{si} and Z_0 respectively. The frequency dependent complex transmission is obtained by the ratio of the Fourier transformed sample and reference time domain signals, $\tilde{t}(\omega) = \dfrac{E_{sam}(\omega)}{E_{ref}(\omega)}$ with the reference being a bare silicon substrate of equal thickness. Using analogous Fresnel amplitude transmission coefficients at the front and back interfaces of the sample, the measured transmitted electric field through the bare substrate [106], is given by

$$E_{ref}(\omega) = E_i \frac{2Z_{Si}}{Z_{Si} + Z_0} \frac{2Z_0}{Z_{Si} + Z_0} \tag{7.1}$$

Similarly, the transmitted electric field through the sample is expressed as

$$E_{sam}(\omega) = E_i \frac{2Z_{mf} \parallel Z_{Si}}{Z_{mf} \parallel Z_{Si} + Z_0} \frac{2Z_0}{Z_{Si} + Z_0} \tag{7.2}$$

The complex transmission coefficient can then be written as

$$\tilde{t}(\omega) = \frac{Z_{mf} \parallel Z_{Si}}{Z_{mf} \parallel Z_{Si} + Z_0} \frac{Z_{Si} + Z_0}{Z_{Si}} \tag{7.3}$$

The magnitude of the above complex transmission is compared with the transmission measurements. The complex impedance of the metafilm follows standard expressions from circuit theory for a series *RLC* circuit and is given by

$$Z_{mf}(\omega) = R + j\omega L + \frac{1}{j\omega C} \tag{7.4}$$

The values for *R*, *L* and *C* are then manually adjusted to match the data. The resonant frequency of the metafilm unit cell relates the *L* and *C* by the relation $\omega = {1}/{\sqrt{LC}}$ and the quality factor for a series *RLC* circuit is given by $Q = {1}/{R\sqrt{LC}}$. The two relations impose restrictions to the range of permissible values. Table 3 gives the fitted circuit parameters to match the measured transmission THz-TDS data with the model for the metafilms MM1, MM2 and MM3.

Sample	R (Ω)	L (pH)	C (fF)
MM1	42.5	281.9	0.4
MM2	50.4	315.4	0.17
MM3	64.0	290.05	0.11

Table 3 Extracted lumped circuit values for transmission measurements.

Keeping all other parameters fixed the extracted values for the resistance *R* increase linearly with an increase in the SRR size. The extracted capacitance is inversely proportional to the size of the SRR. The inductance *L* in Table 3 does not show a clear trend. This is likely due to the interplay of mutual and self-inductances as a function of element separation.

Based on the above values, Figure 7-4,Figure 7-5 and Figure 7-6 show the comparison between the measured transmission data and the calculated transmission coefficient from the *RLC*-TL model for metafilms MM1, MM2 and MM3 respectively.

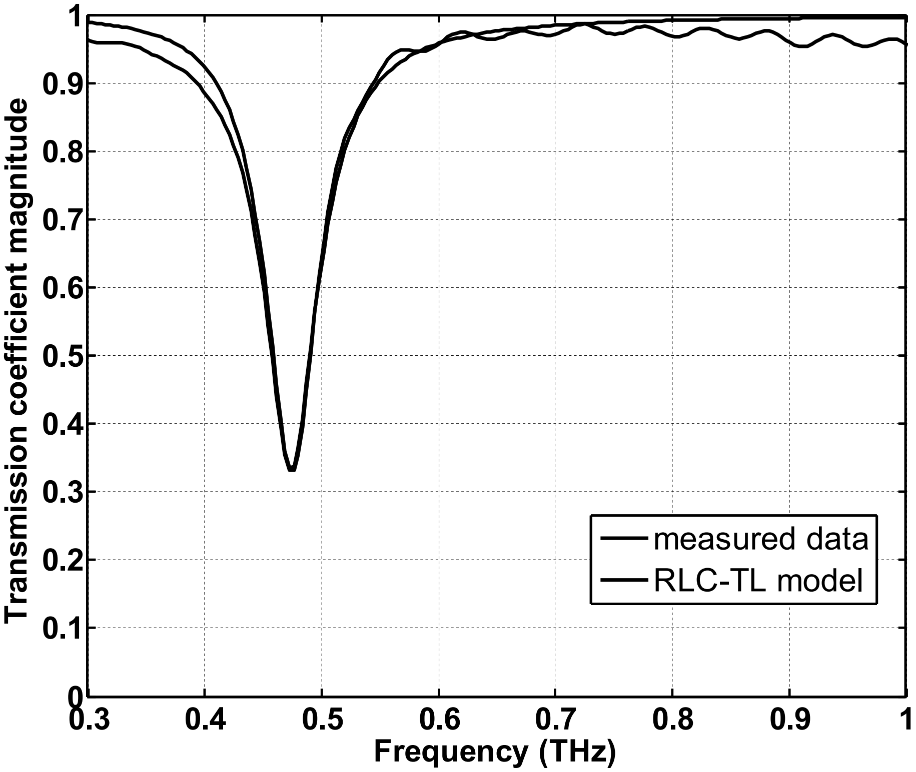

Figure 7-4 Transmission coefficient for metafilm MM1 from measurements (solid) and *RLC*-TL circuit model (dashed).

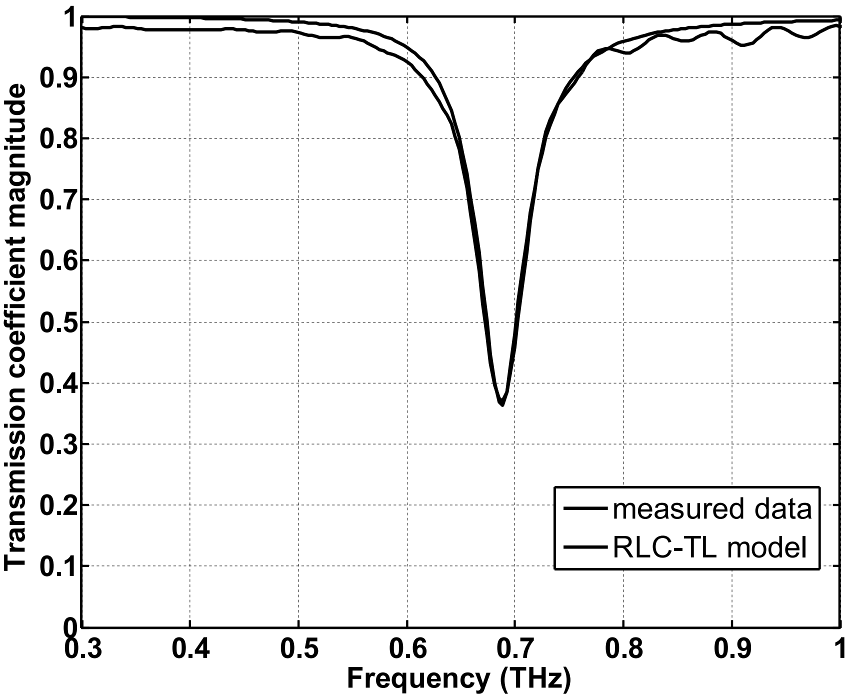

Figure 7-5 Transmission coefficient for metafilm MM2 from measurements (solid) and *RLC*-TL circuit model (dashed).

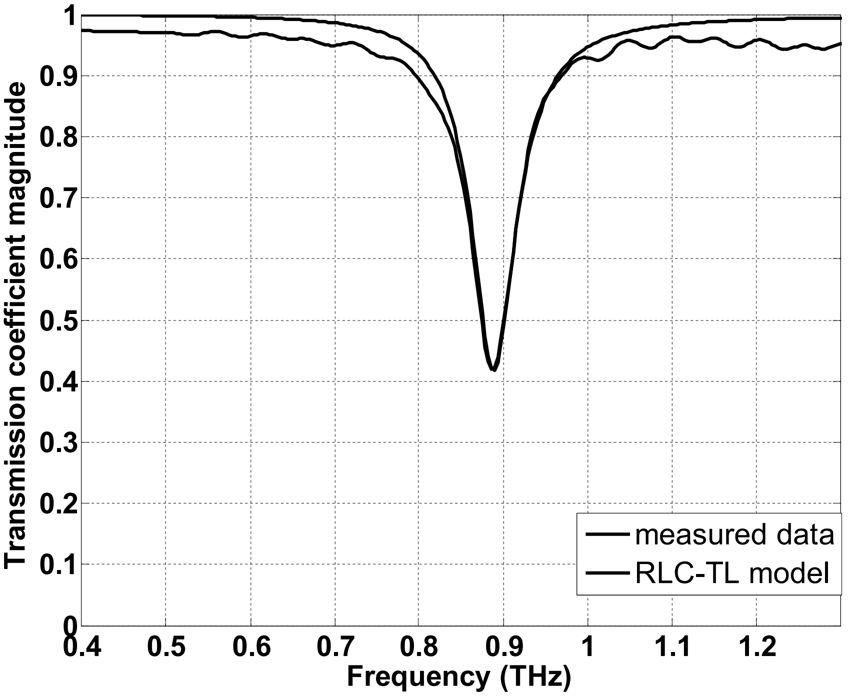

Figure 7-6 Transmission coefficient for metafilm MM3 from measurements (solid) and *RLC*-TL circuit model (dashed).

7.3.2 Transmission line model for THz-ATR transmission

The stratified *RLC*-TL circuit model is adapted to ATR measurements based on the approach discussed previously under transmission measurements. This model is slightly modified to mimic the conditions for oblique incidence, specifically total internal reflection phase shift as determined from Fresnel reflection coefficients using the ATR geometry. The values of the metafilm are adjusted manually to match the calculated reflection coefficient with the measured ATR data.

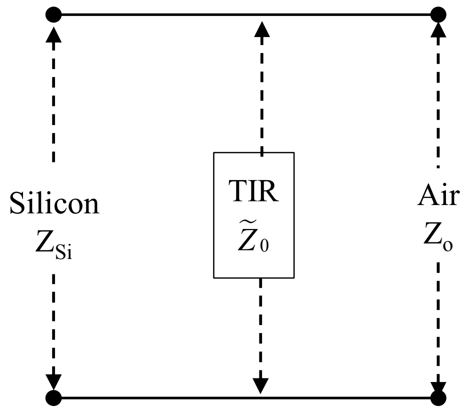

Figure 7-7 Circuit model for the ATR configuration at the silicon-air TIR boundary.

For the circuit model equivalent for the reference measurement shown in Figure 7-7, with only the silicon prism and in the absence of a metafilm on its surface, additional impedance namely $\tilde{Z}_0$ is introduced at the silicon-air boundary to account for non-zero angles of incidence. Typically, for normal incidence $\theta_i = 0°$, the characteristic impedance of the rarer medium in this case air, is 377 Ω. But when the angle of incidence goes beyond critical angle, the reflection coefficient becomes complex and the surface impedance is modified. Therefore $\tilde{Z}_0$ is the effective impedance for the TIR interface without a metafilm and is angle dependent. Assuming a frequency independent refractive index for silicon, Fresnel reflection coefficient from silicon to air with angle of incidence $\theta_i = 45°$ for perpendicular polarization is

$$\Gamma_{ATR}^{ref} = \frac{n_2 \cos\theta_i - n_1 \cos\theta_t}{n_2 \cos\theta_i + n_1 \cos\theta_t} \tag{7.5}$$

The reflection coefficient is also expressed using a parallel combination of $Z_{Si} \,||\, \tilde{Z}_0 \,||\, Z_0$ from Figure 7-7 and is equal to

$$\frac{\tilde{Z}_0 \,||\, Z_0 - Z_{Si}}{\tilde{Z}_0 \,||\, Z_0 + Z_{Si}} = 0.0935 - i0.9956 \tag{7.6}$$

Solving for $\tilde{Z}_0$, $\tilde{Z}_0 = \left(-35.2 - j109.75\right)\Omega$.

The measured field from the silicon-air interface is given by

$$E_{ATR}^{ref}(\omega) = E_i(\omega)\Gamma_{ATR}^{ref} = E_i(\omega)\frac{\tilde{Z}_0 \,||\, Z_0 - Z_{Si}}{\tilde{Z}_0 \,||\, Z_0 + Z_{Si}} \tag{7.7}$$

whereas in the presence of a metafilm at the silicon-air boundary, the measured field in an ATR configuration (see Figure 7-8 below) is

$$E_{ATR}^{sam}(\omega) = E_i(\omega)\Gamma_{ATR}^{sam} = E_i(\omega)\frac{Z_{surf} \,||\, Z_0 - Z_{Si}}{Z_{surf} \,||\, Z_0 + Z_{Si}} \tag{7.8}$$

Here the effective surface impedance modified by a metafilm is defined as

$$Z_{surf} = Z_{mf} \,||\, \tilde{Z}_0 = \frac{Z_{mf}\tilde{Z}_0}{Z_{mf} + \tilde{Z}_0} \tag{7.9}$$

and as before the lumped *RLC* element is expressed as

$$Z_{mf} = R + j\omega L + \frac{1}{j\omega C} \tag{7.10}$$

Therefore the ATR coefficient becomes

$$\Gamma_{ATR} = \left(\frac{Z_{surf} \parallel Z_0 - Z_{Si}}{Z_{surf} \parallel Z_0 + Z_{Si}} \right) \left(\frac{\tilde{Z}_0 \parallel Z_0 + Z_{Si}}{\tilde{Z}_0 \parallel Z_0 - Z_{Si}} \right) \tag{7.11}$$

This expression for the reflection coefficient is used to match the measured ATR transfer function $\frac{E_{ATR}^{sam}(\omega)}{E_{ATR}^{ref}(\omega)}$ by manually choosing values for R, L and C of the metafilm along with the constraints of $\omega = 1/\sqrt{LC}$ and $Q = 1/R\sqrt{LC}$

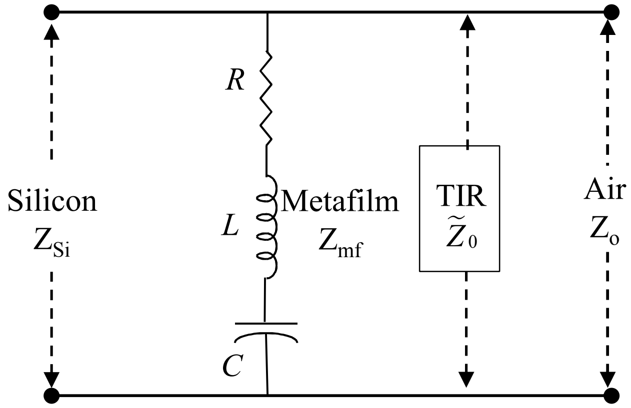

Figure 7-8 Equivalent circuit model for ATR configuration: metafilm on silicon prism.

This treatment assumes that the high resistivity silicon prism is continuous with the high resistivity silicon substrate on which the sample is fabricated and that there is no air gap between the silicon prism and the silicon substrate. Using this above approach, Table 4 shows the extracted lumped circuit parameters for the metafilms MM1, MM2, MM3 using the experimental data.

Sample	R (Ω)	L (pH)	C (fF)
MM1	146.35	484.6	0.27
MM2	51.71	193.8	0.32
MM3	105.15	184.52	0.19

Table 4 Extracted lumped circuit parameters for ATR measurements on metafilms.

The results shown in Table 4 vary from the extracted *R, L* and *C* circuit parameters for the *RLC*-TL model seen from Table 4 above. The extracted inductance for MM1 is unusually high compared to the other two metafilms. No simple clear behavior is evident in the extracted lumped circuit parameters for the metafilms. The resonance frequency extracted from the ATR fit differs from the observed resonance frequency extracted from the normal incidence transmission fitting from the previous section. The measured transmission quality factors and resonance frequencies are different from those of ATR. Figure 7-9, Figure 7-10 Figure 7-11 show the comparison between the measured ATR data and the calculated curves based on the *RLC*-TL model for metafilms MM1, MM2 and MM3 respectively. Due to restricted measurement bandwidth, only the low-order Lorentzian resonance corresponding to the fundamental *LC* resonance is used for fitting. For these measurements, the center of the sample was illuminated by the incident terahertz beam.

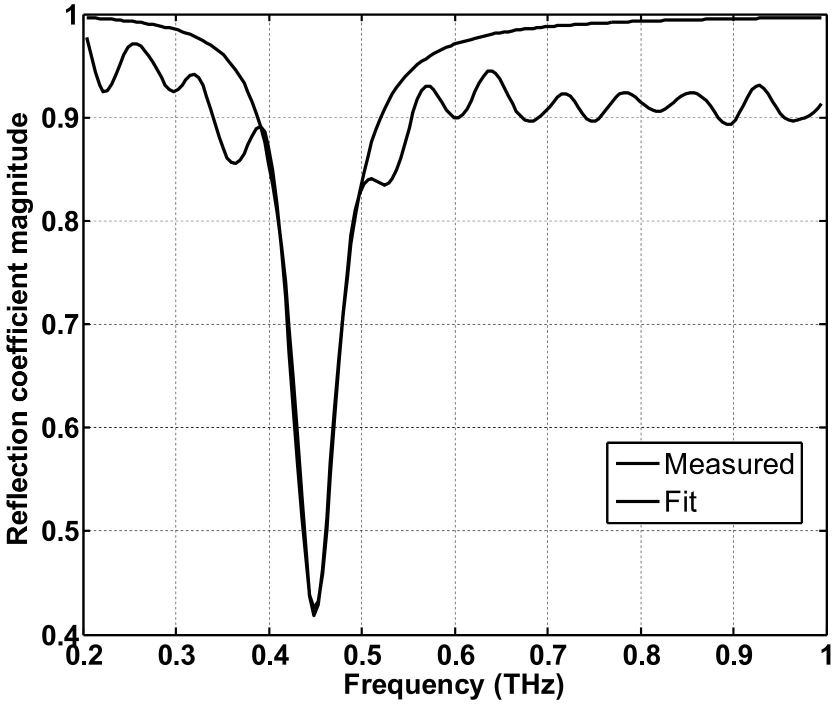

Figure 7-9 Reflection coefficient (ATR) for metafilm MM1 from measurements (solid) and *RLC*-TL circuit model (dashed).

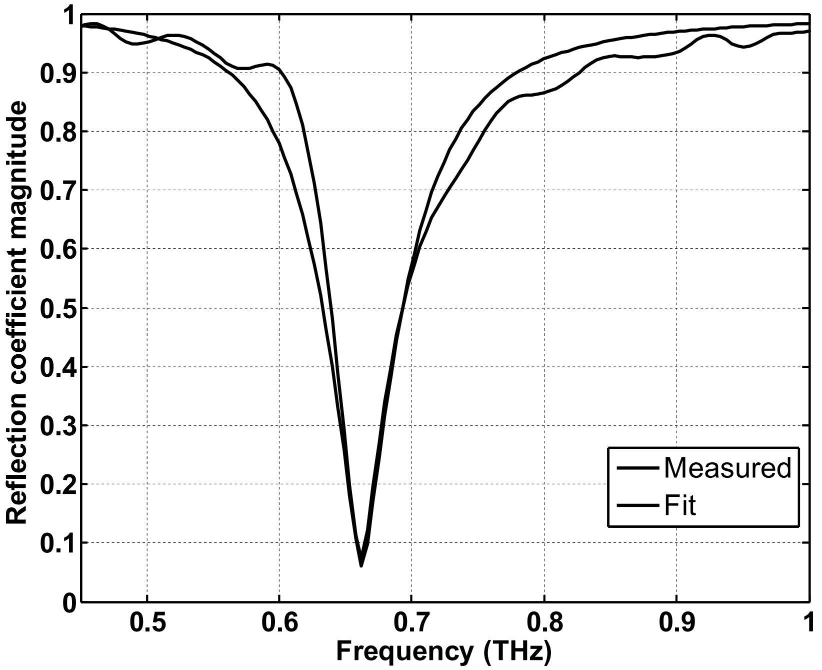

Figure 7-10 Reflection coefficient (ATR) for metafilm MM2 from measurements (solid) and *RLC*-TL circuit model (dashed).

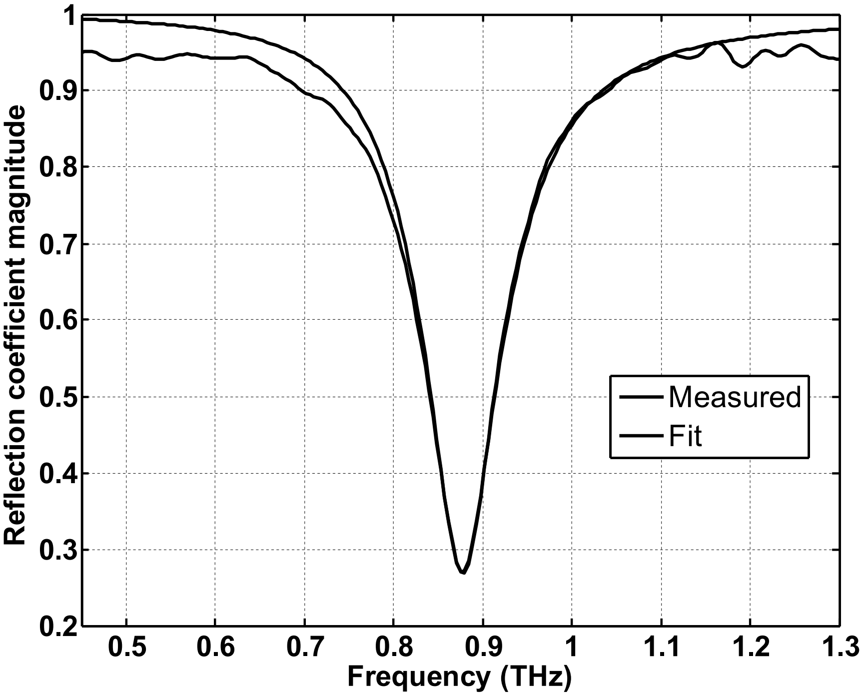

Figure 7-11 Reflection coefficient (ATR) for metafilm MM3 from measurements (solid) and *RLC*-TL circuit model (dashed).

Despite the asymmetry and differences in the off-resonance levels, there is a close agreement between the frequency dependent ATR spectra and the calculated amplitude reflection coefficients.

TIR Transmission coefficient

The transmission coefficients for the TIR configuration (Figure 7-3 and Figure 7-7) can be derived following the approach outlined earlier and the corresponding TIR transmission coefficients for the sample can be expressed as

$$t_{ATR}^{sam} = \frac{2Z_{surf} \parallel Z_0}{Z_{surf} \parallel Z_0 + Z_{Si}} \tag{7.12}$$

and the TIR transmission coefficient for the reference is

$$t_{ATR}^{ref} = \frac{2\widetilde{Z}_0 \,||\, Z_0}{\widetilde{Z}_0 \,||\, Z_0 + Z_{Si}} \tag{7.13}$$

the ratio of which is the transmission coefficient at the TIR boundary expressed as

$$t_{ATR} = \frac{Z_{surf} \,||\, Z_0}{Z_{surf} \,||\, Z_0 + Z_{Si}} \frac{\widetilde{Z}_0 \,||\, Z_0 + Z_{Si}}{\widetilde{Z}_0 \,||\, Z_0} \tag{7.14}$$

Using the extracted R, L, C parameters in the expression for t_{ATR}, a plot of t_{ATR} as a function of frequency for the sample MM1 is shown in Figure 7-12.

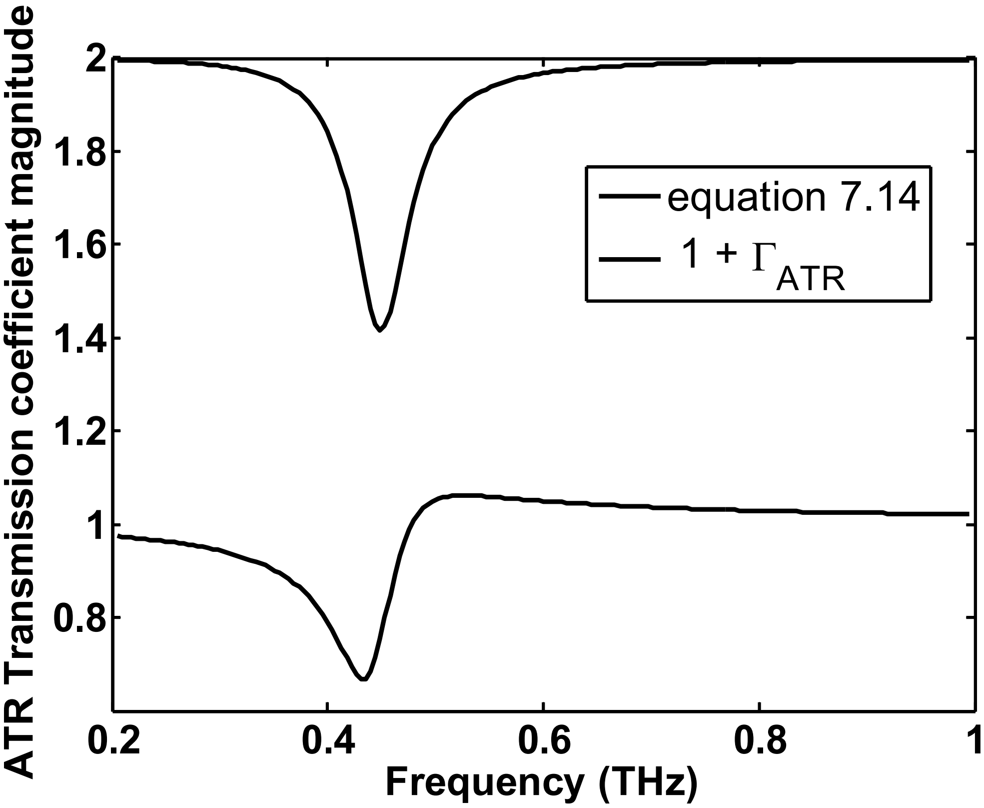

Figure 7-12 Calculated ATR Transmission coefficient using equation (7.14) shown as a solid curve and dashed curve corresponds to the relation $t_{ATR}=1 + \Gamma_{ATR}$.

The transmission coefficient at the TIR boundary t_{ATR} using equation (7.14) is shown as a solid curve in Figure 7-12 for a silicon-air interface in the presence of a metafilm. It exceeds 1 for frequencies above resonance and shows a dip around the resonance instead of a peak.

The transmission coefficient arising in a TIR situation can also be derived from the calculated reflection coefficient using the relation $t_{ATR} = 1 + \Gamma_{ATR}$ for perpendicular or s-polarization. Here, it does not equal to the quantity $(1 + \Gamma_{ATR})$, the magnitude of which is plotted in the top half of Figure 7-12. The attenuated reflection coefficient Γ_{ATR} in the above relation was calculated using equation (7.11).

The results from the *RLC*-TL model specifically interpreting the TIR transmission coefficient are yet to be fully understood. It yields inconclusive results that are difficult to interpret, other than the behavior varies strongly near the resonance. The intent in using this mathematically accessible and established approach [105, 106] was to prove that the metafilm modifies the TIR condition near the *LC* resonance, but it does not allow transmission across the TIR boundary. The fact that conservation of energy should hold indicates that the transmission predicting gain is non-physical. Thus the simplistic effective medium transmission line model fails to capture the observed experimental behavior of the metafilm in ATR.

The failures would lead one to expect that the responsible mechanisms are not inherent to the *RLC*-TL model. The results of the transmission using the above approach are totally non-physical which indicates that the treatment of the metafilm surface as an effective medium will not explain the physical mechanisms responsible for the observed re-radiation. The model is one-dimensional, but the ATR configuration requires at least two dimensions to describe the plane of incidence. The metafilms are discrete in nature and the arrays and excitation are bounded.

7.4 Lumerical 3D

Finite Difference Time Domain (FDTD) simulations using Lumerical 3D were performed to overcome the limitations of the previous approaches. FDTD solvers generate physically relevant fields during the simulation process and allow visualization of propagation behavior. The intent in using this approach was to use a time domain simulation to be able to visualize the coupling and re-radiation mechanisms to guide interpretation of the experimental results.

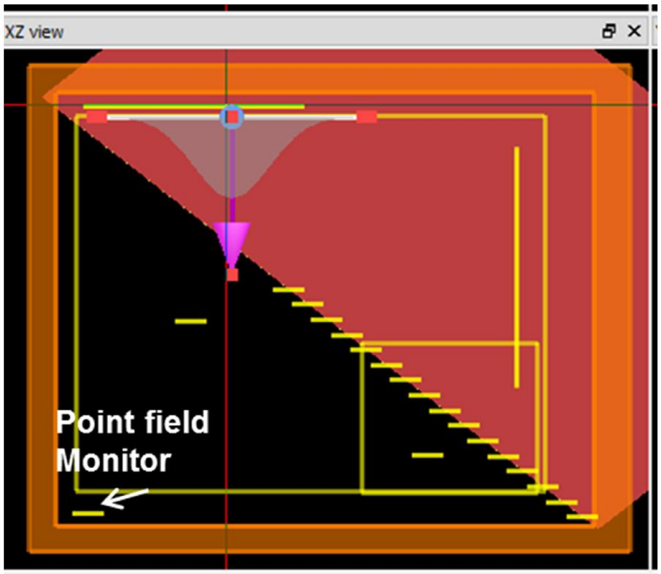

Figure 7-13 Lumerical FDTD simulation model showing the XZ plane view.

The simulation space is shown in Figure 7-13. A Gaussian profile incident beam is shown at the top, propagating downward in the direction of the pink arrow. The silicon prism is shown shaded red in the upper right region and the air space is in black in the lower left. The SRRs are modeled on the TIR boundary using actual dimensions (MM1). The TIR surface has 27 SRRs and is referred to as a "full" array. Simulations were performed with fewer SRRs to correspond to the edge of an array. Various field monitors are shown in yellow. The one of interest is the point field monitor indicated by the arrow which is as far away from the prism as possible within the available computational space.

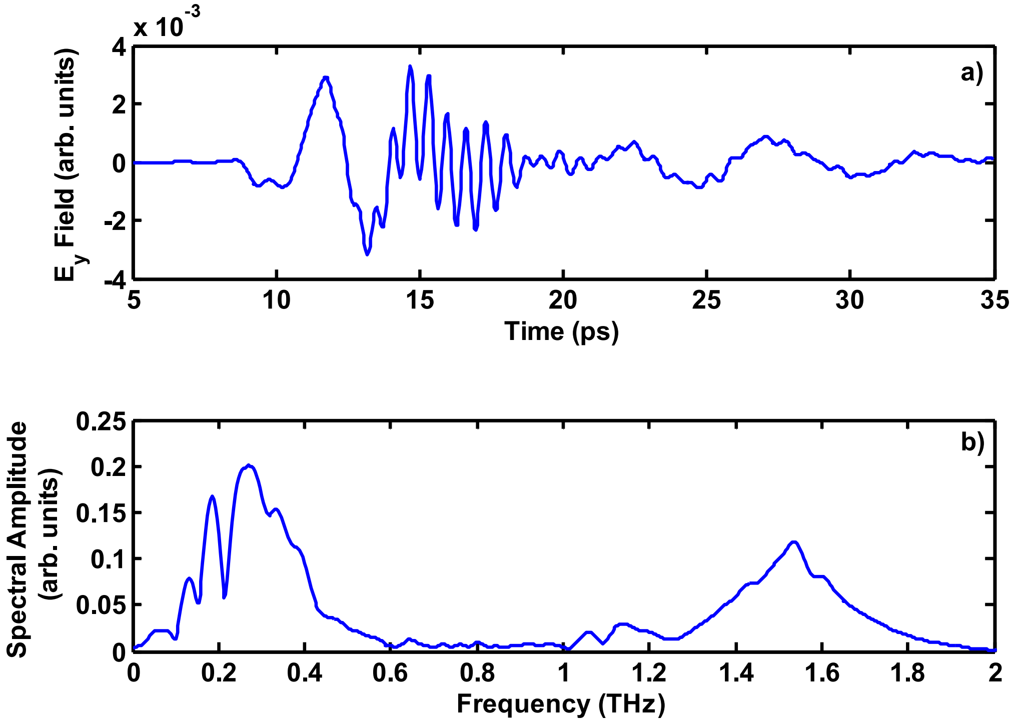

Figure 7-14 Signal from the point field monitor indicated in Figure 7-13. a) Time domain b) Frequency domain.

The initial results obtained from this simulation are shown in Figure 7-14. The signal resembles the measured re-radiation signal seen in Chapter 6. There is a low frequency peak that is near the observed *LC* resonance and a high frequency ringing that is located near the transmission grating frequency.

However despite the superficial resemblance, there are concerns with this result. Specifically, the *LC* resonance does not correspond to the actual measured resonance for MM1 (0.45 THz). There is a remnant background signal present between 10 ps and 15 ps that is present in the re-radiation signal. Unlike the detector in the experiment which is sensitive only to paraxial rays, the point monitor collects all signals irrespective of propagation directions, resulting in additional artifacts. Also the position of the point monitor is 1 mm away from the TIR surface, not in the far field, as opposed to the location of the THz receiver that is 300 mm away. The incident beam size of 200 μm is much smaller than the experimental beam size of 3 mm. As a result there is a larger k vector spread which is equivalent to an increased range of angles. Small beam size also implies fewer elements contribute to the transmission grating signal. The beam was not centered on the array since the intent was to observe the coupling of surface waves to the edge of a truncated array.

Further refinements were implemented to address the above concerns. The beam size was increased to 270 μm. The beam position was changed to align with the edge of the array when truncated. The computational space was expanded and background measurements were recorded by running simulations without the presence of the SRR array. The boundary conditions were changed from periodic to Bloch. Figure 7-15 shows the improved simulation space.

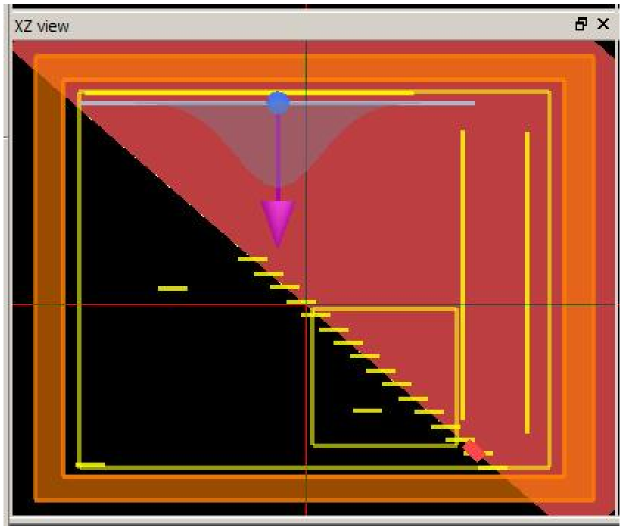

Figure 7-15 Improved Lumerical FDTD simulation model showing the XZ plane view**.**

Figure 7-16 shows the time domain data with the background removed for four cases. The blue trace (top) corresponds to the full array mimicking the infinite array condition. The green curve (second from top) introduces truncation by having half (14 SRRs) as many SRRs as a full array. The beam peak is centered on the edge element. This situation resembles finite arrays and was considered since there is a correlation between the edge of the array and the measured *LC* re-radiation signal. The red and cyan curves have two and four unit cells respectively added onto the truncated edge, corresponding to 16 and 18 SRRs respectively. This is equivalent to moving the beam farther into the array.

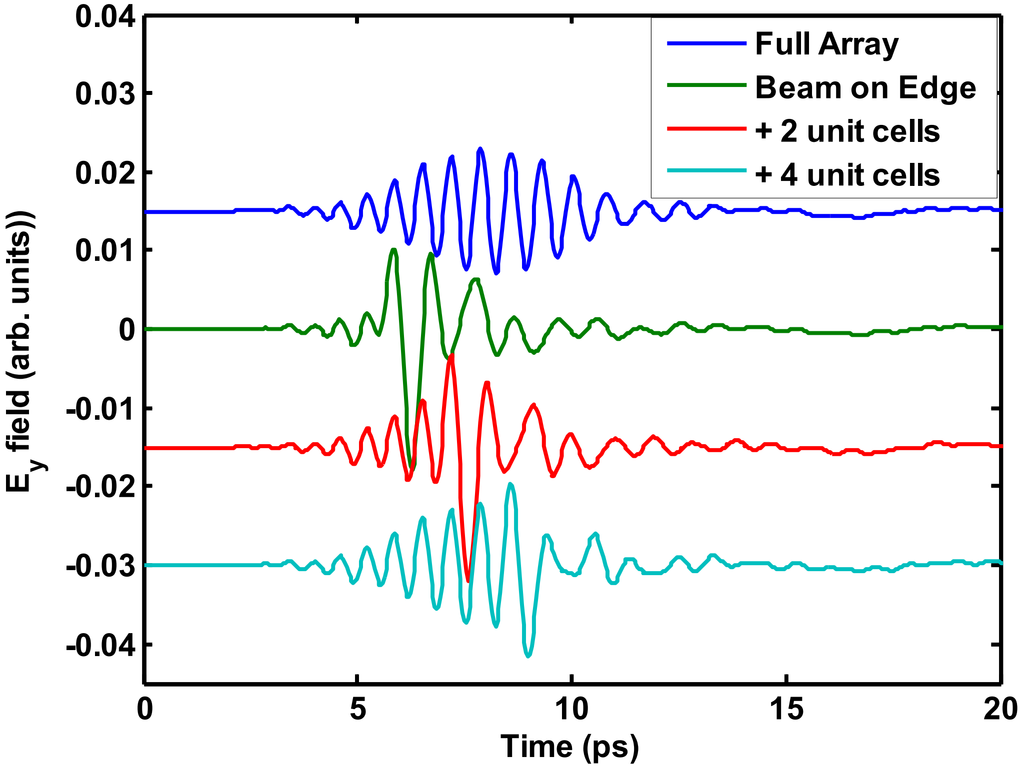

Figure 7-16 Time domain data from the improved simulation model. Traces are shifted vertically for clarity.

The full array trace shows a single frequency envelope. Short pulse features appear in the other traces.

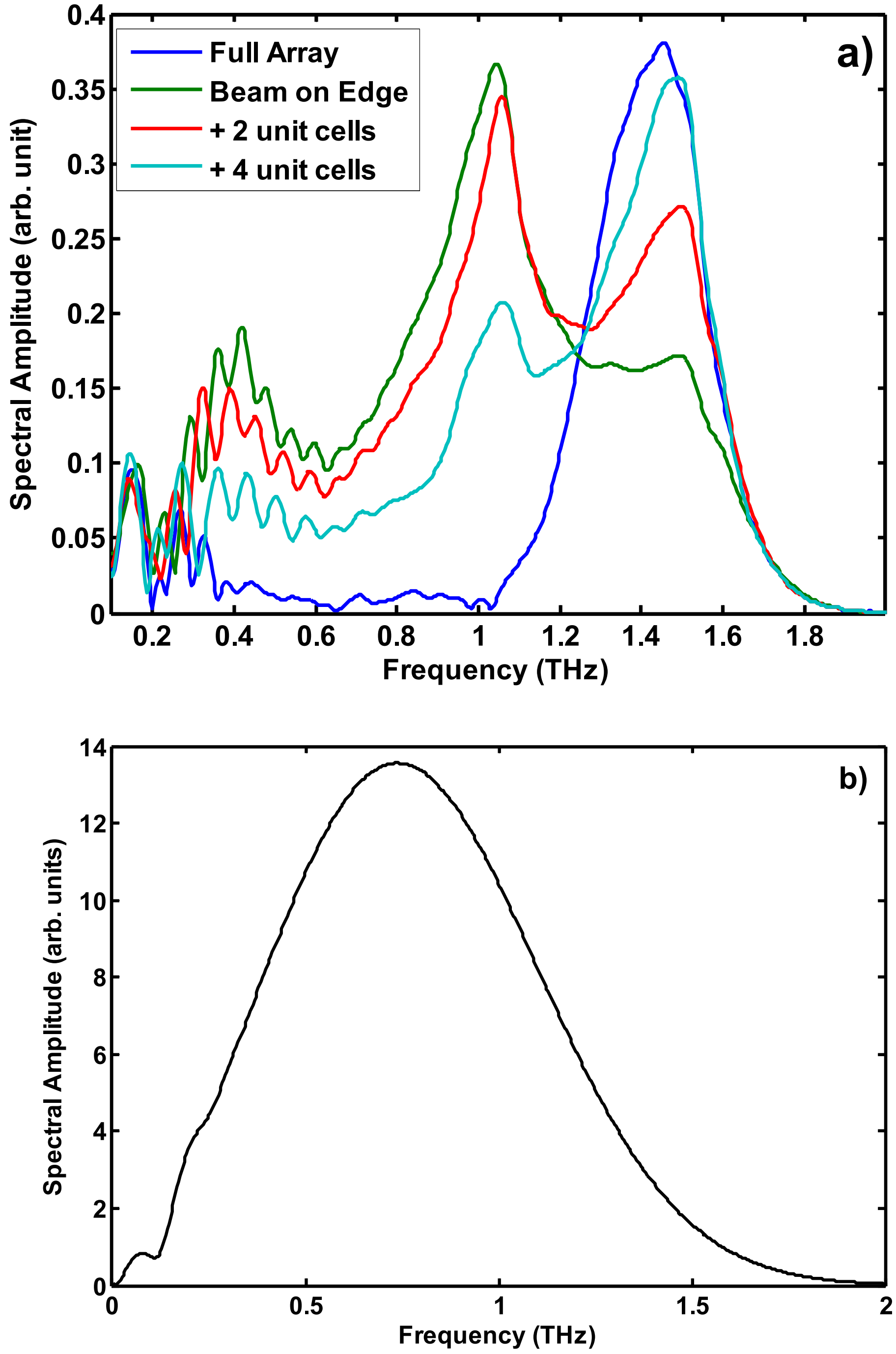

Figure 7-17 a) Spectra corresponding to time signals from Figure 7-16. b) Excitation spectrum.

The corresponding Fourier transformed spectra are plotted in Figure 7-17 a) along with the input ATR spectrum in Figure 7-17b). The resultant spectrum shows significant differences with respect to the initial results from Figure 7-14. The full array (blue curve) shows a clear transmission grating response near 1.5 THz. There is no *LC* resonance. The low frequency response below 0.2 THz is an artifact of the boundary conditions. The incident beam on the edge of the array (green curve) corresponds to the truncated array. It shows a broad background possibly due to edge diffraction signal that distorts the resulting spectrum. The transmission grating is suppressed with respect to the full array results due to the monitor in close proximity to the array and shows a relative frequency shift which is equivalent to having a different observation angle. However the *LC* resonance is strongly evident at 0.4 THz. The other spectra (red and cyan curves) corresponding to two/ four unit cells added to the truncated array show the recovery of the transmission grating signal and reduction of the background. And the *LC* resonance peak also starts to disappear.

These results were promising but have proved difficult to interpret. Other analytic approaches were required to pinpoint physical mechanisms that were responsible for the observed re-radiation in the metafilms.

7.5 ATR Reflectance Interpretation

The experimental data can also be interpreted in other ways where the surface wave could be attributed to a “three-way loss mechanism” [107]. In the first possible interpretation, the surface wave could absorb energy as Ohmic loss in an ATR measurement that would otherwise be reflected and measured. Secondly, the surface wave may radiate energy as it propagates in the less dense medium, in this case air. The third mechanism as proposed earlier is when the surface wave radiates energy when it reaches the edge of the metafilm array. Assuming energy is coupled into a surface wave, the re-radiation from the edge could possibly account for the anomalous increase in resonance strength.

In a thin film/low loss ATR experiment, the ATR reflectance spectra resembles a direct transmittance measurement so the optical relation is modified to become 1 = R + A [8], where the reflectance is the square of the measured quantity R = $\left|r_{atr}(\omega)\right|^2$. Based on the experimental results, the conservation of energy equation can be recast as 1= R + A_{rr} + A. The additional term A_{rr} accounts for the radiation signal from the induced currents in the SRRs that couple to adjoining SRRs through surface wave interactions but are radiated out of the measurement after encountering the edge of the array or where energy goes into surface waves which travel away from the SRRs near the center of the array and are attenuated or radiate into the dense medium (the IRE) before they reach the edge. In other words, A_{rr} depends on inter-element coupling and is a function of beam position with respect to the edge of the array. Since strong inter-element coupling should only be expected for closely-spaced rings and for resonance-enhanced currents, these surface wave losses are isolated near the fundamental frequency of the SRRs. This results in the apparent strength of the resonance being modified by position while the background ATR signal remains unchanged in measurement. This is evident from the strong dips in the ATR measurements for sample MM1 (Figure 6-12). The effect is significantly reduced in MM2 and is not evident at all in MM3. In a terahertz ATR reflection measurement, since there is no transmittance [10], the measured component is taken to be only reflectance and absorption A is considered constant. When a THz ATR measurement is performed with the beam located near the edge of the MM sample the measurement records R only. Because the hypothesized surface waves set up on the SRRs when the beam is focused near the edge of the finite array experience a sudden discontinuity, the energy they contain then can re-radiate out of the TIR face of the sample and are not detected, thus increasing the contribution of the A_{rr} term. When the measurement has an incident beam focused at the center of a sample (corresponding to the infinite array regime of Figure 6-12) this A_{rr} term is re-emitted preferentially into the high index substrate by a factor of n^3 [20], approximately x40 for silicon. Then A_{rr} may be relatively reduced.

Edge-radiated energy may have unexpected effects if not properly accounted for. For example, in metafilm perfect absorbers, the absorbance determined from measuring R alone and not $(R+A_{rr})$ for the MF sample at resonance would be artificially high. This could lead to incorrect conclusions regarding the absorption characteristics of planar metamaterials measured in reflection. This phenomenon also represents a possible hurdle in assigning effective material parameters to bulk or 2D metamaterials especially if they are of a finite size, on the order of the beam area, or exhibit strong inter-element coupling.

The two potential mechanisms explaining the experimental observations, namely surface waves and edge effects, are elaborated in the following paragraphs.

7.6 Analytic approaches describing re-radiation

Phase matching conditions should prevent any transmission beyond critical angle despite the presence of a metafilm at the TIR interface if one considers the metafilm as a continuous and an infinite effective medium. Subsequently, either the finite array size or the discrete nature of the resonant elements of the metafilm or both must facilitate the experimentally observed re-radiation.

Illumination either partially or fully at the edge leading to a strong re-radiation signal also suggests edge diffraction to be a potential phenomenon. But direct edge diffraction such as diffraction from an opaque screen or a knife edge would give a more broadband response[68] because it would diffract all the frequencies of the incident field. Thus the nature of the resulting re-radiation signal would be broadband from a broadband THz excitation source and not frequency selective at the SRR resonance frequency. This effect was seen using finite difference time domain simulations (Lumerical 3D). Also the observed broadside radiation, though weak would not be present when the incident wave is on the center of the array. Thus in this case, one can argue that the measured phenomenon is not merely edge diffraction at an arbitrary boundary between differing surfaces due to the strong frequency selective component (near the *LC* resonance of the SRRs) but a phenomenon intricately correlated to the behavior of the metafilm.

A surface wave can be excited along the array that can alter the phase relationship between the various radiators on the array beyond the fixed phase advance determined by the incident driving field. There can be a fast surface wave that could give rise to leaky radiative waves. Or a non-radiative slow wave could be excited that then encounters an array edge (impedence mismatch) and radiates.

In order to completely characterize the fields at the TIR boundary, theory demands a more rigorous analysis than is available in the current literature. Full wave simulations using commercial packages such as CST and Lumerical do add insight into the actual behavior, but do not allow isolation of individual physical mechanisms. Simple filter theory as described in an earlier section fails to capture the physics responsible for the observed re-radiation signal.

The lack of theoretical treatments of these issues required assistance from collaborators better versed in electromagnetic modeling and wider analytic foundations to understand the nature of this observed phenomenon and conclude if this re-radiation arose from edge effects or from surface waves. Guided by the observations from previous chapters, the experimental results were phenomenologically reproduced by the following approaches which indicate that the physics for the re-radiation mechanism is captured.

7.6.1 Floquet method

Metafilms are inherently periodic structures. Therefore, one can use the Floquet treatment to describe the interaction between neighboring unit cells when the array is excited by an incoming plane wave. The array is assumed to be infinite. Thus edge effects do not enter this line of treatment. This method requires the discretization of the split ring resonators. Since the excitation is oblique, the resonators have different phases, but this too will be periodic having a fixed relationship due to geometry (unit cell size) and phase advance due to the tilted phase front of the driving field (angle of incidence of the THz beam.)

The analysis assumes a one-dimensional array of infinite wires (in lieu of SRRs) located at the TIR boundary to simplify analysis even though the actual metafilm is a two-dimensional array of SRRs illuminated by a plane wave. The setup for this approach is shown in Figure 7-18. The wire array is along the y-direction and is periodic along the x-direction. Gold patches located at the Si-air boundary represent individual line sources separated by a distance *d*. The SRRs are represented by line sources on the dielectric-air interface. The scattered field in a periodic structure can be expanded via the Floquet theorem. According to the Floquet theorem [108] [109], the field component in the frequency domain for a structure that is periodic in the x-direction, obeys the following relation,

$$E(x,y,z)=E(x+d,y,z)\exp(jk_x d) \tag{7.15}$$

The advantage of this method is that propagation properties for an array can be derived by considering a single unit cell which considerably reduces computational overhead.

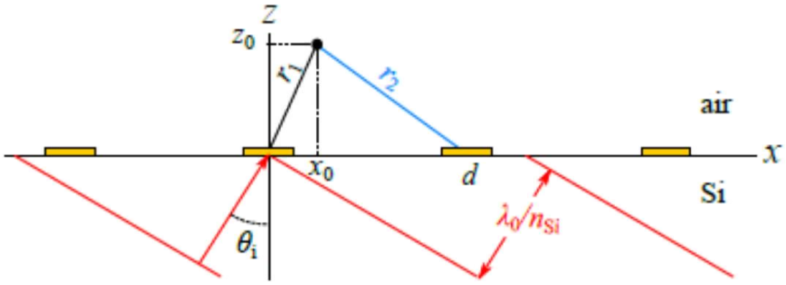

Figure 7-18 Theoretical analysis concept showing the principal excitation from plane waves (red) in the silicon prism. Small gold patches along boundary represent SRRs that are modeled as infinitesimal wires for Floquet analysis.

The resulting electric field generated on the air side of the wire array can be expressed as

$$E_y(\omega)=\sum_{m=-\infty}^{\infty} F(\omega)e^{-j\left(k_0 m d n_{Si}\sin\theta_i\right)}G_a(\omega,\mathrm{r}_m) \tag{7.16}$$

where k_0 is the free-space wavenumber. $F(\omega)$ is the interaction of the SRRs with the incident field and is a complex, frequency dependent amplitude determined by the incident wave and/or resonant properties of the SRRs. Ga(ω, r_m) is the Green's function of the *m*th wire on the TIR boundary which is essentially the frequency dependent transfer function that describes the radiation pattern of the individual elements on the air side. Green's functions for radiating elements on a dielectric interface are challenging to develop with an analytically rigorous model for all but the simplest cases. *F* is the driving function and r$_m$ is a vector to the observation point originating at the *m*th wire.

$$r_m = \sqrt{\left(x - md\right)^2 + z^2} \tag{7.17}$$

The phase of the incoming wave contained in the exponential term in equation (7.16) is

$$\phi(m) = k_0 m d n_{Si} \theta_i \tag{7.18}$$

The Green's function describes the field from a given radiating element observed at any given point in space. The task remains in finding the Green's function for a line source on the dielectric-air interface. This is shown in Eq(7.19). The Green's function can then be used to determine the fields generated by the line source equivalently due to a single SRR on the metafilm. The Green's function was found to be[110]

$$G_a = -\frac{\omega \mu_0 I}{\sqrt{2\pi}} \frac{z_0 e^{j\pi/4}}{z_0 + r\sqrt{n_{Si}^2 - \left(x_0/r\right)^2}} \frac{e^{-jk_0 r}}{\sqrt{k_0 r}} \tag{7.19}$$

For this to work, the assumption is that the SRR array would radiate similar to a line source with an equivalent line current. Thus the Green's function for a small loop is approximated by that of a wire. The fundamental radiative behavior would be reproduced since in actuality, an SRR is both a magnetic and an electric dipole in nature (see Chapter 4 for discussion). But here only the effect due to an electric dipole is treated.

When the angle of incidence exceeds the critical angle, the component of the wavevector normal to the interface (*z*-direction) on the air side becomes imaginary[68]. The components of the wavevector in air are given by

$$k_{0x} = k_0 \sin\theta_t \quad \textit{and} \quad k_{0z} = k_0 \cos\theta_t \tag{7.20}$$

Using snell's law, the z component of the wavevector can be written as

$$k_{0z} = -ik_0\sqrt{\frac{\sin^2\theta_i}{n_{ti}^2} - 1} \qquad (7.21)$$

where

$$n_{ti} = \frac{n_t}{n_i} = \frac{1}{n_{Si}} \qquad (7.22)$$

The value of the radicand in (7.21) is positive because for all values of θ_i above critical angle, the ratio $\frac{\sin^2\theta_i}{n_{ti}^2}$ will be greater than one, thus leading to a physically realizable solution of an exponentially decaying evanescent field. Thus the transmitted field in the rarer medium given by (7.16) becomes evanescent. Following the above arguments, the Floquet method should not predict any re-radiation at the SRR frequency.

However, the actual measurements are not dealing with an infinite array. Therefore the fields from equation (7.16) can be modified for the case of a finite array

$$E_y(\omega) = \sum_{\substack{p= \\ q=}}^{l/2d} \sum_{-l/2d} A(x,y)F(\omega)e^{-j\left(k_0 p d n_{Si}\sin\theta_i\right)}G_a(\omega, r_{pq}) \qquad (7.23)$$

Here l denotes the full width of the array. The double summation indicates that the array is bounded in both x and y. Due to the obliquity of the terahertz beam in the x-direction, one can simplify the above equation by ignoring the fields in the y-direction reducing this to a one- dimensional array and subsequently less computationally intensive problem. By truncating the array as shown in equation (7.23), it no longer strictly follows Floquet's theorem, "…which basically states that for a periodic structure, the phases of the element currents must match those of the incident field. However, when the structure becomes finite, it is no longer periodic and Floquet's Theorem simply does not apply." [111] Therefore caution must be exercised when departing from the infinite array approach.

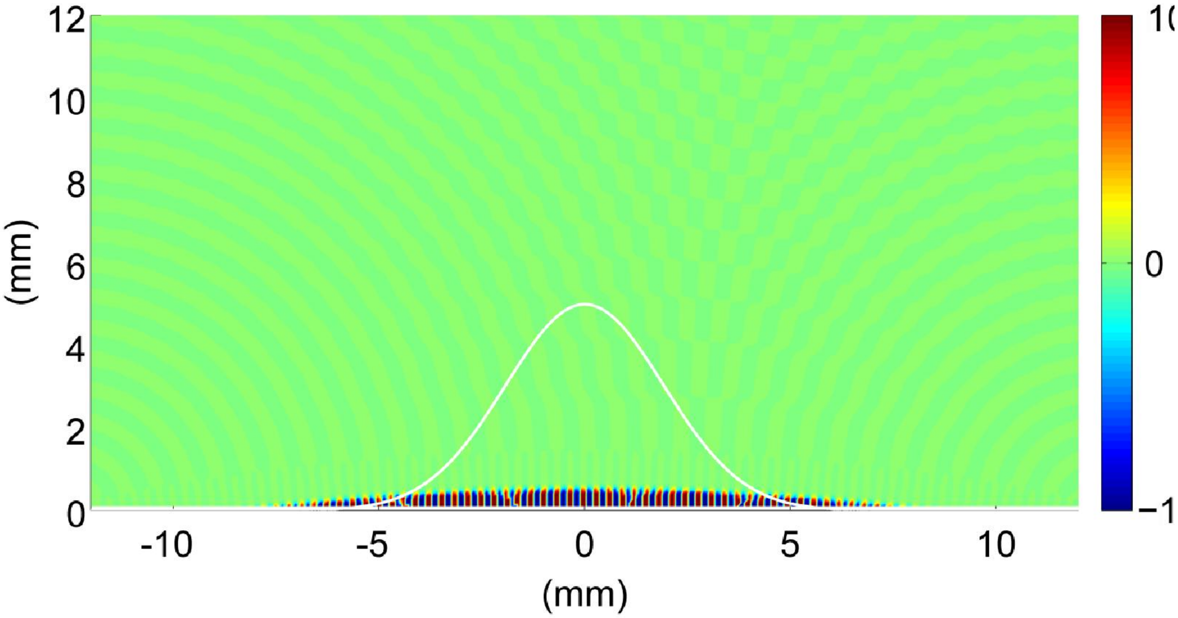

Figure 7-19 Electric field amplitude corresponding to s-polarization at the resonance frequency of 0.4 THz at the TIR boundary for a wire array that is 25 mm wide. No inter-element coupling is explicitly included in this treatment. The incident terahertz beam is shown in white [107].

Figure 7-19 uses equation (7.23) to show the electric field for a line array when excited obliquely at the resonance frequency of 0.4 THz similar to the experiment. For this case, coupling between elements is ignored. The terahertz beam at the TIR interface is assumed to be 5 mm wide (45°). The line array is 25 mm wide and the spacing between adjacent line radiators is 80 μm. The Gaussian profile (in white) shows the intensity distribution for the incident field as a function of position. There is no transmission at the resonance frequency when the coupling between individual radiators in a finite SRR array is taken to be zero. This in agreement with the arguments presented earlier where only the evanescent field prevails, extending a short distance into the air side of the TIR boundary. On the other hand, with the same geometry and excitation conditions, there is radiation at the grating frequency of 1.55 THz that is emitted normal to the TIR boundary in agreement with the re-radiation measurements. This is shown in Figure 7-20 and different frequencies would produce radiation at different transmission angles in accordance with the grating equation (6.3). Inter element coupling plays no role in these numerical results and is due only to the discrete nature of the SRRs.

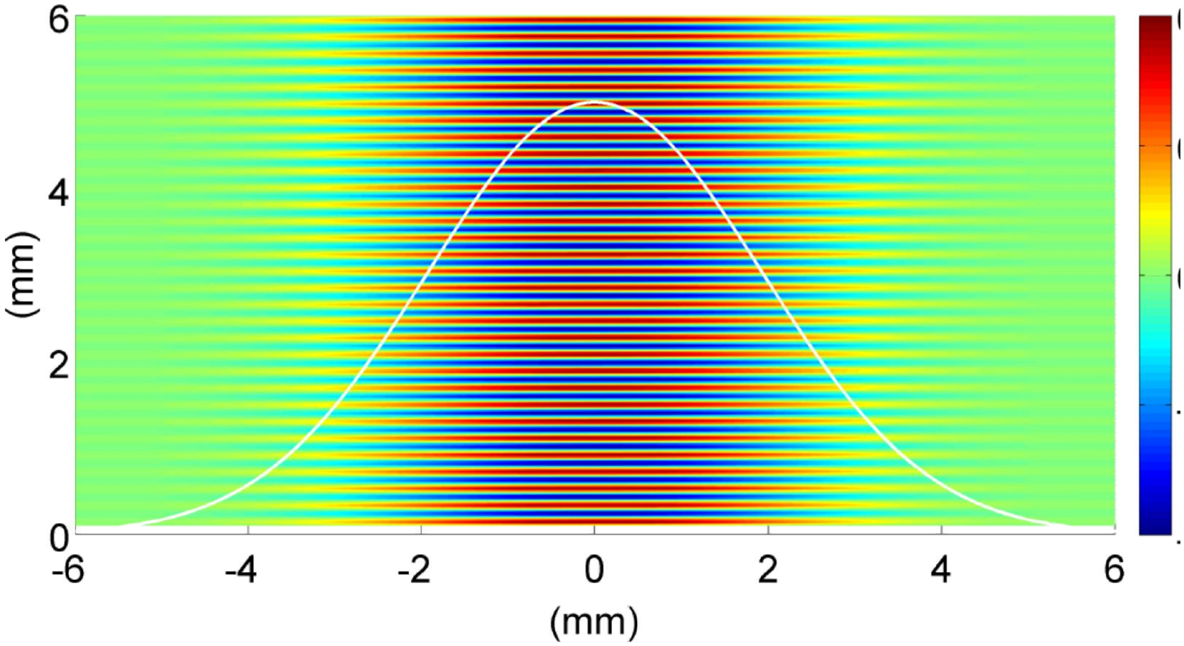

Figure 7-20 Electric field amplitude corresponding to s-polarization at the grating transmission frequency of 1.55 THz corresponding to a 0° diffracted angle at the TIR boundary, for a wire array . No inter-element coupling is explicitly included in this treatment. The incident terahertz beam is shown in white [107].

The results presented thus far do not support the experimental observations seen at the SRR resonance frequency. To reiterate, using the ATR technique, there was weak re-radiation measured at the center of the array, the magnitude of which was considerably less than the re-radiation signal from the array edge. The introduction of an edge would break the periodicity of the array and would possibly change the behavior of the TIR interface.

To address this, the numerical experiment has the periodic line sources truncated at x = + 5mm and x = −12.5 mm. Edge effects become apparent as shown in Figure 7-21 where the terahertz beam is incident near the edge of the truncated line array. The array is now 17.5 mm wide.

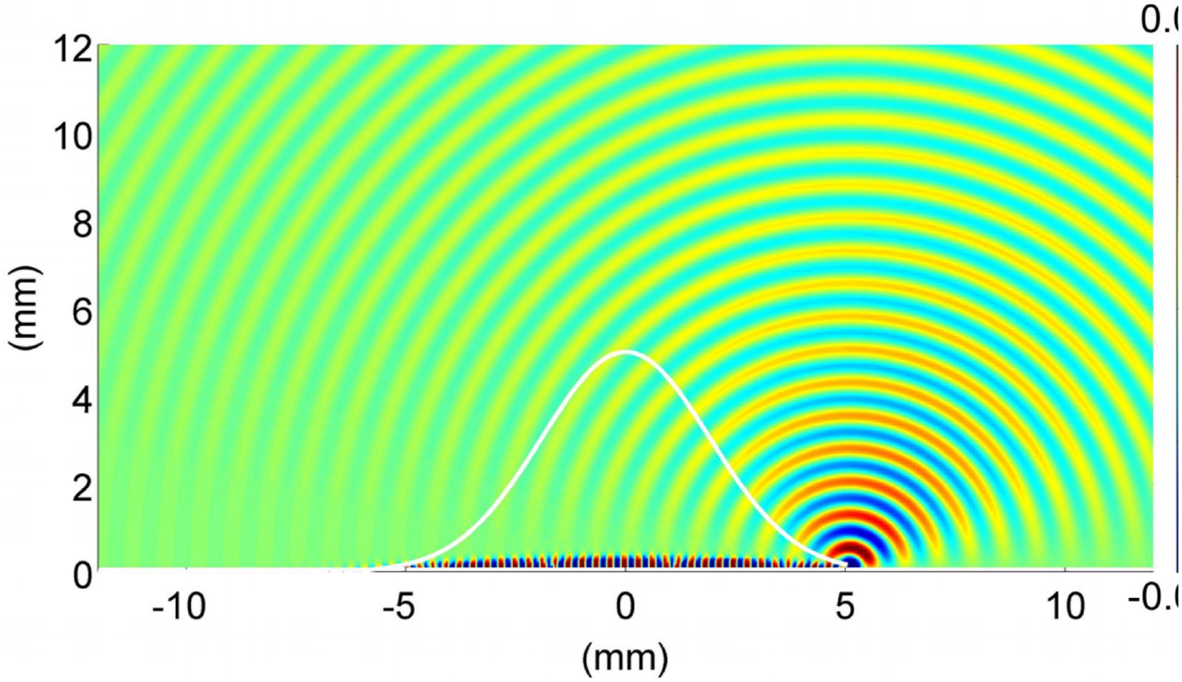

Figure 7-21 Electric field amplitude corresponding to s-polarization at the resonance frequency of 0.4 THz at the TIR boundary for a wire array that is truncated at x = +5 mm. No inter-element coupling is explicitly included in this treatment. The incident terahertz beam is shown in white [107].

There is a dramatic increase in re-radiation emanating from the edge of the array located at x = +5 mm. The input beam size is 3.2 mm (FWHM). The input beam forms a 5 mm elongated spot on the interface. The beam center is shifted such that it is 5 mm from the edge. This calculation strongly supports the observations from the experiment where there is enhanced radiation when the THz beam is shifted to the edge of the metafilm array. Even though the radiation pattern is primarily omni-directional; there is a slight angular dependence which corresponds to similar wide angular features observed in the angular measurements. The angular measurements peaked between 35° and 45° as seen in Figure 6-25. The magnitude of the radiation as shown in the above plot increases considerably when compared to Figure 7-19. This effect is apparent even when the incident field amplitude has dropped off dramatically at the wings of the beam profile. This result shows that inter-element coupling is not a necessary condition for radiation and that the strength of the re-radiation field increases as the incident field intersects the edge of the array.

7.6.2 Surface wave analysis

Although there is a clear edge effect, this does not preclude the contribution of surface wave type of energy transfer, especially with inter-element coupling playing a role. Some radiation was observed in the center of a large array which indicates other mechanisms may be at work. The previous approach that uses Floquet analysis treated the metafilm as a periodic array of discrete resonators with the resonance built into the $F(\omega)$ component of Equation (7.16). The Floquet treatment does not explicitly include the interactions between the elements.

In this treatment, the metafilm is treated as a continuous film. This treatment relies on finding the solutions to the wave equation for a surface wave mediated by inter-element coupling of the metafilm array. The eigenvalues of this wave equation determine the resonances. One root depends on the array geometry or the cell spacing whereas the other depends on the SRR resonance. In order to determine if surface waves play a role in the transmission across the forbidden TIR boundary, consider a SRR and two nearest neighbors on the metafilm array.

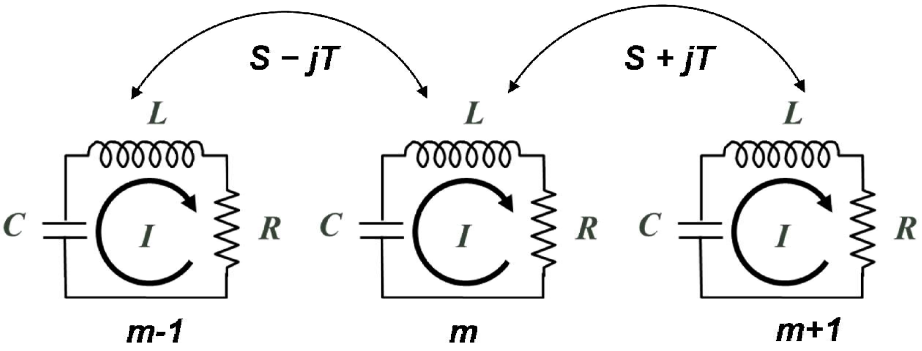

Figure 7-22 Circuit model showing coupled SRRs.

Returning to a simple circuit model for three coupled SRRs as shown in Figure 7-22, the voltage equation using Kirchoff's law can be written as

$$(S - jT) I_{m-1} + Z I_m + (S + jT) I_{m+1} = 0 \tag{7.24}$$

The term $(S \pm jT)$ describes the magnetic interaction between neighboring resonators. Z is the impedance of the SRR defined in terms of the lumped circuit *R*, *L* and *C* components.

For a series circuit,

$$Z = R + j\omega L - j/\omega C \tag{7.25}$$

I_m, I_{m+1} and I_{m-1} are the currents in the *m*th, and adjoining (*m* + 1)th, and (*m*−1)th elements. Treating the array as an effective medium where the wavelength is assumed to be much larger than the spacing between the radiators, equation (7.24) can be expressed as

$$S\left(I_{m-1}+I_{m+1}\right)\rightarrow d^2 S\frac{d^2 I_m}{dx^2}+2SI_m \tag{7.26}$$

$$T\left(I_{m+1}-I_{m-1}\right)\rightarrow 2dT\frac{dI_m}{dx} \tag{7.27}$$

which produces the following surface wave equation.

$$d^2 S\frac{d^2 I}{dx^2}+2jdT\frac{dI}{dx}+\left(2S+Z\right)I=0 \tag{7.28}$$

Let $I=I_0 e^{\lambda x}$,then the roots are

$$\lambda d=-j\frac{T}{S}\pm j\sqrt{\frac{T^2}{S^2}+\frac{2S+Z}{S}} \tag{7.29}$$

The TIR boundary can support two kinds of surface waves based on the eigenvalues from the wave equation. One root is independent of the SRR resonance and is given by

$$\lambda_1 d\approx -2j\frac{T}{S} \tag{7.30}$$

Equation (7.30) suggests that the surface wave resulting from the first root depends on the array geometry together with the dielectric constant of the prism substrate. The other root depends on the SRR resonance and is given by

$$\lambda_2 d\approx j\frac{2S+Z}{2T} \tag{7.31}$$

The field at a specific distance x from a radiator located on the array can be calculated using the following exact solutions[110]

$$E_y=\frac{\omega\mu_0 I}{2\left(n_{Si}^2-1\right)k_0 x}\left[H_1^{(2)}\left(k_0 x\right)-nH_1^{(2)}\left(k_1 x\right)\right] \tag{7.32}$$

$$H_z=\frac{jI}{2\left(n_{Si}^2-1\right)k_0 x^2}\left[2H_1^{(2)}\left(k_0 x\right)-k_0 xH_0^{(2)}\left(k_0 x\right)-2n_{Si}H_1^{(2)}\left(k_1 x\right)+n_{Si}^2 k_0 xH_0^{(2)}\left(k_1 x\right)\right] \tag{7.33}$$

where $H_\nu^{(2)}$ is the Hankel function of the second kind and order ν.

The relation describing the interaction terms S and T is

$$S + jT = -ja\omega\mu_0 H_z \tag{7.34}$$

Even though the experiments intrinsically had electric and magnetic components, here only magnetic coupling is assumed for simplicity. Substituting the expression for H_z from equation (7.33) in equation(7.34), we get

$$S + jT = \frac{a\omega\mu_0 I}{2\left(k_0^2 - k_1^2\right)}\left[\frac{2k_0}{x^2}H_1^{(2)}\left(k_0 x\right) - \frac{k_0^2}{x}H_0^{(2)}\left(k_0 x\right) - \frac{2k_1}{x^2}H_1^{(2)}\left(k_1 x\right) + \frac{k_1^2}{x}H_0^{(2)}\left(k_1 x\right)\right] \tag{7.35}$$

Thus the condition for re-radiation is not solely dependent on the resonant nature of the SRRs but also on the geometric properties of the metafilm array.

7.6.3 Method of moments analysis

Method of moments has been commonly used to study edge effects in frequency selective surfaces and scattering in finite arrays, to name a few related applications to similar electro-magnetic problems. It is used for solving inverse problems by applying orthogonal expansions to translate integral equations into simultaneous linear equations. This problem is non-trivial and requires extensive computational resources to simulate the system in hand. However it is well suited because the metafilm array is finite and discrete with localized currents and a circuit model for SRRs is already established. The following steps outline this approach.

- Compute elements of the Impedance matrix $\left[Z_{mn}\right]$
- Fill incident voltage vector $\left[V_n\right]$
- Find inverse $\left[Z_{mn}\right]^{-1}$

- Solve the linear system to determine currents $\left[I_m\right]=\left[Z_{mn}\right]^{-1}\left[V_n\right]$
- Calculate Far-field radiation pattern E_y from the current distribution on the array.

The total current can be expressed as a summation of primary and secondary currents.

$$I_m = I_{mm} + I_{mn} \tag{7.36}$$

The currents in the line sources due to the incident field, so called "primary" currents are denoted by I_{mm} whereas the effect due to neighboring SRRs is described by the secondary currents I_{mn}. The matrix V_m represents the voltage due to the incident field from the silicon side.

$$\left[V_m\right]=\left[Z_{mn}\right]\left[I_m\right] \tag{7.37}$$

The immediate task is to find the impedance matrix Z. Then the primary currents I_{mm} can be obtained by inversion of equation (7.37). The matrix elements Z_{mm} describes the self-resonances of the individual radiators defined in equation (4.1). The matrix elements Z_{mn} for purely magnetic coupling are determined from equation (7.35). The secondary current on the *m*th line source due to the *n*th line source can be expressed as

$$I_{mn} = \sum_{n=-\infty}^{\infty} \frac{V_n}{Z_{mn}} \tag{7.38}$$

Here V_n is the voltage induced on the *n*th line. Equation (7.23) can be used to calculate the total re-radiation field once the primary and secondary currents are calculated for the case of a finite array.

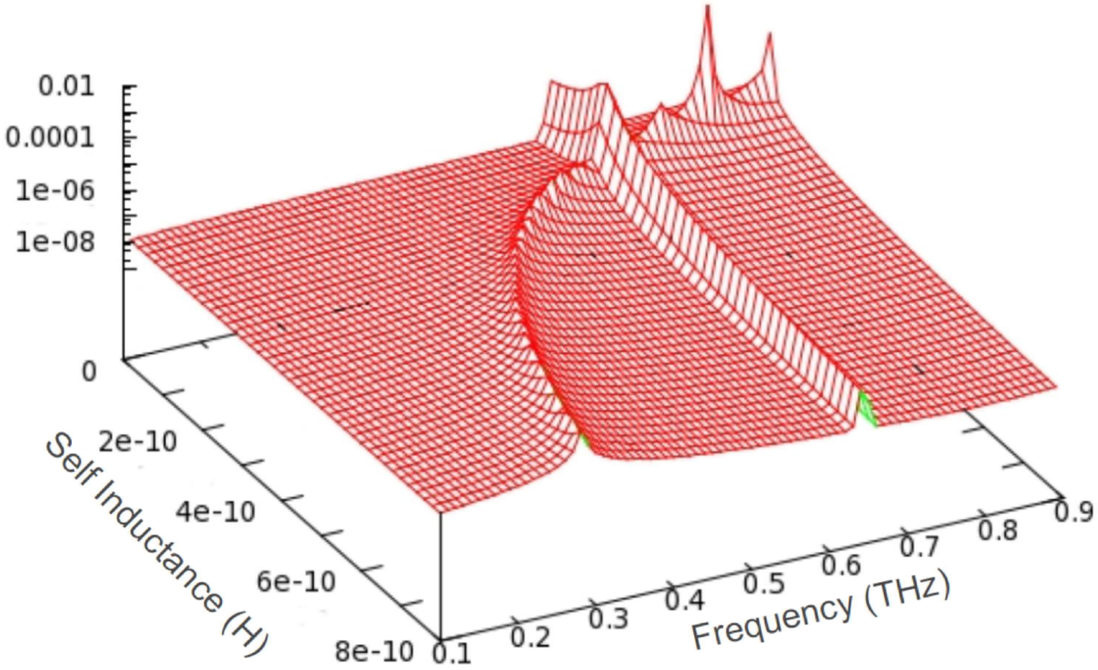

Figure 7-23 Maximum amplitude of the re-radiation field as a function of SRR self-inductance and frequency for the large 2.4 cm array [107].

Figure 7-23 plots the magnitude of the re-radiation E_y as a function of self-inductance. There is an enhanced transmission when the geometric resonance overlaps with the SRR resonance. As the self-inductance increases, the resonant frequency for the SRRs given by $\omega_0 = 1/\sqrt{LC}$ also changes. The SRR resonance transmission is near 0.4 THz whereas the geometric resonance is evident at 0.65 THz.

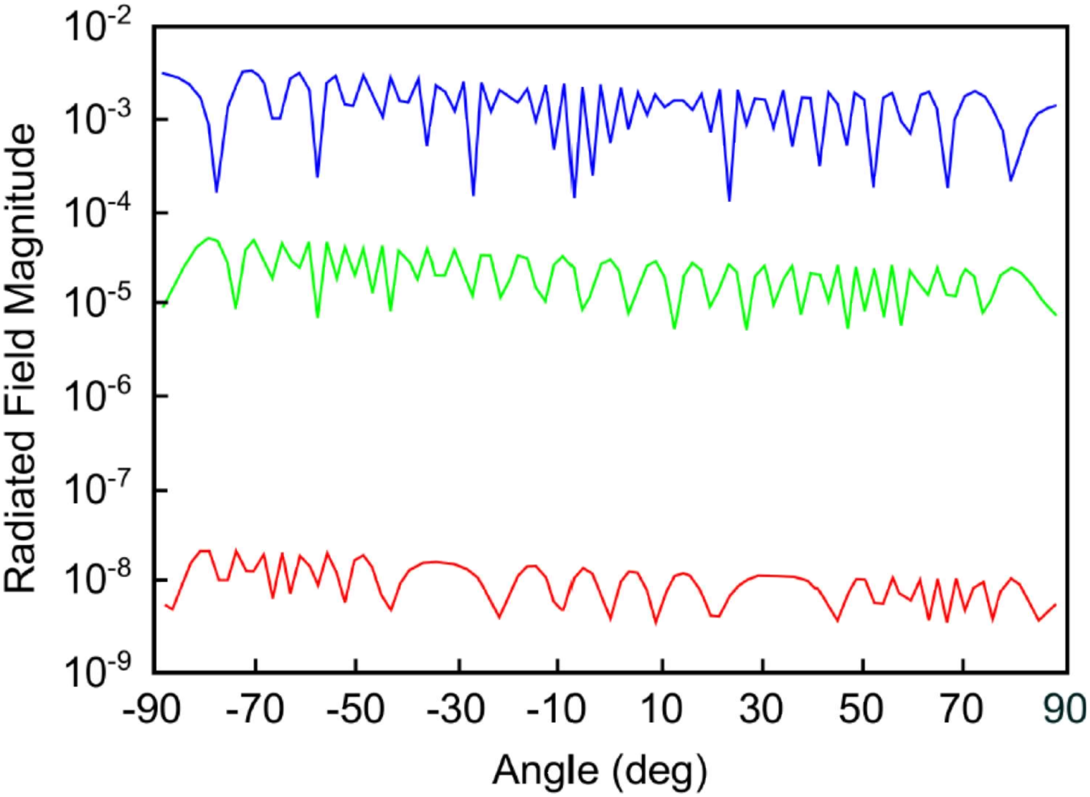

Figure 7-24 Re-radiation field magnitude for three array sizes as a function of angle relative to TIR surface normal at SRR resonance of 0.4755 THz. (Red, bottom) 2.4 cm array ; (Green,middle) 1.6 cm array; (Blue, top) 0.96 cm array. All have centered incident beams [107].

Figure 7-24 compares the re-radiation calculated using the method of moments to determine the current distribution along the array and then generating the far field response from that current for several different widths of the line array. The peak of the response near the SRR resonance frequency of 0.4755 THz is shown. The red curve is the result from Figure 7-23 for a 2.4 cm wide array. The green curve is the radiation field for a 1.6 cm array. Lastly, the radiation for 0.96 cm wide array is illustrated in blue. This corresponds to the 10 mm x 10 mm SRR arrays that initiated the re-radiation study detailed in this document. For all three curves, the beam size is fixed corresponding to the actual beam size and the array size is varied. The magnitude of the radiation in the air half space increases considerably as the array to beam size ratio gets smaller. The plot indicates that there is little angular dependence to the radiation pattern reproducing the observed re-radiation behavior. The field pattern is uniform and is fairly isotropic as expected from a diffracting edge and as illustrated in Figure 7-21 from the Floquet treatment results.

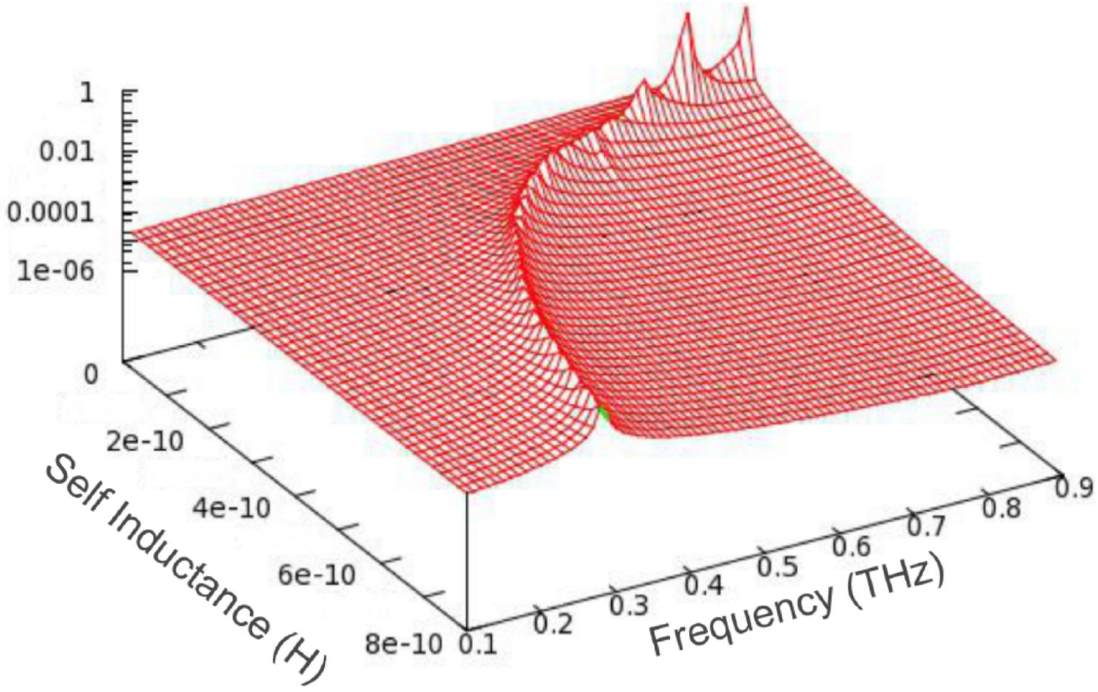

Figure 7-25 Maximum amplitude of the re-radiation field as a function of SRR self-inductance and frequency for small 9.6 mm array. Note the magnitude (z-axis) scale is increased 100**x** compared to Figure 7-23 [107].

Figure 7-25 shows that there is an enhancement of the re-radiation field as the beam is incident on the smaller 9.6 mm array. In this parametric scan, the self-inductance *L* of Equation (7.25) is varied across plausible values which in turn modify the *LC* resonance of the individual SRRs and manifests as the peak re-radiation signal. In other words, the beam gets closer to the array edge as the array dimensions decrease. It is interesting to note that the resonance due to the cell spacing near 0.65 THz is no longer prominent. Only the self-resonance due to the SRR dominates when the array gets smaller, once again matching experimental observations.

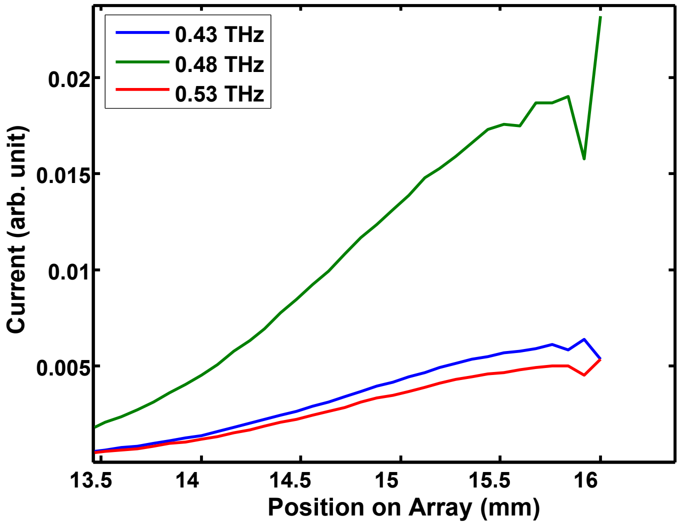

Figure 7-26 Calculated current distribution at the edge of a 16 mm array near the resonance frequency.

The calculated current distribution of the re-radiation signal is shown in Figure 7-26 where the currents are plotted for the resonance frequency of 0.48 THz. The on-resonance current (green curve) experiences a relative enhancement at the edge that is not seen for other off-resonance frequencies.

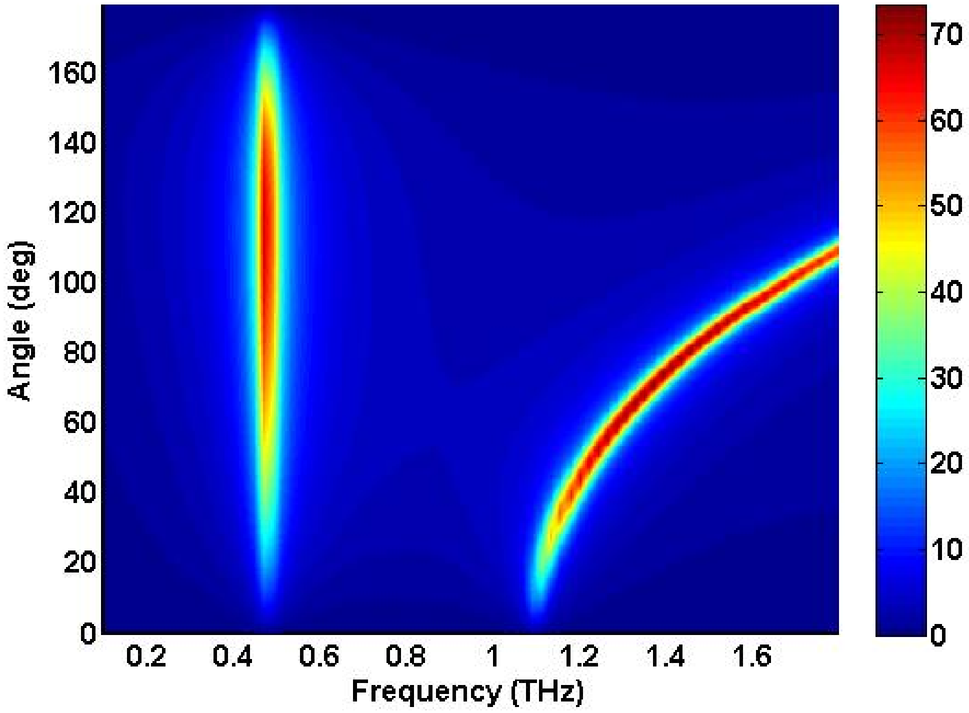

Figure 7-27 Angular dependence of the far field re-radiation pattern

The angular dependence of the far field re-radiation pattern is shown in Figure 7-27 which is calculated from the current distribution generated using the method of moments MATLAB code shown in the appendix. Note the strong resemblance to the measurement shown in Figure 6-25. This approach validates the experimental observations.

7.6.4 Theoretical Conclusion

The Floquet and Method of moments analyses show radiation from metafilms into the far field by oblique excitation from the substrate side by taking into account the finiteness of the array and energy transfer between elements.

Conclusions that can be drawn from the theoretical treatments show

1. Surface waves may exist.
2. Edge effects would appear to dominate under the conditions that the measurements were performed.
3. Further experimental work would be necessary to enhance the surface wave effect and make a definitive measurement.

8 Conclusion & Future work

8.1 Conclusions

The response of metafilms (MF) using THz-TDS in conjunction with ATR technique has been presented. Here an approach to directly measure the THz re-radiation solely from the resonating MF elements without comparing to an unstructured reference substrate is demonstrated. Thus the re-radiation mechanism may lead to a reference free method of probing metamaterial resonance where the MF elements are excited by the THz field through ATR in a prism coupled configuration. However the coupling is very weak in the current ATR configuration using standard metafilm samples.

Research efforts focused in understanding anomalous measurements experimentally observed at total internal reflection surfaces of dielectrics coupled with MFs which may enable improvements in spectroscopy and sensing by taking advantage of the field enhancement at the SRR gap or inter-element coupling increasing the sample interaction length. These measurements were performed on MF arrays with varying resonator sizes in the Kretschmann ATR configuration. The measured fundamental *LC* resonance of the SRRs showed a positional dependence with respect to the excitation beam and MF array placement. This anomalous behavior is referred to in this work, as "anomalous edge enhancement". The anomalous edge enhancement was most strongly observed in the MF array with elements closely spaced with respect to resonant wavelength.

Further investigations also led to measuring the re-radiation signal across the TIR boundary which was unexpected. The re-radiation signal was at the *LC* resonance of the metamaterial. The angular dependence of this signal was studied by taking measurements over a wide range of angles from the normal to the TIR interface. Cross-polarization measurements were performed to isolate the response due to coupling from the incident electric and magnetic fields. The impact of the beam size was considered by designing larger SRR arrays. Several approaches were taken to model the observed re-radiation signal. Numerical simulations using commercial software gave insight into the physical origins of the measured re-radiation signal. Theoretical treatments included the Floquet and method of moments approaches. Both of these approaches were able to qualitatively model the isotropic re-radiation at the SRR resonance frequency. Being able to toggle on and off the inter-element coupling is not possible in an experiment or full wave simulation packages. But the theoretical treatment was able to consider the role of inter-element coupling and also the finiteness of the array independently. Contrary to expectations, inter-element coupling does not play a dominant role in the generation of the anomalous edge enhancement. When the excitation beam is positioned near the edge, edge effects—specifically currents in SRRs with missing nearest neighbors—dominate over surface waves. Theory also predicts the potential of surfaces waves that could occur at the center of the MF array. These would be fast surface waves that would then couple into the MF boundary and re-radiate strongly, but over a much narrower range of angles [112].

The anomalous increase in the strength of the observed resonance could lead to inaccurate conclusions if MFs are used in order to modify or enhance the electric field strength [21], specifically regarding assumptions about the magnitude of the metafilm absorption if the illuminating beam size is on the order of the SRR array or is near a discontinuity such as an edge of a finite array. A modification to the energy equation by introducing an additional term A_{rr} that would account for the re-radiation signal was proposed. The "re-radiation" signal is a potential loss mechanism which is dependent on alignment that could complicate analysis for the electromagnetic behavior of metamaterials under evanescent probing. This also could become a factor when dealing with smaller MF sizes, where the array area is comparable to the illuminating beam area. This phenomenon also represents a possible hurdle in assigning effective material parameters to bulk or 2D metamaterials. Alternately, this mechanism might be utilized to enhance sensitivity by specifically tailoring the MF geometry to support these "anomalous" modes.

8.2 Future work

The measurements were done within the constraints imposed by a multi-user facility which required the capacity to return the spectroscopy system to its original configuration for standard transmission and acute angle reflection measurements. If this work were to continue, the primary requirement would be to have a fully dedicated THz ranging system for doing ATR measurements rather than a shared reconfigurable resource. This would greatly speed the process of data acquisition and confirmation of theoretical predictions.

Additionally, physical improvements to the experimental apparatus would be focused on:

1. sample mounting
2. sample preparation
3. choice of prism
4. modifications to the sample geometry

The priority would go to redesign of the sample mounting. The metafilm arrays were contact mounted onto the TIR surface as described in detail in Chapter 5. A minimum of an hour's preparation was devoted to cleaning, prepping and mounting the sample. Subsequent ATR measurements were required to determine if the air gap was small enough to not significantly interfere with the results. Aside from conducting the entire experiment in a cleanroom setting, improvements to be made could include horizontal placement of the sample. That is to say, gravity would hold the sample rather than surface tension and rubber bands. However this would require a heroic reconfiguration of the ranging system using the existing right angled prism.

Carefully positioning the array without a reference was a challenge to the position-dependent ATR measurements. In order to better control the lateral displacement of the MM sample with respect to the incident beam, a micrometer controlled translation stage would be required. However, due to requirements of good contact with the prism, a technique would need to be developed that would allow continuous movement without breaking the seal or damaging the Si prism/sample. Possibly, index matching fluids beyond those already considered could be used. But this would require additional research and would likely incur significant bureaucratic headaches to include work authorizations and waste stream management as non-polar liquids tend to be unfriendly to users or the environment.

A right angled silicon prism was used due to being readily available for ATR measurements. A dove prism shown in Figure 8-1 would be a better choice since it maintains the optical axis of the system and would not require realignment for ATR measurements [113]. Although the prism configuration shown in Figure 8-1 shows a liquid cell in the gravity assisted configuration proposed earlier, a normally mounted dove prism would equally well work in the ranging configuration with minor corrections to receiver axis alignment.

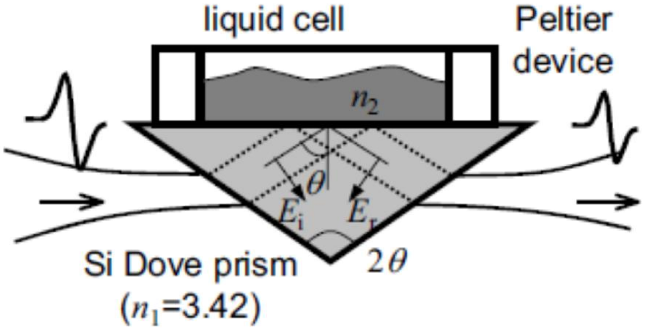

Figure 8-1 Dove prism for ATR measurements [113]

Surface roughness of the sample/prism interface is a major problem and can result in erroneous ATR measurements, but is typically observable in the additional Fresnel reflections observed. Opticaly polished silicon is prone to scratching. A scratch resistant material for the prism other than silicon needs to be considered. One option is to use disposable prisms so wear and tear on the components can be replaced. Changing the material of the prism to Teflon, which is less expensive than high purity silicon, may provide an alternative. For example, Teflon has a refractive index of 1.43 in the THz frequency range [114]. As a result, loss due to Fresnel reflections is reduced. However, the critical angle for Teflon-air interface is 44.4°. This would require larger incidence angles on the TIR interface which would necessitate the use of a dove prism instead of a simple right angled prism. This would introduce changes to the penetration depth of the evanescent field since the penetration depth increases with a reduced index of the prism material. The increased penetration depth would reduce the impact of a given air gap which would simplify the mounting process. Changing the prism material to Teflon would necessitate the use of Teflon substrates which would pose a challenge to the photolithography process. An alternative would be to fabricate the metafilms directly onto the prism surface which would only be feasible if there was a ready and cheap supply of appropriate prisms.

For changing the sample geometry, there are several directions that could be pursued. Maximizing the re-radiation signal by re-patterning the metafilm arrays may provide directions for further improvements. One way could be to modify the unit cell size of the metafilm to maintain a $\lambda/9$ separation, to couple to the geometric resonance mode. Following the theoretical treatment outlined in the previous chapter, the resonators can be designed in order to observe an increase in the emission due to an overlap of the geometric resonance and SRR self resonances. Another direction would be to modify the SRR array with missing rows and columns to be able to couple strongly to a magneto-inductive surface wave mode, based on the work done in [104]. To ensure that the coupling was due to evanescent field only, the metafilms need to be fabricated with a spacer layer of polyimide.

Further improvements to the optomechanical system that makes up the THz ranging system would be focused primarily upon the delivery of the femtosecond laser pulses to the receiver module. The optical fiber fundamentally limited the angular movement of the rotation assembly. The length of the fiber can be increased to ensure that there was enough slack by preventing any damage to the special receivers, which would in turn require modification to the dispersion compensation. Another possibility that was briefly considered was replacing the single mode fiber with a photonic bandgap fiber that has minimal dispersion at 800 nm. This would eliminate the losses incurred by the grating pair dispersion compensator and dramatically increase the signal measured at the receiver. This would provide more time in fruitful measurements rather than peaking up the system. The initial attempts to upgrade the ranging system were abandoned due to time constraints and experimental priority was given to other users which necessitated returning to the proven, yet underperforming, single mode fiber configuration.

Bibliography

1. G. J. Wilmink and J. E. Grundt, Journal of Infrared, Millimeter, and Terahertz Waves **32** (10), 1074-1122 (2011).
2. M.C. Kemp, P.F. Taday, B.E. Cole, J.A. Cluff, A.J. Fitzgerald and W.R. Tribe, SPIE **5070**, 44 (2003).
3. C. H. Matthias and F. József András, Journal of Physics D: Applied Physics **44** (8), 083001 (2011).
4. B. S. Williams, Nature photonics **1** (9), 517-525 (2007).
5. P. H. Siegel, Microwave Theory and Techniques, IEEE Transactions on **50** (3), 910-928 (2002).
6. D. Mittleman, *Sensing with terahertz radiation*. (Springer-Verlag, Berlin, 2003).
7. M. Tonouchi, Nature photonics **1** (2), 97-105 (2007).
8. K. Sakai, *Terahertz optoelectronics*. (Springer, Berlin, 2005).
9. S. L. Dexheimer, *Terahertz spectroscopy: principles and applications*. (CRC press, 2007).
10. N. J. Harrick, *Internal Reflection Spectroscopy*. (Interscience, 1967).
11. J. Fahrenfort, Spectrochimica Acta **17** (7), 698-709 (1961).
12. K. A. Chan, S. V. Hammond and S. G. Kazarian, Analytical chemistry **75** (9), 2140-2146 (2003).
13. Koulis, Cynthia V., J. A. Reffner, and A. M. Bibby, Journal of Forensic Science **46** (4) (2001).
14. H. Hirori, K. Yamashita and M. Nagai, Japanese Journal of Applied Physics **43** (10A), 3 (2004).
15. D. A. Newnham and P. F. Taday, Appl. Spectrosc. **62** (4), 394-398 (2008).
16. C. Rau, G. Torosyan, R. Beigang and K. Nerkararyan, Applied Physics Letters **86** (21), 211119 (2005).

17. D. Molter, G. Torosyan, J. Klier, C. Matheis, C. Petermann, S. Weber, F. Ellrich, J. Jonuscheit and R. Beigang, Infrared, Millimeter and Terahertz Waves (IRMMW-THz), 2011 36th International Conference on , pp.1,2, 2-7 Oct. 2011.

18. A. Nakanishi, Y. Kawada, T. Yasuda, K. Akiyama and H. Takahashi, Review of Scientific Instruments **83** (3), 033103 (2012).

19. A. Wojdyla and G. Gallot, Optics Letters **38** (2), 112-114 (2013).

20. D. Smith, J. Pendry and M. Wiltshire, Science (New York, N.Y.) **305** (5685), 788-792 (2004).

21. J. B. Pendry, A. J. Holden, D. J. Robbins and W. J. Stewart, Microwave Theory and Techniques, IEEE Transactions on **47** (11), 2075-2084 (1999).

22. V. Veselago, Soviet Physics Uspekhi **10** (4), 509-514 (1968).

23. D. R. Smith, W. J. Padilla, D. C. Vier, S. C. Nemat-Nasser and S. Schultz, Physical Review Letters **84** (18), 4184-4187 (2000).

24. V. M. Shalaev, Nature photonics **1** (1), 41-48 (2007).

25. J. Zhou, T. Koschny, M. Kafesaki, E. N. Economou, J. B. Pendry and C. M. Soukoulis, Physical Review Letters **95** (22), 223902 (2005).

26. N. I. Zheludev, Science **328** (5978), 582-583 (2010).

27. J. F. O'Hara, M. T. Reiten, P. Colestock, L. Earley and A. Taylor, Proc. SPIE **8093**, Metamaterials: Fundamentals and Applications IV, 809304 (2011).

28. N. Liu, H. Guo, L. Fu, S. Kaiser, H. Schweizer and H. Giessen, Nature materials 7 (1), 31-37 (2007).

29. K. Fan, A. C. Strikwerda, H. Tao, X. Zhang and R. D. Averitt, Opt. Express **19** (13), 12619-12627 (2011).

30. T. J. Yen, W. J. Padilla, N. Fang, D. C. Vier, D. R. Smith, J. B. Pendry, D. N. Basov and X. Zhang, Science **303** (5663), 1494-1496 (2004).

31. H.-T. Chen, W. J. Padilla, J. M. O. Zide, A. C. Gossard, A. J. Taylor and R. D. Averitt, Nature **444** (7119), 597-600 (2006).

32. T. Driscoll, H.-T. Kim, B.-G. Chae, B.-J. Kim, Y.-W. Lee, N. M. Jokerst, S. Palit, D. R. Smith, M. Di Ventra and D. N. Basov, Science **325** (5947), 1518-1521 (2009).

33. H.-T. Chen, W. J. Padilla, M. J. Cich, A. K. Azad, R. D. Averitt and A. J. Taylor, Nat Photon **3** (3), 148-151 (2009).

34. X. Liu, T. Starr, A. F. Starr and W. J. Padilla, Physical Review Letters **104** (20), 207403 (2010).

35. D. Y. Shchegolkov, A. K. Azad, J. F. O'Hara and E. I. Simakov, Physical Review B **82** (20), 205117 (2010).

36. R. W. Ziolkowski, J. Peng, J. A. Nielsen, M. H. Tanielian and C. L. Holloway, Antennas and Wireless Propagation Letters, IEEE **8**, 1329-1333 (2009).

37. W. J. Padilla, A. J. Taylor, C. Highstrete, M. Lee and R. D. Averitt, Physical Review Letters **96** (10), 107401 (2006).

38. J. Gu, R. Singh, Z. Tian, W. Cao, Q. Xing, M. He, J. W. Zhang, J. Han, H.-T. Chen and W. Zhang, Applied Physics Letters **97** (7), 071102 (2010).

39. H. Tao, A. C. Strikwerda, K. Fan, W. J. Padilla, X. Zhang and R. D. Averitt, Physical Review Letters **103** (14), 147401 (2009).

40. N. Papasimakis, V. A. Fedotov, N. I. Zheludev and S. L. Prosvirnin, Physical Review Letters **101** (25), 253903 (2008).

41. J. Gu, R. Singh, X. Liu, X. Zhang, Y. Ma, S. Zhang, S. A. Maier, Z. Tian, A. K. Azad and H.-T. Chen, Nature communications **3**, 1151 (2012).

42. H. Tao, W. J. Padilla, X. Zhang and R. D. Averitt, Selected Topics in Quantum Electronics, IEEE Journal of **17** (1), 92-101 (2011).

43. B. Reinhard, O. Paul and M. Rahm, Selected Topics in Quantum Electronics, IEEE Journal of **19** (1), 8500912-8500912 (2013).

44. Y. Minowa, M. Nagai, T. Hu, F. Kebin, A. C. Strikwerda, Z. Xin, R. D. Averitt and K. Tanaka, Terahertz Science and Technology, IEEE Transactions on **1** (2), 441-449 (2011).

45. P. R. Smith, Auston, D H, & Nuss, M C, IEEE J. Quantum Electron. **24** (2), 255-260 (1988).

46. D. Y. An *et al.*, Applied Physics Letters **102** (9), - (2013).

47. G. Gallerano and S. Biedron, presented at the Proceedings of the 2004 FEL Conference, 2004 (unpublished).

48. W. M. Robertson, *Optoelectronic techniques for microwave and millimeter-wave engineering*. (Artech House, Boston, 1995).

49. L. Xu, X. C. Zhang and D. H. Auston, Applied Physics Letters **61** (15), 1784-1786 (1992).

50. J. Hebling, K.-L. Yeh, M. C. Hoffmann, B. Bartal and K. A. Nelson, J. Opt. Soc. Am. B **25** (7), B6-B19 (2008).

51. B. B. Hu, X.-C. Zhang, D. H. Auston and P. R. Smith, Applied Physics Letters **56** (6), 506-508 (1990).

52. Y. Cai, I. Brener, J. Lopata, J. Wynn, L. Pfeiffer, J. B. Stark, Q. Wu, X. C. Zhang and J. F. Federici, Applied Physics Letters **73** (4), 444-446 (1998).

53. R. A. Cheville, J. Opt. Soc. Korea **8** (1), 34-52 (2004).

54. S. Ramani, M. S. thesis, Oklahoma State University, 2006.

55. M. van Exter and D. R. Grischkowsky, Microwave Theory and Techniques, IEEE Transactions on **38** (11), 1684-1691 (1990).

56. D. H. Auston, K. P. Cheung and P. R. Smith, Applied Physics Letters **45** (3), 284-286 (1984).

57. N. Katzenellenbogen and D. Grischkowsky, Applied Physics Letters **58** (3), 222-224 (1991).

58. Kiyomi Sakai, *Terahertz Optoelectronics* ,(Springer, 2005).

59. M. C. Beard, G. M. Turner and C. A. Schmuttenmaer, Journal of Applied Physics **90** (12), 5915-5923 (2001).

60. R. P. Prasankumar, A. Scopatz, D. J. Hilton, A. J. Taylor, R. D. Averitt, J. M. Zide and A. C. Gossard, Applied Physics Letters **86** (20), 201107 (2005).

61. E. F. Y. Kou and T. Tamir, Appl. Opt. **27** (19), 4098-4103 (1988).

62. E. Kretschmann, Z. Physik **241** (4), 313-324 (1971).

63. A. Otto, Z. Physik **216** (4), 398-410 (1968).

64. Pike Technologies, *ATR – Theory and Applications*, pp. 1-3,(Madison, 2005).

65. Z. M. Khoshhesab, in *Infrared Spectroscopy- Materials Science, Engineering and Technology*, edited by T. Theophanides (2012).

66. D. Grischkowsky, S. Keiding, M. v. Exter and C. Fattinger, J. Opt. Soc. Am. B **7** (10), 2006-2015 (1990).

67. H. Hirori, M. Nagai and K. Tanaka, Opt. Express **13** (26), 10801-10814 (2005).

68. E. Hecht, *Optics*, 4th ed. (Addison-Wesley, Reading, Mass., 2002).

69. C. A. Balanis, *Advanced engineering electromagnetics*. (Wiley, New York, 1989).

70. M. Born and E. Wolf, *Principles of optics : electromagnetic theory of propagation, interference and diffraction of light*, 6th ed. (Pergamon Press, Oxford ; New York, 1980).

71. F. Goos and H. Hänchen, Annalen der Physik **436** (7-8), 333-346 (1947).

72. K. Artmann, Annalen der Physik **437** (1-2), 87-102 (1948).

73. H. K. V. Lotsch, Optik **32** (1970/71).

74. R. H. Renard, J. Opt. Soc. Am. **54** (10), 1190-1196 (1964).

75. C. Schaefer and R.Pich, Ann. Physik **6** (2), 16 (1937).

76. A. Puri and J. L. Birman, J. Opt. Soc. Am. A **3** (4), 543-549 (1986).

77. M. T. Reiten, Ph.D dissertation, Oklahoma State University, 2006.

78. A. Lakhtakia, AEU - International Journal of Electronics and Communications **58** (3), 229-231 (2004).

79. I. V. Shadrivov, A. A. Zharov and Y. S. Kivshar, Applied Physics Letters **83** (13), 2713-2715 (2003).

80. E. D. Palik and R. T. Holm, Optical Engineering **17** (5), 175512-175512 (1978).

81. L. A. Averett, P. R. Griffiths and K. Nishikida, Analytical Chemistry **80** (8), 3045-3049 (2008).

82. R. Marqués, F. Medina and R. Rafii-El-Idrissi, Physical Review B **65** (14), 144440 (2002).

83. N. Katsarakis, T. Koschny, M. Kafesaki, E. N. Economou and C. M. Soukoulis, Applied Physics Letters **84** (15), 2943-2945 (2004).

84. W. Withayachumnankul and D. Abbott, Photonics Journal, IEEE **1** (2), 99-118 (2009).

85. D. Schurig, J. J. Mock and D. R. Smith, Applied Physics Letters **88** (4), 041109 (2006).

86. W. J. Padilla, M. T. Aronsson, C. Highstrete, M. Lee, A. J. Taylor and R. D. Averitt, Physical Review B **75** (4), 041102 (2007).

87. H.-T. Chen, J. F. O'Hara, A. J. Taylor, R. D. Averitt, C. Highstrete, M. Lee and W. J. Padilla, Opt. Express **15** (3), 1084-1095 (2007).

88. J. B. Pendry, A. J. Holden, W. J. Stewart and I. Youngs, Physical Review Letters **76** (25), 4773-4776 (1996).

89. W. J. Padilla, D. N. Basov and D. R. Smith, Materials today **9** (7), 28-35 (2006).

90. N. K. Grady, J. E. Heyes, D. R. Chowdhury, Y. Zeng, M. T. Reiten, A. K. Azad, A. J. Taylor, D. A. R. Dalvit and H.-T. Chen, Science **340** (6138), 1304-1307 (2013).

91. J. F. O'Hara, J. M. O. Zide, A. C. Gossard, A. J. Taylor and R. D. Averitt, Applied Physics Letters **88** (25), 251119 (2006).

92. Alan Cheville, *THz Time Domain Spectroscopy on a Budget*, http://thzspectrometer.okstate.edu/, (11 June 2013).

93. M. T. Reiten, K. McClatchey, D. Grischkowsky and R. A. Cheville, Opt. Lett. **26** (23), 1900-1902 (2001).

94. J. F. O'Hara, E. Smirnova, H.-T. Chen, A. J. Taylor, R. D. Averitt, C. Highstrete, M. Lee and A. J. Padilla, Journal of Nanoelectronics and Optoelectronics **2** (1), 90-95 (2007).

95. M. T. Reiten, D. Roy Chowdhury, J. Zhou, A. J. Taylor, J. F. O'Hara and A. K. Azad, Applied Physics Letters **98**, 131105 (2011).

96. W. Lukosz, Journal of the Optical Society of America **71** (6), 744-754 (1981).

97. D. S. Janning and B. A. Munk, Antennas and Propagation, IEEE Transactions on **50** (9), 1254-1265 (2002).

98. D. R. Denison and R. W. Scharstein, Microwave and Optical Technology Letters **9** (6), 338-343 (1995).

99. B. A. Munk, D. S. Janning, J. B. Pryor and R. J. Marhefka, Antennas and Propagation, IEEE Transactions on **49** (12), 1782-1793 (2001).

100. E. A. P. J.-B. Robertson, B. Sanz-Izquierdo and J. C. Batchelor, Metamorphose-VI, 2009 .

101. E. Shamonina, V. A. Kalinin, K. H. Ringhofer and L. Solymar, Journal of Applied Physics **92** (10), 6252-6261 (2002).

102. A. Radkovskaya, E. Tatartschuk, O. Sydoruk, E. Shamonina, C. J. Stevens, D. J. Edwards and L. Solymar, Physical Review B **82** (4), 045430 (2010).

103. H. Liu, Y. M. Liu, T. Li, S. M. Wang, S. N. Zhu and X. Zhang, physica status solidi (b) **246** (7), 1397-1406 (2009).

104. J. L. Garcia Pomar, B. Reinhard, J. Neu, V. Wollrab, O. Paul, R. Beigang and M. Rahm, SPIE **7945**, Quantum Sensing and Nanophotonic Devices VIII, 79450V (2011).

105. J. O’Hara, A. K. Azad and A. J. Taylor, Eur. Phys. J. D **58** (2), 243-247 (2010).

106. J. F. O'Hara, E. Smirnova, A. K. Azad, H.-T. Chen and A. J. Taylor, Active and Passive Electronic Components **2007**, Article ID 49691, 10 pages, (2007).

107. S. Ramani, M. T. Reiten, P. L. Colestock, A. J. Taylor, A. K. Azad and J. F. O'Hara, Terahertz Science and Technology, IEEE Transactions on **3** (6), 709-720 (2013).

108. F. Capolino, *Theory and phenomena of metamaterials*. (CRC Press, 2010).

109. E. J. Rothwell and M. J. Cloud, *Electromagnetics*. (CRC press, 2010).

110. J.R.Wait, *Electromagnetic waves in stratified media*. (Pergamon Press, 1970).

111. B. Munk, *Finite Antenna Arrays and FSS*. (Wiley-IEEE Press, 2003).

112. P. L. Colestock, (private communication) .

113. M. Nagai, H. Yada, T. Arikawa and K. Tanaka, Int J Infrared Milli Waves **27** (4), 505-515 (2006).

114. Tydex Optics, *THz materials*, http://www.tydexoptics.com/products/thz_optics/thz_materials/, (13 May 2013).

Appendix

Matlab Code for method of moments solution for far-field re-radiation

```
% Code to solve current distribution on ATR Surface
% Modified from Pat Colestock's atrsol.c version 09.15.13


% Input parameters

R = 42.0; %
L = 281e-12; % R,L,C lumped components of individual SRRs
C = .4e-15;
nn = 200; % nn = number of line sources in array

nvec = [1:nn]; % vector of array
muo = 12.56637e-7; %
dd = 1e-5; % dd = width of capacitive gap in SRR, scales electric
coupling
% warning! not implemented yet.  Will modify the strength of the
current
% from the driving field VV.
A = 0.05e-9; % area of SRR that scales magnetic coupling
scale = 80e-6; % unit cell spacing
RR = 2; % RR = field radius of constructed Ey field RR meter away
kp1 = 3.42; % index of Si substrate
xin = 0.0079; % xin = position of beam incidence < nn*scale
wd = 20.0; % wd = half width of incident beam in cell spacings

thetain = 45*pi/180; % incident angle with respect to normal
% (all units MKS thank god)

% freq = 3.9214e11; % freq = frequency in Hz
freq = linspace(1e11,1.8e12,80);
maxrad = 2*nn; % number of angular points
ff_freq = zeros(length(freq),maxrad);
II_freq = zeros(length(freq),nn);
for kk = 1:length(freq);
 kk
ww = 2*pi*freq(kk); % angular frequency
ko = ww/3e8; % |k| vector in free space
k1 = kp1*ww/3e8; % |k| vector in silicon

% Note regarding Hankel functions in Matlab
% Hnu^(2) would be the Hankel function of the second kind order nu
```

```
% where the H_nu = J_nu - i*Y_nu (second kind is conjugate of first)
%         besselh(nu,2,z) = besselj(nu,z) - i*bessely(nu,z)


% Compute [Z]
ZZ = zeros(nn,nn);
for ii = 1:nn; for jj = 1:nn;
        if ii==jj;
            ZZ(ii,jj) = R-1i*ww*L+1i/(ww*C);
        else;
            d = scale*abs(ii-jj);
            bogus1 = 2*ko/d^2*besselh(1,2,ko*d)-
ko^2/d*besselh(0,2,ko*d);
            bogus2 = -
2*k1/d^2*besselh(1,2,k1*d)+k1^2/d*besselh(0,2,k1*d);
            %bogus1+bogus2 => magnetic coupling only from eqn 10 in
paper
            %using Wait's Green's function "Electromagnetic Waves in
            %Stratified media" ChII pp 25-26
            ZZ(ii,jj) = -ww*muo*A/(2*(ko^2-k1^2))*(bogus1 + bogus2);
        end;
    end; end;

% Now solve for the inverse of the impedance matrix [ZZ]
%
ZZinv = inv(ZZ);

% Set up external excitation beam vector VV
nc = round(nn);
VV = exp(-(nvec-nc).^2/wd^2).*exp(1i*cos(thetain)*k1*scale*abs(nvec-
nc));

% Generate the currents [II] = [ZZ]^-1[VV]
%
II = zeros(size(VV));
for jj = 1:nn;
    II(jj) = sum(ZZinv(jj,:).*VV);
end;
II_freq(kk,:) = II;
% Generates field pattern away from surface by summing contribution
from
% each element
%
clear bogus1 bogus2
field = zeros(1,maxrad);
thetaout = pi/maxrad*[0:maxrad-1];
for ii = 1:maxrad;
    xff = RR*cos(thetaout(ii));
    yff = RR*sin(thetaout(ii));

for jj = 1:nn;
    xs = scale*(jj-nn/2);
    dd = sqrt((xff-xs)^2+yff^2);
```

```
%      field(ii) = field(ii)+ II(jj)*exp(1i*ko*dd)/dd; % original Pat
     bogus1= yff*exp(pi/4)/(yff +dd*sqrt(kp1^2-(xff/dd)^2));
     bogus2= exp(-1i*ko*dd)./sqrt(ko*dd);
    field(ii) = field(ii)+ II(jj)*ww*muo/(sqrt(2*pi))*bogus1*bogus2; %
John paper
end; end;

ff_freq(kk,:) = field;
end;
```

VITA

Suchitra Ramani

Candidate for the Degree of

Doctor of Philosophy

Thesis: METAMATERIAL RADIATION FROM ATTENUATED TOTAL REFLECTION AT TERAHERTZ FREQUENCIES

Major Field: Photonics (Electrical Engineering)

Biographical:

Education: B.E. in Instrumentation, 2001, University of Mumbai, India M.S. Photonics, 2006, Oklahoma State University, Stillwater, Oklahoma. Completed the requirements for the Doctor of Philosophy in Photonics at Oklahoma State University, Stillwater, Oklahoma in December, 2013.

Experience: Worked on material characterization using Terahertz Differential Time Domain Spectroscopy (THz-DTDS). Investigated the conduction mechanisms in porous silicon at terahertz frequencies using THz-TDS under Dr. Alan Cheville at Oklahoma State University. Investigated and reported sources of experimental and analytical errors that affect the accuracy and repeatability of DTDS measurements. Investigated coupling phenomena in planar metamaterials using Attenuated total reflection as part of my doctoral research at Center for Integrated Nanotechnologies, MPA, LANL.

Professional Memberships: Student member of OSA